

---

---

# Attitude Control System

## for AAUSAT6

---

---



GROUP CE-631  
ELECTRONICS & IT  
AALBORG UNIVERSITY  
DATE: 30 MAY 2018





## AALBORG UNIVERSITY STUDENT REPORT

**Aalborg University**  
Electronics & IT  
Fredrik Bajers Vej 7  
9220 Aalborg Øst  
[www.es.aau.dk](http://www.es.aau.dk)

**Title:**

Attitude Control System  
for AAUSAT6

**Theme:**

BSc Project (Control Engineering)

**Project Period:**

Spring Semester 2018

**Project Group:**

CE-631

**Participants:**

Christian Bekhøi Roskær  
Henrik Glavind Clausen

**Supervisor:**

Jesper Abildgaard Larsen

**Pages:** 85

**Appendix:** 11 (A-B)

**Date of Completion:** 30-05-2018

**Abstract:**

A new attitude control system is needed for the coming AAUSAT 6 satellite, which requires a higher precision compared to earlier iterations of the AAU satellites, due to a presumed camera payload.

This project is therefore based on reaction wheels as actuators, as an attempt to achieve a higher precision than former satellites developed at Aalborg University. AAUSAT6 is modeled based on specifications of earlier AAUSAT satellites. A dynamic model for the satellite with reaction wheels is derived, and a fitting PI controller is designed. The modeled system with the controller is then simulated, using software libraries from AAU's earlier work with satellites, and the simulated system fulfill the given requirements.

Subsequently, the controller is implemented on a testbed made by former AAU students, as an attempt to reproduce the simulations. This however did not prove to possible, as manual center of mass adjustments were inadequate and the air bearing of the testbed caused too large disturbance torques. Suspending the satellite model of the testbed using a fishing line gave better results comparable to the simulations, but still significantly worse and not able to fulfill the given requirements.



# Preface

This report is conducted by group 631 as part of the BSc project in the Electronic & IT programme at Aalborg University.

The theme of this project is Control Engineering and the purpose is to develop an Attitude Control System for AAUSAT6.

We would like to thank Brian Gasberg Thomsen and Jens Nielsen for taking time out of their schedule to help us get the ACS testbed up and running.

## Reading guide:

This report is divided into chapters numbered by the order they appear. Sections and subsections are numbered as well the same way, but subsubsections appear without numbers.

Figures, tables, equations, and code examples are numbered by the chapter they appear in as well as the order. Figure 5 in chapter 4 will thereby be numbered as 4.5. Appendices are found in the back of the report and will be numbered with letters, which will be referred to throughout the report.

The reference method *Vancouver* is used throughout the report. A list of the references is found at the end of the report, numbered and organized by the order they are used in the report. References are indicated in the text with a number that matches the list in the back. Example of a reference:

By Murphy's Law, when the loop is first closed, the sign will be wrong and the behavior will be unexpected unless the engineer understands how the response will go if the gain which should be positive is instead negative [0].

[0] Franklin GF, Powell JF, Emami-Naeini A. Feedback Control of Dynamic Systems. 4th ed. Prentice Hall; 2002.



Christian Bekhøi Roskær  
<croska15@student.aau.dk>



Henrik Glavind Clausen  
<hclaus15@student.aau.dk>

## Notation

Throughout the report the following mathematical notation is used:

Scalars	Italic	$k, K$
Vectors	Lower case boldface	$\mathbf{v}$
Matrices	Upper case boldface	$\mathbf{A}$
Quaternions	Lower case italic boldface	$\mathbf{\mathit{q}}$
Operation point	Bar	$\bar{\omega}$
Small signal	Tilde	$\tilde{\omega}$
Unit vector	Hat	$\hat{\mathbf{v}}$
Identity matrix	Boldface 1	$\mathbf{1}$

# Contents

<b>1</b>	<b>Introduction</b>	<b>1</b>
<b>2</b>	<b>Pre-analysis</b>	<b>3</b>
2.1	Orbit Description . . . . .	3
2.2	Reference Frames . . . . .	5
2.3	Disturbance Torques . . . . .	9
2.4	Testbed Introduction . . . . .	13
<b>3</b>	<b>Project Scope</b>	<b>15</b>
3.1	Requirements . . . . .	15
3.2	Test Specifications . . . . .	20
<b>4</b>	<b>Modeling of the Satellite</b>	<b>21</b>
4.1	Attitude Parametrization . . . . .	21
4.2	Rotational Mechanics . . . . .	24
4.3	Kinematic Model . . . . .	25
4.4	Dynamic Model . . . . .	27
4.5	Reaction Wheels and DC Motors . . . . .	29
<b>5</b>	<b>Controller Design</b>	<b>37</b>
5.1	Attitude Control in One Axis . . . . .	37
5.2	Attitude Control in Three Axes . . . . .	41
<b>6</b>	<b>Simulation of Attitude Control System</b>	<b>61</b>
6.1	Implementation in Simulink . . . . .	61
6.2	Simulation Results . . . . .	64
<b>7</b>	<b>Acceptance Test</b>	<b>71</b>
7.1	Implementation on the Testbed . . . . .	71
7.2	Controller Tests on Testbed . . . . .	73
7.3	Tests Using a Suspended Satellite Model . . . . .	77
7.4	Summary . . . . .	80
<b>8</b>	<b>Closure</b>	<b>83</b>
8.1	Conclusion . . . . .	83
8.2	Future Improvements . . . . .	84
	<b>Bibliography</b>	<b>87</b>

<b>A Quaternions</b>	<b>89</b>
<b>B Controller test using the ACS testbed and suspension</b>	<b>91</b>
B.1 Controller test using the testbed . . . . .	91
B.2 Controller test using suspension . . . . .	96

# 1 | Introduction

In 2003 students from Aalborg University launched their first CubeSat called AAU CubeSat. Since then, several other student-built CubeSats from AAU have been launched with great success: AAUSAT-II, AAUSAT3, AAUSAT5, and latest AAUSAT4 in 2016.

The CubeSat specifications were initially developed by Standford University and California Polytechnic State University, with the aim of having a relative cheap way of developing and deploying small scale satellites. The reference design was proposed in 1999, and the first CubeSat was launched in 2003 and has since become a standard over time.

CubeSats are specified to be small such that cost can be kept down, initially with a size of 10x10x11.35 cm (size called a 1U CubeSat) and a weight of maximally 1.33 kg. A sketch of a 1U CubeSat can be seen in figure 1.1. Later it has been made possible to stack these satellites into one another, such that a larger volume is possible making the satellites up to 3U. Only increasing the size in one dimension means that it is possible to keep the same launching mechanism for keeping cost down. In the recent years larger satellites have been developed such as 6U (2x3 1U) and 8U (2x4 1U), typically to go beyond educational purpose and slide into commercial purposes.

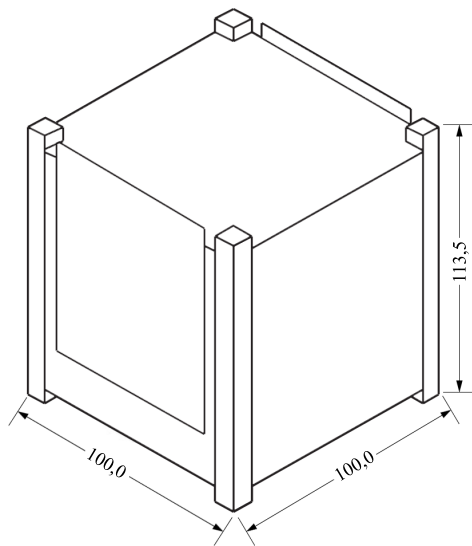


**Figure 1.1:** A sketch of a 1U CubeSat.

All previous AAUSAT satellites have been equipped with an Attitude Determination and Control System (ADCS) to keep the satellite from tumbling and to point the antennas

towards Earth to make radio communication possible.

The next student-built CubeSat from AAU will be called AAUSAT6. As all the previous AAUSAT satellites, this satellite is assumed to be a 1U CubeSat. Currently several payload options are being discussed for AAUSAT6, one of them being a camera.

To get the most out of the camera, it is necessary to be able to point the satellite in a desired direction with high precision. This sets stricter requirements to the ADCS compared to previous satellites. In addition to pointing the camera in a specific direction, an improved ADCS will be able to point the antennas in a specific direction with greater precision and thereby increase the signal strength of the radio link between the satellite and ground station.

## Actuators for Attitude Control

The most recent AAUSAT satellites only had magnetorquers as actuators for attitude control. Magnetorquers are coils working like electromagnets, that due to the magnetic field of Earth can produce a torque changing the attitude of the satellite. With magnetorquers it is only possible to control the attitude in two axes at a given time. Three axes control can be obtained by changing attitude over time, such that the magnetorquers acts on new axes as the magnetic field of Earth changes along the orbit path. This leads to a slow actuation speed and low precision, which might not be ideal for satisfactory usage of a camera payload.

To be able to control the attitude in three dimensions at any given time, several other types of actuators exist. One solution is jet propulsion. This, however, requires fuel of which it is only possible to bring a finite amount of into space and is therefore not a suitable option for continuous attitude control in CubeSats.

Another option for actuators is reaction wheels. A reaction wheel (also called momentum wheel) is a spinning wheel, which due to the conservation of angular momentum, produces a torque on the satellite when the wheel is accelerated or decelerated. With three or more reaction wheels it is possible to control the attitude in three axes at any given time. Reaction wheels do however saturate at some point when they cannot accelerate any further, and this puts a limit on how much (or how long) the satellite attitude can be controlled. A way to overcome this weakness is by the use of momentum dumping. This means to have another actuator produce a torque on the satellite as the reaction wheels accelerates or decelerate, such that the combined force on the satellite is zero. Using magnetorquers for this purpose is a valid option.

Therefore the option to develop a control algorithm for a 3-axes ADCS, based on the use of both reaction wheels and magnetorquers as actuators will be investigated.

We have now looked into what the project's initial proportions. The following chapter deal with, the fundamentals of an orbit around earth, and how different frames of reference is need when computing a satellites attitude, and how the cube satellite is affected by the perturbations, found in low earth orbit. Such that the scope of the project can be obtained.

## 2 | Pre-analysis

This chapter investigates some of the general details related to satellites in orbit around the Earth, including a general orbit description and the different reference frames related to attitude determination and control. In addition to this, the environmental disturbance torques affecting the satellite attitude will be examined. Finally a short introduction to the available ACS testbed will be presented.

### 2.1 Orbit Description

The perigee height (or just perigee) is the shortest distance from the satellite to the surface of Earth. Apogee height is the largest distance from the satellite to the surface of Earth.

To gain an understanding of what it means when a satellite is moving in an orbit around Earth, and how this works regarding attitude control, a basic orbital description is needed, along with some of the terminology related to this. A simple manner to consider this is through a Keplerian orbit.

A way to think of an orbit, is to think of this 2-dimensional ellipse. Describing the path of an orbiting object, which is the Keplerian orbit. It takes its basis in gravitational attraction between two objects with no perturbations included, as stated by Kepler's first law. Kepler's first law states that two objects that interact gravitationally and are permanently associated will have orbits that are ellipses.

Within such an orbit the object with the most mass is called the primary, and the object with the lesser mass is called secondary or satellite. These two objects will interact gravitationally with each other, and they will revolve around a point called the barycenter. This center is the combined center of mass between these objects. In the case that one object has a significantly bigger mass, the barycenter is typically located within the bigger mass, which is the case for any man made satellite around Earth.

A specific orbit can be described by different elements. All of them will not be examined here, but only the elements that will be relevant for attitude control. In this project, AAUSAT6 will be assumed to have the same orbit as AAUSAT4. The relevant orbit parameters for AAUSAT4 are written in table 2.1.

Apogee is the highest point in the orbit in relation to Earth, and perigee is the lowest point. The semi-major axis is largest distance from Earth's center to the satellite in the elliptic orbit. In addition to this it can be relevant to know the ascending node, which is the where a satellite crosses the equatorial plane from perigee, and the opposite

Parameter	Value	Unit
Semi-major axis	6927	km
Perigee height	443	km
Apogee height	668	km
Inclination	98.1	°
Orbit period	5880	s
Mean orbital speed	7.5	km/s

**Table 2.1:** List of essential orbit parameters for AAUSAT4 [1].

is called descending node. This is illustrated in figure 2.1.

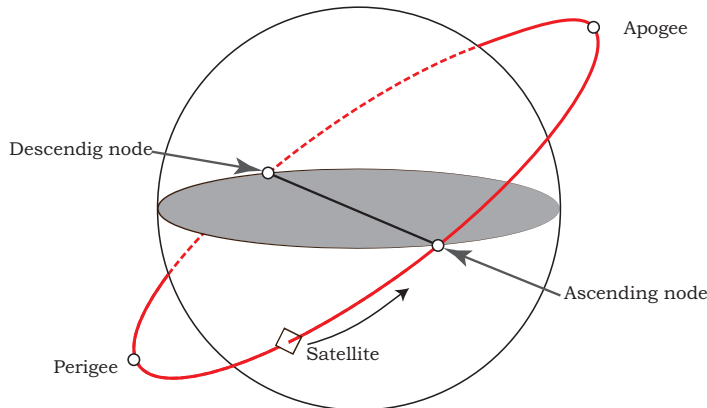


**Figure 2.1:** Sketch of a satellite's orbit around Earth.

Satellites with an altitude of less than 2000 km are considered to be in Low-Earth Orbit (LEO), and this is the case for AAUSAT4 and all previous AAUSAT satellites as well.

When talking about a satellite's movement in relation to orbits, it can be convenient to refer a specific time as a number of orbits e.g. "a rotation on the fifth orbit" as a way to describe at which point a satellite is supposed to perform an action. It is thus relevant to know the orbit period of a satellite.

The way a satellite orbits around the earth, is said to be its inclination angle. The angle starts at east and increases towards north as illustrated in figure 2.2. Satellites that move with an inclination angle below 90°, and thereby with Earth's rotation, is called prograde. Satellites with an angle above 90° are called retrograde. AAUSAT4 has an inclination angle of 98.1° making it retrograde.

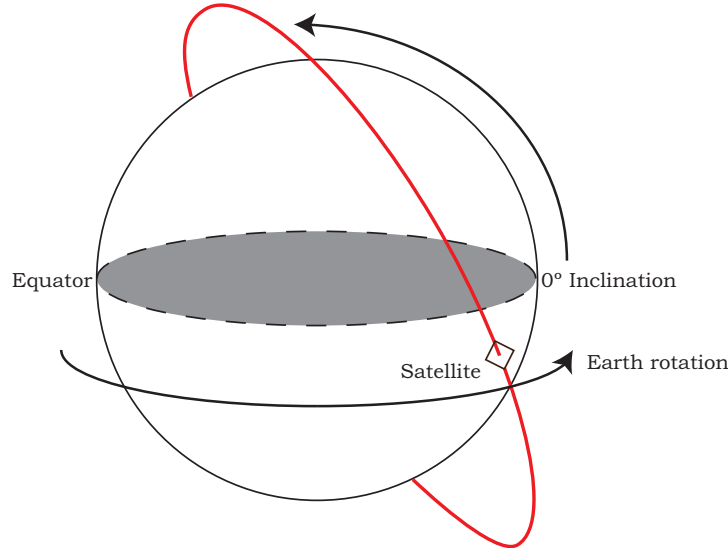


**Figure 2.2:** Sketch of a satellite's inclination angle in relation to the Earth.

The orbital speed  $v$  of a satellite in orbit at a certain point can be calculated as follows [2]:

$$v = \sqrt{\mu \left( \frac{2}{r} - \frac{1}{a} \right)} \quad (2.1)$$

where  $r$  is the distance from the satellite to Earth's center at the current point and  $a$  is the semi-major axis. The parameter  $\mu$  is the standard gravitational parameter defined as  $GM$ , where  $G$  is the gravitational constant and  $M$  is the mass of Earth. Thus  $\mu = 403.5033 \cdot 10^{12} \text{ m}^3/\text{s}^2$ . In essence this formula means that a satellite in orbit will change velocity as they move in the orbit, gaining speed as they decent from apogee, and losing speed as they ascend from perigee. For LEO satellites this difference may however be negligible, because the difference in velocity is relatively low compared to the mean velocity. For instance, AAUSAT4 has a mean velocity of about 7.5 km/s and the difference in velocity while orbiting is 16m/s, which is a difference of 0.2% between the highest and lowest point.

## 2.2 Reference Frames

When controlling the attitude of a satellite, it is important to know what the attitude is specified in relation to, such as the Earth or the satellite itself. Therefore a number of reference frames are needed.

This section describes a total of five different reference frames, with background in how to control the satellite and how to orient the satellite towards a desired point. These are listed in table 2.2 along with a short description explaining why it is useful.

Throughout the report, certain quantities, such as rotation matrices, will be denoted with prescripts according to which reference frame they are defined in relation to. For example, a matrix transforming a vector from the ECI frame to the CRF will be noted  ${}^c\mathbf{A}$ .

In the following, each reference frame will be described more in depth.

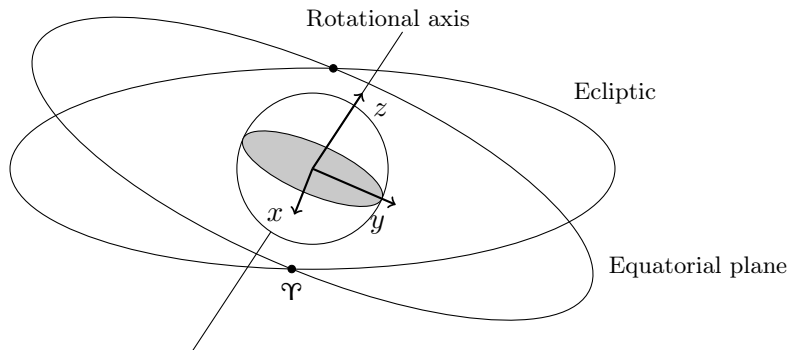
Reference Frame	Description	Prescript
Earth-Centered Inertial (ECI)	The ECI frame will be used as the main reference frame for most applications as this will be the reference frame in which the attitude of the satellite will be defined from the ADS.	<i>i</i>
Earth-Centered Earth-Fixed (ECEF)	The ECEF frame is of interest mainly because of the Earth's magnetic field, which is important when using magnetorquers, and when targeting a specific point on Earth's surface.	<i>f</i>
Satellite Reference Frame (SRF)	The SRF is needed to be able to relate the attitude of the satellite to the physical body of the satellite.	<i>s</i>
Control Reference Frame (CRF)	The CRF is mainly used for computational purposes as this frame eases certain parts of the calculations related to the mathematical modeling of the satellite.	<i>c</i>
Orbit Reference Frame (ORF)	The ORF is useful when commanding the satellite to point in a specific direction related to its orbit.	<i>o</i>

**Table 2.2:** List of relevant reference frames.

### 2.2.1 Earth-Centered Inertial (ECI)

One commonly used coordinate system is the Earth-Centered Inertial reference frame which is defined with the origin point  $(0, 0, 0)$  as the Earth's center of mass. The  $z$ -axis of the coordinate system is defined along the rotational axis of the Earth (through the geographical poles), the  $x$ -axis through the vernal equinox, and the  $y$ -axis through the point where the meridian  $90^\circ$  east of the vernal equinox crosses equator.

The vernal equinox is the point where the celestial equator (the plane of the terrestrial equator extended to space) intersects with the ecliptic (the plane in which the Earth orbits the Sun) going south to north as illustrated in figure 2.3. The intersection of the celestial equator and the ecliptic going north to south is called the autumnal equinox. The angle between the equatorial plane and the ecliptic plane is called the axial tilt of obliquity and is approximately  $23.4^\circ$ .

**Figure 2.3:** Illustration of the definition of the vernal equinox, noted by the symbol  $\Upsilon$ .

This ECI coordinate system is not fixed to the Earth in the sense that when the Earth is rotating about itself, the ECI coordinate system does not rotate along with it.

The ECI reference frame is not constant in relation to time. Due to the gravitational forces of the Moon and the Sun, the Earth's rotational axis itself rotates about the ecliptic poles. This phenomenon is called precession, and one complete rotation takes 26000 years. In addition to this, the Earth's rotational axis wobbles in a way called nutation with an amplitude of approximately  $0.0025^\circ$  and a period of 19 years. The precession and nutation results in the equinoxes and the equatorial plane not being constant, but change according to the time. Therefore, the ECI has to be specified according to a specific time. A commonly used system is the 2000 coordinates, where the mean equator and mean equinox are defined according to 1 January 2000.

### 2.2.2 Earth-Centered Earth-Fixed (ECEF)

Like ECI, the Earth-Centered Earth-Fixed (ECEF) coordinate system is also defined based on the Earth, but differs in that the coordinate system is fixed (as the name refers to) to the Earth, such that the coordinate system rotates along with the rotation of the Earth. Just like the ECI, the ECEF coordinate system has its origin in Earth's center of mass and its  $z$ -axis through the geographical poles. The  $x$ -axis is defined as going through the intersection of equator and the prime meridian ( $0^\circ$  longitude and  $0^\circ$  latitude). The  $y$ -axis goes through the point on the equator  $90^\circ$  east.

### 2.2.3 Satellite Reference Frame (SRF)

The satellite itself also has a frame of reference. It is used for recognizing the orientation of the satellite in relation to another frame of reference, for example the ECI. The Satellite Reference Frame is defined in relation to the frame of the satellite, with the origin point  $(0, 0, 0)$  in one of the corners and the three axes along the borders of the frame of the satellite. As illustrated in figure 2.4. This reference frame is mainly used to give a reference of the satellite compared to the ECI, such that the desired attitude can be interpreted, and therefore is this frame defined based on what is most convenient when interpreting the attitude. For the purposes of this project, the camera payload will be assumed to be placed along the  $z$ -axis, while the  $x$ - and  $y$ -axes will be perpendicular to the  $z$ -axes to form a right-handed coordinate system.

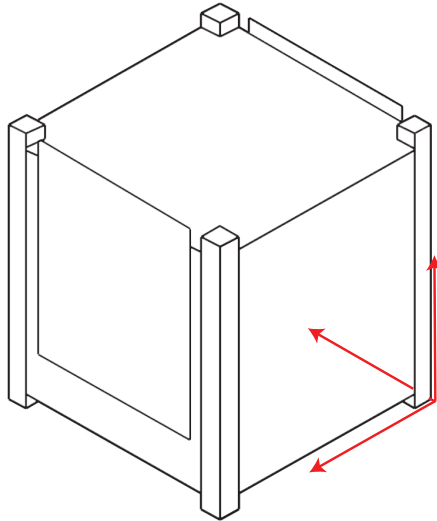


**Figure 2.4:** Illustration of the Satellite Reference Frame

#### 2.2.4 Control Reference Frame (CRF)

This frame is used for having the principal axes going through the satellite, such that the mass of the satellite is equally distributed around the principal axes giving it mass symmetry. The purpose of this CRF is to make calculations easier, because mass symmetry along the principal axes gives a smaller expression, because we do not need to take into account deviations from the center of mass. More on this in section 4.2.

#### 2.2.5 Orbit Reference Frame (ORF)

The Orbit Reference Frame is defined to have the origin point  $(0, 0, 0)$  in the center of mass of the satellite. It consists of a roll axis  $x$ , a pitch axis  $y$  and a yaw axis  $z$ . The roll axis is defined along the velocity vector of the satellite. The yaw axis is along the nadir, which is the name of the direction toward the center of the Earth. The pitch axis is perpendicular to the two others. This is illustrated in figure 2.5.

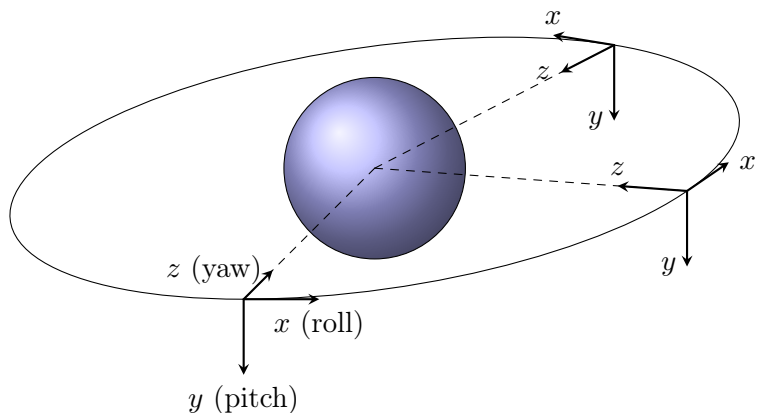


**Figure 2.5:** Illustration of the Orbit Reference Frame.

The Orbit Reference Frame will mainly be used in relation to the desired attitude of the satellite. If the satellite for example is supposed to point a camera in the direction of Earth during the entire orbit, it would be easy to specify this in relation to the ORF.

## 2.3 Disturbance Torques

When designing an attitude control system for a satellite, it is valuable to know what sources of disturbance exist in space and what order of magnitude can be expected from them. This section therefore describes the sources for the disturbances and aims to give an estimate for the worst case disturbance torque the satellite may be subjected to. The following four disturbance torques will be investigated:

- Solar Radiation
- Gravity Gradient
- Aerodynamic Drag
- Magnetic Disturbance

### 2.3.1 Solar Radiation

When a surface on the satellite is subjected to sunlight, the solar radiation will provide a radiation pressure on the surface which will result in a torque about the center of mass of the satellite. The magnitude of the torque depends on the intensity and angle of incidence of the solar radiation and the optical properties of the surface.

The intensity of the solar radiation is assumed constant for a satellite orbiting the Earth and is described by the solar constant  $F_s = 1367 \text{ W/m}^2$  [2].

In general, radiation hitting surface can be absorbed or reflected, or in most cases a mix of both. However, by assuming that the surface has a uniform reflectance, a simple estimate for the force  $f_{\text{sr}}$  due to the solar radiation can be obtained as [3]:

$$f_{\text{sr}} = \frac{F_s}{c} A_s (1 + q) \cos \theta \quad (2.2)$$

where  $F_s$  is the solar constant,  $c$  is the speed of light,  $A_s$  is the surface area,  $\theta$  is the angle of incidence, and  $q$  is the unitless reflectance factor (ranging in values from 0 for perfect absorption to 1 for perfect reflection).

The torque  $\tau_{\text{sr}}$  about the center of mass can thus be found by

$$\tau_{\text{sr}} = f_{\text{sr}} \cdot r \quad (2.3)$$

where  $r$  is the distance from the center of mass to the center of radiation pressure.

According to equation (2.2), the radiation pressure is largest when the radiation is completely reflected back exactly the way it came, i.e.  $\theta = 0$  and  $q = 1$ . Similarly, the torque will be largest when the center of mass and the center of radiation pressure are furthest away from each other. For a 1U CubeSat such as AAUSAT6, the center of mass is assumed to be close to the geometric center, this distance is largest if the center of radiation pressure is in one of the corners. This will result in a distance of roughly

0.09 m. Assuming the surface area for AAUSAT6 to be 0.1 m by 0.1 m and inserting the aforementioned values in equation (2.2) and (2.3), we can calculate an estimate for the worst case solar radiation torque to be  $\tau_{sr} = 8.2 \cdot 10^{-9}$  Nm.

### 2.3.2 Gravity Gradient

The gravitational force between Earth and the satellite keep the satellite in orbit, but it is also a source of disturbance. Generally we would like to think of the gravity as something that pulls uniformly on the satellite, but in reality the satellite's mass is not uniformly distributed, which means that gravity will pull non-uniformly on it, which will result in a torque. The gravitational force  $d\mathbf{f}_i$  on a given mass element  $m_i$  can be described as:

$$d\mathbf{f}_i = \frac{-\mu \mathbf{s}_i dm_i}{|\mathbf{s}_i|^3} \quad (2.4)$$

where  $\mu$  is the standard gravitational parameter as defined in equation (2.1) and  $\mathbf{s}_i$  is the position of a given mass  $m_i$  on the satellite relative to the center of mass of Earth.

This means that the torque can be computed as follows, where  $\mathbf{r}_i$  is the distance from the satellite's center of mass to the mass element:

$$d\boldsymbol{\tau}_i = \mathbf{r}_i \times d\mathbf{f}_i \quad (2.5)$$

By integrating equation (2.5) over all the mass of the satellite, the gravity gradient disturbance torque can be computed. It can be shown that this will result in the following equation, where  $\mathbf{I}$  is the satellite's moment of inertia matrix [2]:

$$\boldsymbol{\tau}_{GG} = \frac{3\mu}{|\mathbf{s}|^3} (\hat{\mathbf{s}} \times (\mathbf{I} \cdot \hat{\mathbf{s}})) \quad (2.6)$$

The gravity gradient is then only depending on the inertia matrix and the satellite's distance to Earth. If the inertia matrix of AAUSAT3 (equation 4.18) is inserted into equation 2.6, and the distance is set to AAUSAT4's perigee at approximate 6814 km, then the largest torque will appear when  $\hat{\mathbf{s}} = [1 \ 0 \ 1]^T / \sqrt{2}$  or  $\hat{\mathbf{s}} = [1 \ 1 \ 0]^T / \sqrt{2}$ . This will result in a gravity gradient disturbance torque of  $|\boldsymbol{\tau}_{GG}| = 0.945 \cdot 10^{-9}$  Nm.

### 2.3.3 Aerodynamic Drag

Even though the atmosphere of Earth decays exponentially as a function of altitude, the atmosphere is still present in low Earth orbit and must therefore be taken into consideration. Just as on the surface of Earth, the force  $f_{ad}$  due to aerodynamic drag from the atmosphere can be described by the following equation [3]:

$$f_{ad} = \frac{1}{2} \rho C_d A_s v^2 \quad (2.7)$$

where  $\rho$  is the atmospheric density,  $C_d$  is the drag coefficient,  $A_s$  is the surface area in the direction of the velocity and  $v$  is the velocity of the satellite.

As can be seen from the equation, the force is proportional to the square of the velocity. So even though the atmospheric density is low in LEO, the high velocity of the satellite makes the aerodynamic drag significant.

In the same way as for the solar radiation, when the aerodynamic drag force is not aligned with the center of mass of the satellite, the satellite will be subjected to a torque  $\tau_{\text{ad}}$ :

$$\tau_{\text{ad}} = f_{\text{ad}} \cdot r \quad (2.8)$$

where  $r$  is the distance from the center of mass to the center of aerodynamic pressure.

We do not have any experimental data to determine the drag coefficient, but this is usually between 2.0 and 2.5 for spacecraft [3], so in our worst case calculation we will use  $C_d = 2.5$ . The atmospheric density is highly dependent on the altitude, so with basis in AAUSAT4's orbit, the lowest altitude is 441 km at which point the mean density is  $\rho = 1.585 \cdot 10^{-12} \text{ kg/m}^3$  [2]. The velocity of the satellite is assumed to be  $v = 7.5 \text{ km/s}$ . As in the estimate for the solar radiation torque, the surface area is assumed to be  $A_s = 0.1 \cdot 0.1 = 0.001 \text{ m}^2$  and the worst-case distance between the center of mass and center of aerodynamic pressure is  $r = 0.09 \text{ m}$ . With these values, the resulting torque is  $\tau_{\text{ad}} = 100.3 \cdot 10^{-9} \text{ Nm}$ .

### 2.3.4 Magnetic Disturbance

The magnetic disturbance torque is present for the same reason as magnetorquers work. Therefore the physics behind magnetorquers will be investigated first, before proceeding with the magnetic disturbance.

Magnetorquers are in essence electromagnets, with the purpose of using the Earth's magnetic field to produce a torque.

The magnetorquers are coils in one form or another conducting a current, which follow Laplace's law [4]:

$$\mathbf{f} = I\boldsymbol{\ell} \times \mathbf{B} \quad (2.9)$$

Laplace's law states that when a conductor with length and direction  $\boldsymbol{\ell}$  conducting a current  $I$  is placed in a magnetic field  $\mathbf{B}$ , a force  $\mathbf{f}$  will act on the conductor in a direction perpendicular to both  $\mathbf{B}$  and  $\boldsymbol{\ell}$ , in accordance with the right-hand rule.

If the conductor is a closed loop, such as a coil, the forces acting on the coil will result in a torque. For a conducting loop enclosing an area  $A$  lying along a plane with normal vector  $\hat{\mathbf{n}}$  (as illustrated in figure 2.6), the magnetic moment  $\boldsymbol{\mu}$  is defined as [5]:

$$\boldsymbol{\mu} = IA\hat{\mathbf{n}} \quad (2.10)$$

For a coil with  $N$  windings, the magnetic moment is simply extended to:

$$\boldsymbol{\mu} = NI A\hat{\mathbf{n}} \quad (2.11)$$

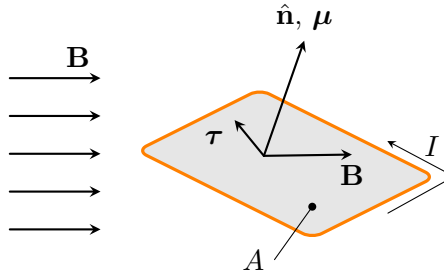


**Figure 2.6:** Illustration of a square-shaped coil with the current  $I$ , enclosing an area  $A$ , in a magnetic field  $\mathbf{B}$ .

The torque  $\tau$  acting on the coil is found as the cross product between the magnetic moment and the magnetic field [5]:

$$\tau = \mu \times \mathbf{B} \quad (2.12)$$

The torque is always perpendicular to both the magnetic moment vector and the magnetic field vector. This means that the torque will always have a direction trying to align the magnetic moment vector and the magnetic field vector.

The circuits and material in the satellite will provide some unintended torque due to Earth's magnetic field as well. Using equation 2.12, the torque due to the magnetic field can be described as:

$$\tau_{\text{md}} = \mu_{\text{sat}} \cdot B_{\text{earth}} \cdot \sin \theta \quad (2.13)$$

where  $\mu_{\text{sat}}$  is the magnetic moment from the satellite,  $B_{\text{earth}}$  is the magnetic field of the Earth and  $\theta$  is the angle between them.

The magnetic field of the Earth is dependent on location and altitude. On the surface of the Earth the magnetic field strength is between 20 to 65  $\mu\text{T}$ , which weakens as the altitude increases, to about 20 to 52.5  $\mu\text{T}$  at 500 km above Earth's surface [2]. Earth's magnetic field is approximate to a dipole magnet, and these poles are located around  $11^\circ$  relative to Earth's geographic poles. Magnetic south is located around the Arctica and the magnetic north is located close to the Antarctica.

The value for  $\mu_{\text{sat}}$  is difficult to determine precisely, but it has been approximated in a master's thesis from 2014 [6], that the magnetic moment is around  $0.01 \text{ Am}^2/\text{kg}$ . So assuming that AAUSAT6 has a mass of 1 kg, then the magnetic moment is  $\mu_{\text{sat}} = 0.01 \text{ Am}^2$ . As explained above, the magnetic field is altitude dependent, and at an altitude of 441 km the magnetic field strength is around 52.5  $\mu\text{T}$  at maximum. Using these values and having  $\theta = 90^\circ$ , the resulting torque due the magnetic disturbance will be  $\tau_{\text{md}} = 525.0 \cdot 10^{-9} \text{ Nm}$ .

If the satellite is equipped with magnetorquers, the magnetorquers can be driven at a certain DC bias to produce an opposite torque to compensate for the magnetic disturbance torque. Depending on how well the magnetic disturbance is known, it is possible to compensate for more or less of the disturbance. In this analysis it will be assumed that the magnetic disturbance is known well enough to be able to compensate for 90% of it using

magnetorquers. The resulting disturbance torque due to residual magnetic disturbance is therefore  $\tau_{\text{md}} = 52.5 \cdot 10^{-9}$  Nm.

### 2.3.5 Summary

In this section the disturbance torques on the satellite was investigated and a worst case scenario was analyzed for each of the four different disturbance torques. The results of these are summarized in table 2.3.

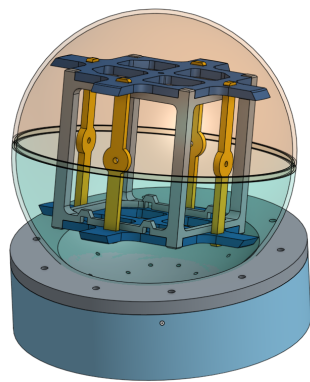
Source of disturbance	Worst case value	Unit
Solar Radiation	$8.2 \cdot 10^{-9}$	Nm
Gravity Gradient	$0.945 \cdot 10^{-9}$	Nm
Aerodynamic Drag	$100.3 \cdot 10^{-9}$	Nm
Magnetic Disturbance	$52.5 \cdot 10^{-9}$	Nm
Total	$113.5 \cdot 10^{-9}$	Nm

**Table 2.3:** Summary of the estimated worst case disturbance torques.

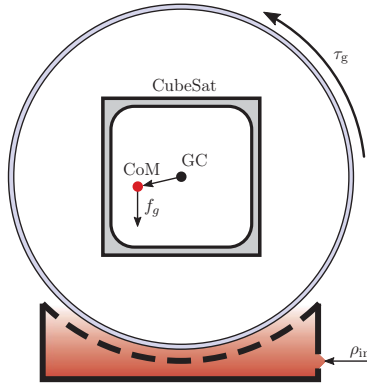
As seen from this table, the most significant disturbance is due to the aerodynamic drag with the second largest being the residual magnetic disturbance. Both of these are very altitude dependent due to Earth's magnetic field and atmosphere, respectively, so at higher altitudes they will be less dominant. It is important to note that these values are very rough estimates. The total disturbance torque is calculated as  $\tau_{\text{totd}} = \sqrt{\tau_{\text{sr}}^2 + \tau_{\text{gg}}^2 + \tau_{\text{ad}}^2 + \tau_{\text{md}}^2}$ , as each of the different sources of disturbance is considered as independent, and therefore it is highly unlikely that all disturbances should summarize, mostly they will neutralize some of the torque other disturbances applies.

## 2.4 Testbed Introduction

For the purpose of ADCS, former students have made a testbed for a CubeSat such that in principle, it is possible to simulate free rotational movement in three dimensions. The testbed is already equipped with reaction wheels as actuators, and the hardware allows for installment of magnetorquers as well. We think of this as a good opportunity to use this testbed. That way we can spend less time on building hardware on our own, while it is possible to implement control algorithms on actual hardware, instead of purely running these algorithms in a simulation - where AAU also have available software libraries, which also offers the opportunity to test initial algorithms, before trying to implement these on the hardware testbed.



(a) Testbed model with enclosed CubeSat.



(b) Sketch of testbed showing the air for lifting the enclosed CubeSat.

**Figure 2.7:** "Shows the CubeSat suspended inside a low mass acrylic ball in the GC (gravity center), where the color gradient illustrates the pressurized air flow and  $\rho_{in}$  is the pressure inlet". Quote and figures from [7].

The testbed is made by former AAU students Brian Gasberg Thomsen and Jens Nielsen as a part of their master's thesis in 2016 [7]. In essence the testbed works like an air hockey table. It uses pressurized air to equalize gravity, to simulate the weightlessness of space. Principally this allows the CubeSat to float within the testbed, such that reaction wheels can spin the CubeSat with little to no friction. Furthermore the testbed is made such that it is possible to fit it inside a Helmholtz coil to simulate Earth's magnetic field, allowing the usage of magnetorquers too. The reaction wheels on the testbed is mounted in a tetrahedron configuration, which requires four reaction wheels, as described in section 4.5.2. An illustration of the testbed can be seen in figure 2.7.

# 3 | Project Scope

As mentioned in the introduction in chapter 1, the requirements to the ADCS of AAUSAT6 are stricter than previous iterations of AAUSAT due to the presumed camera payload. Therefore this project will be based on reaction wheels, as they are able to control the satellite's attitude in three axes with high precision. The satellite will need magnetorquers for momentum dumping eventually, as the reaction wheels will reach saturation at some point, but it has been decided that the focus in this project will be on control using reaction wheels only, with the intention being that magnetorquers and momentum dumping can be implemented later on as part of another project.

It has been decided to use a testbed developed by former AAU students, as this testbed is equipped with reaction wheels (and have the hardware available for implementation of magnetorquers). Based on these initial considerations, the project scope will be narrowed down further.

The project is only focused on making a working attitude control system (ACS) and not an attitude determination system (ADS), since previous AAUSAT satellites already have a working ADS, which should easily be reused in the upcoming AAUSAT6. In addition to this, the testbed available also has a working ADS.

Another important part of an ADCS is detumbling, to keep the satellite from tumbling uncontrollably after launch. This have been successfully implemented in previous AAUSAT satellites as well, and will therefore not be investigated further in this project.

The focus of this project can therefore be summarized in the following problem statement:

*How can a control algorithm be developed that enables a CubeSat to obtain the pointing precision required for a camera payload?*

- *How can this be done through full 3-axes attitude control with basis in the available testbed using reaction wheels for actuation?*

Based on this project delimitation, the requirements of the system will be presented along with test specifications.

## 3.1 Requirements

In this section, the requirements for the ACS will be devised based on the project delimitation. The requirements consist of two different parts: Functional requirements

and technical requirements. All requirements are accompanied by a reasoning for why this requirement is relevant. In addition to this, test specifications are devised as well.

## Functional requirements

### F.1 Keep the camera pointing towards a specific point on Earth

**Reasoning:** When the satellite is supposed to take pictures of a specific area on Earth, it will have to point the camera towards this specific area. It will have to keep this area in its field of view for as long as possible before the satellite reaches a point in its orbit where it is no longer possible for the camera to see the specified area. The same procedure can be used for pointing antennas towards ground stations.

## Technical requirements

### T.1 Nadir pointing: Constant rotational speed of 0.0011 rad/s

**Reasoning:** A good general idle attitude is nadir pointing. This ensures that the satellite is never far away from pointing at a specific point on earth. In nadir mode the satellite focuses towards the center of Earth, making the satellite rotate 360° every orbit. This takes around 98 minutes or 5880 seconds. This gives a mean rotational speed of:

$$\omega_{\text{nad}} = \frac{2\pi \text{ rad}}{5880 \text{ s}} = 0.0011 \text{ rad/s} \quad (3.1)$$

### T.2 Point tracking: Follow the curves in figure 3.2

**Reasoning:** For the satellite to be able to focus at a certain point on earth, the satellite needs to be able to rotate at a certain speed. For the purpose of calculating this rotational speed, we use AAUSAT4 as basis.

In point tracking mode the satellite focuses on a given point on Earth, for as long as possible. This requires the satellite to rotate 180° around itself, as sketched on figure 3.1. This rotation of the satellite happens faster than the nadir mode.

The whole angle of orbit  $\theta_{eo}$  where the satellite has line of sight with the point up until it reaches its peak required rotational speed (the part of the orbit where the satellite has to turn 90° to track the point) can be computed as:

$$\theta_{eo} = \arccos \left( \frac{r_{\text{earth}}}{r_{\text{earth}} + r_{\text{aausat4}}} \right) = 20.78^\circ \quad (3.2)$$

For AAUSAT4 an orbit around Earth takes approximately 5880 seconds (98 minutes), which means that the satellite must rotate 90° in:

$$t_p = \frac{20.78^\circ}{360^\circ} \cdot 5880 \text{ s} = 339 \text{ s} \quad (3.3)$$

This means that at time  $t_0 = 0$ , the satellite can see the horizon of the targeted point on the earth, and at time  $t = 339 \text{ s}$  the satellite is directly above the targeted point on earth. It will be assumed that at  $t_0$ , the satellite will already have made the transition from nadir to pointing mode, since the satellite is assumed to know the point to target long before it has to act on it.

The required rotational speed of the satellite to track the point is dependent on the distance  $r_{sp}$  from the satellite to the tracking point as well as the velocity component perpendicular to this direction. The distance  $r_{sp}$  can be found by the law of cosines, as described in the following:

$$r_{sp} = \sqrt{r_o^2 + r_{\text{earth}}^2 - 2 \cdot r_o \cdot r_{\text{earth}} \cdot \cos \theta} \quad (3.4)$$

where  $r_{\text{earth}}$  is the radius of the Earth (6371 km),  $r_o$  is the minimal distance from the satellite orbit to the center of Earth (the orbit is assumed circular with  $r_o = 6814$  km). All of this is illustrated in figure 3.1.

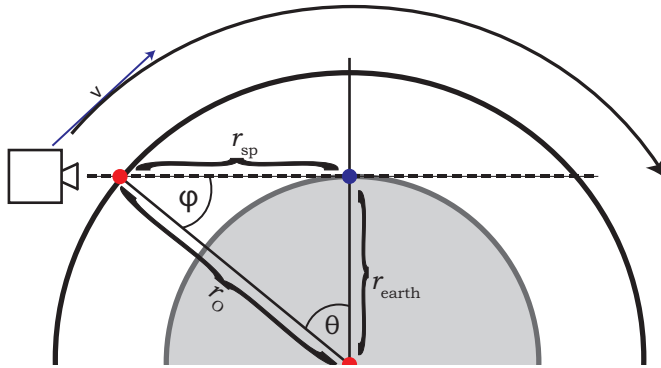


**Figure 3.1:** Illustration of the satellite in point tracking mode.

The velocity component perpendicular to  $r_{sp}$  can be found by:

$$v_p = v \cdot \cos \varphi \quad (3.5)$$

where  $\varphi$  is the angle between  $r_{sp}$  and  $r_o$ , which is the same angle as the angle between the velocity vector  $v$  and the component perpendicular to  $r_{sp}$  (also shown in figure 3.1). This angle is also found using the law of cosines:

$$\varphi = \arccos \left( \frac{r_o^2 + r_{sp}^2 - r_{\text{earth}}^2}{2 \cdot r_o \cdot r_{sp}} \right) \quad (3.6)$$

The required rotational speed of the satellite at a given point can then be found as:

$$\omega_p = \frac{v_p}{r_{sp}} \quad (3.7)$$

A plot of the distance between satellite and tracking point as well as the required rotational speed of the satellite can be seen in figure 3.2.

The shortest distance from satellite to tracking point is when the satellite is directly above the tracking point. Therefore the largest required angular velocity is at this point as well, which is found to be  $\omega_p = 0.0169$  rad/s.

The angle between the satellite and the tracking point will be between 0° and 180° and can be found as the integral of the angular velocity of the satellite. This angle is shown in the last plot in figure 3.2.

For the satellite to be able to perform point tracking, it has to follow the curves in figure 3.2.

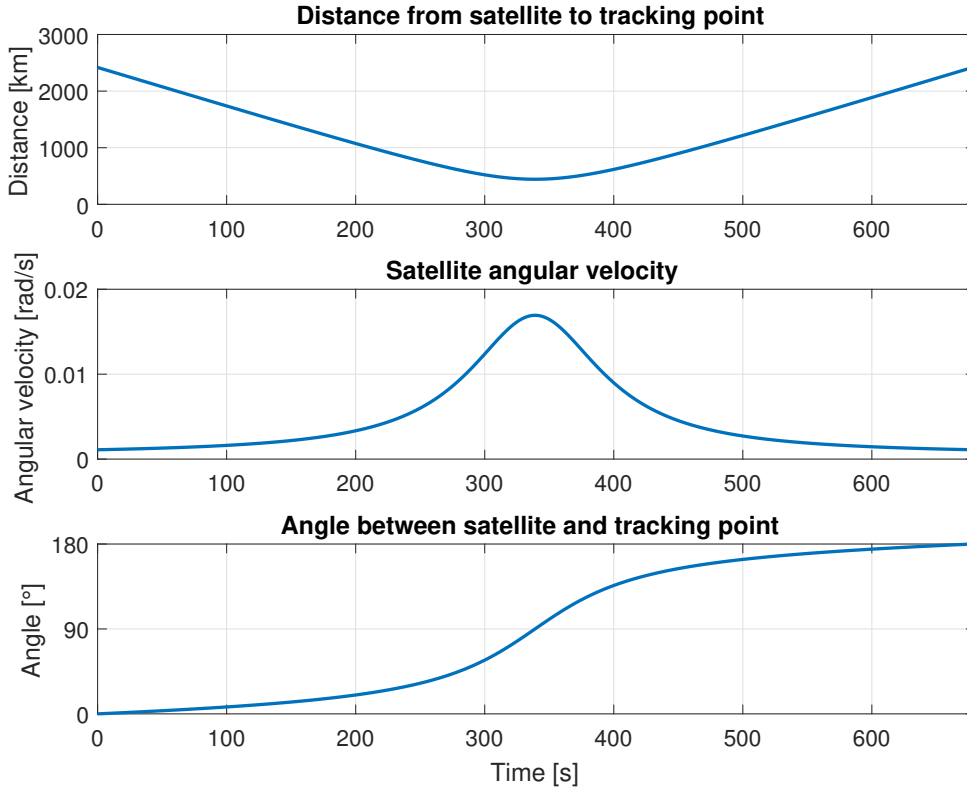


**Figure 3.2:** Plots showing the distance from satellite to tracking point as a function of time, the angular velocity of the satellite as a function of time, and the angle between satellite and tracking point as a function of time.

### T.3 Pointing precision of $\pm 1.241^\circ$

Reasoning: To determine how precise the ACS needs to be, it will be assumed that the satellite is equipped with a camera and that this camera is supposed to take a picture of Jylland, as shown in figure 3.3.

Previously students have investigated the use of a camera in AAUSAT6 as part of a semester project [8]. The camera module used was a C3188A which is an image sensor of the type OV7620 with a lens with focal length  $f = 6$  mm. Therefore this camera will be the one considered in these calculations. The image sensor has a resolution of 640 px  $\times$  480 px with a pixel size of 7.6  $\mu\text{m} \times$  7.6  $\mu\text{m}$ . Based on these values, the field of view of a single pixel, called the instantaneous field of view (IFOV), can be calculated [9]:

$$\theta_{\text{IFOV}} = 2 \cdot \arctan \left( \frac{7.6 \mu\text{m}}{2 \cdot 6 \text{ mm}} \right) = 0.073^\circ \quad (3.8)$$

The area on Earth which a single pixel can capture can be calculated based on the IFOV and the altitude. The pointing precision needs to be the most precise when the satellite is at its lowest altitude which for AAUSAT4 is 441 km. At this altitude, the area on Earth that a single pixel can capture is a square with side length

$$d = 2 \cdot 441 \text{ km} \cdot \tan \left( \frac{\theta_{\text{IFOV}}}{2} \right) = 558.6 \text{ m} \quad (3.9)$$



**Figure 3.3:** The area of Jylland that the camera on the satellite is supposed to capture.

Thus, with the given resolution, the camera can capture an area on Earth of  $357 \text{ km} \times 268 \text{ km}$ .

The area of Jylland approximately fills a square of  $337 \text{ km} \times 185 \text{ km}$ . To be able to capture all of Jylland, the camera pointing can at max be 20 km off, or 10 km to either side. 10 km correspond to  $\frac{10 \text{ km}}{558.6 \text{ m}} = 17 \text{ px}$  which correspond to an angle of  $17 \cdot \theta_{\text{IFOV}} = 1.241^\circ$ .

Based on this case, the pointing requirement of the ACS is therefore  $\pm 1.241^\circ$ .

#### T.4 Step change from nadir mode to point tracking mode

When the satellite is changing from nadir mode to point tracking mode, this is assumed to happen as a step reference change. After this step the satellite should be ready to point the camera at the tracking point. Following the value in equation (3.2), this step has a value of  $90^\circ - 20.78^\circ = 69.22^\circ$ . The two following requirements are related to this step.

##### T.4a 100 seconds settling time

Reasoning: To get the most out of the point tracking maneuver, the satellite must have settled soon after this step has happened. This settling time is arbitrarily chosen as 100 seconds.

##### T.4b Pointing precision of $15.25^\circ$

Reasoning: The pointing precision when changing from nadir to point tracking mode is not nearly as strict as when doing the pointing. The change will happen when the satellite is 2400 km away from the tracking point (see the first plot in figure 3.2). In this distance the area which the camera can see with one pixel is:

$$d_{2400} = 2 \cdot 2400 \text{ km} \cdot \tan\left(\frac{\theta_{\text{IFOV}}}{2}\right) = 3057 \text{ m}$$

when the  $\theta_{IFOV}$  is equal to  $0.073^\circ$  as determined in equation 3.8. This gives an area of a picture equal to:

$$3057 \text{ m} \cdot (640 \text{ px} \times 480 \text{ px}) = 1957 \text{ km} \times 1467 \text{ km}$$

This means that the camera could be  $\frac{1467-185}{2} = \pm 641 \text{ km}$  off and still capture a picture of Jylland. This corresponds to  $\frac{457.5 \text{ km}}{2293 \text{ m}} = 209 \text{ px}$  equal to  $209 \cdot \theta_{IFOV} = 15.25^\circ$ .

## 3.2 Test Specifications

The test specifications specify how the requirements are tested to determine whether the system fulfills the requirements or not.

### A.1 Test of requirement T.1 - Nadir pointing

When testing this requirement, the satellite prototype will be placed within the testbed and commanded to follow a reference which changes with  $\omega_{nad} = 0.0011 \text{ rad/s}$  about one axis. If the satellite is able to follow the reference with an error less than the precision given by requirement T.3, the requirement is considered fulfilled.

### A.2 Test of requirement T.2 - Point tracking

When testing this requirement, the satellite prototype will be placed within the testbed and commanded to follow a reference equal to the angle trajectory given in figure 3.2 about one axis. If the satellite is able to follow the reference with an error less than the precision given by requirement T.3, the requirement is considered fulfilled.

### A.3 Test of requirement T.3 - Pointing precision

Requirement T.3 is tested as part of test A.1 and A.2. If the system fulfills requirement T.1 and T.2, requirement T.3 is considered fulfilled.

### A.4 Test of requirement T.4a - Step change settling time

When testing this requirement, the satellite prototype will be placed within the testbed and commanded to follow a reference changing from one value to another value in a step equal to  $69.22^\circ$  about one axis. If the satellite is able to follow the reference and reach a steady state with an error less than the precision given by requirement T.3 within 100 seconds, the requirement is considered fulfilled.

### A.5 Test of requirement T.4b - Step change pointing precision

When testing this requirement, the satellite prototype will be placed within the testbed and commanded to follow a reference changing from one value to another value in a step equal to  $69.22^\circ$  about one axis. If the satellite is able to follow the reference without having an overshoot equal to  $15.25^\circ$ , the requirement is considered fulfilled.

# 4 | Modeling of the Satellite

In this chapter the mathematical model for the motion of the satellite will be derived. However before this can be done, it will be investigated how to describe the attitude of a satellite in space, and what different options for attitude parametrization exist.

The modeling itself is divided into two parts: A kinematic model describing the attitude of the satellite without taking into account the forces that act upon it, and a dynamic model which will describe the motion of the satellite in relation to the forces acting upon it. In addition to this, models for the reaction wheels will be derived as well.

## 4.1 Attitude Parametrization

An important concept to be familiar with before proceeding is how to parametrize the attitude of the satellite. The attitude can be thought of as one coordinate system representing the satellite body, e.g. the Satellite Reference Frame (SRF), rotated in relation to a specific frame of reference, e.g. the Earth Centered Inertial. This example is illustrated in figure 4.1.

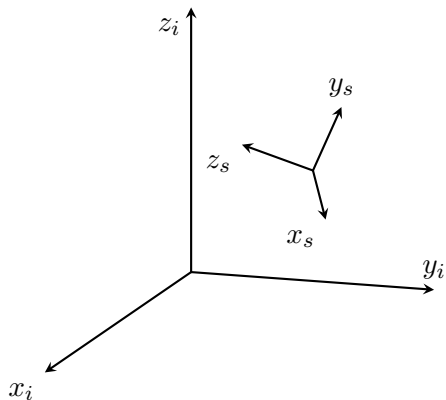


**Figure 4.1:** Illustration of the SRF coordinate system rotated in relation to the ECI coordinate system.

That means that in a known frame of reference, the attitude can simply be described by a rotation matrix. When used to describe an attitude, this rotation matrix is often called the attitude matrix or direction cosine matrix.

A matrix transformation by a rotation matrix  $\mathbf{A}$  in three dimensions preserves the norm and angles between vectors, and  $\mathbf{A}$  is therefore a proper orthogonal  $3 \times 3$  matrix. This

means that the matrix has determinant 1 and satisfies the relation  $\mathbf{A}^{-1} = \mathbf{A}^T$ , that is, the inverse of the matrix is equal to its transpose. If  $\mathbf{A}$  represents a transformation from reference frame to body frame, then  $\mathbf{A}^T$  represents a transformation from body frame to reference frame [2].

There exists several ways to parametrize a rotation matrix which will be considered in the following.

#### 4.1.1 Euler Axis and Angle

For any rotation matrix  $\mathbf{A}$ , there exists an eigenvector  $\hat{\mathbf{e}}$  with corresponding eigenvalue 1 which means this vector is unchanged when multiplied with  $\mathbf{A}$ , i.e.  $\mathbf{A}\hat{\mathbf{e}} = \hat{\mathbf{e}}$ . Therefore the unit vector  $\hat{\mathbf{e}}$  must lie along the axis of rotation.

A rotation around the axis along  $\hat{\mathbf{e}}$  by an angle  $\varphi$  can be described by equation (4.1). This is commonly called the *Euler Axis and Angle* parametrization [2].

$$\mathbf{A}(\hat{\mathbf{e}}, \varphi) = \begin{bmatrix} \cos \varphi + e_1^2(1 - \cos \varphi) & e_1 e_2(1 - \cos \varphi) + e_3 \sin \varphi & e_1 e_3(1 - \cos \varphi) - e_2 \sin \varphi \\ e_1 e_2(1 - \cos \varphi) - e_3 \sin \varphi & \cos \varphi + e_2^2(1 - \cos \varphi) & e_2 e_3(1 - \cos \varphi) + e_1 \sin \varphi \\ e_1 e_3(1 - \cos \varphi) + e_2 \sin \varphi & e_2 e_3(1 - \cos \varphi) - e_1 \sin \varphi & \cos \varphi + e_3^2(1 - \cos \varphi) \end{bmatrix} \quad (4.1)$$

When the axis of rotation is equal to one of the main axes, i.e.  $\hat{\mathbf{e}} = \mathbf{i}, \mathbf{j}$  or  $\mathbf{k}$ , equation (4.1) reduces to (in the case of  $\hat{\mathbf{e}} = \mathbf{i}$ ) equation (4.2).

$$\mathbf{A}_1(\varphi) = \begin{bmatrix} 1 & 0 & 0 \\ 0 & \cos \varphi & \sin \varphi \\ 0 & -\sin \varphi & \cos \varphi \end{bmatrix} \quad (4.2)$$

While this parametrization is quite easy to interpret physically, it has a problem when  $\sin \varphi = 0$ , because in that case the rotation axis cannot be defined [2].

#### 4.1.2 Euler Angles

Another form of parametrization uses three rotation angles, called the *Euler Angles*. This parametrization is defined by successive rotations about some coordinate axes  $i$ ,  $j$ , and  $k$  by angles  $\phi$ ,  $\theta$ , and  $\psi$  respectively. The same coordinate axis can appear two times in the same sequence, as long as two successive rotations are about different axes. This means there are a total of 12 different sequences which can be divided into two different types:

- Type 1: All three axes appear in the sequence, e.g. 1-2-3, 2-1-3, 3-1-2, etc.
- Type 2: Only two different axes appear in the sequence, e.g. 3-1-3, 1-2-1, 2-3-2, etc.

The overall resulting rotation of the rotation sequence can be described by the matrix given in equation (4.3) [2].

$$\mathbf{A}_{ijk}(\phi, \theta, \psi) = \mathbf{A}_k(\psi)\mathbf{A}_j(\theta)\mathbf{A}_i(\phi) \quad (4.3)$$

The Type 1 rotation sequence has a singularity at  $\theta = \pm 90^\circ$ , because in that case the  $\phi$  and  $\psi$  angles cannot be determined uniquely when looking at the resulting direction cosine matrix. Likewise the Type 2 sequence has a singularity at  $\theta = 0^\circ$  and  $\theta = 180^\circ$  [2].

### 4.1.3 Quaternions

Another way of parametrizing an attitude is by the use of quaternions. Quaternions can be considered as hypercomplex numbers of the form  $\mathbf{q} = q_4 + q_1i + q_2j + q_3k$ , where  $i$ ,  $j$  and  $k$  are the imaginary units, or written in another form:

$$\mathbf{q} = \begin{bmatrix} q_1 \\ q_2 \\ q_3 \\ q_4 \end{bmatrix} = \begin{bmatrix} \mathbf{q} \\ q_4 \end{bmatrix} \quad (4.4)$$

The basic properties of quaternions are described in appendix A.

When a quaternion  $\mathbf{q}$  has unit length, that is,

$$q_1^2 + q_2^2 + q_3^2 + q_4^2 = 1, \quad (4.5)$$

then  $\mathbf{q}$  represents a rotation. A rotation about an axis  $\hat{\mathbf{e}}$  by an angle  $\Phi$  can be described by a quaternion having the following values, often called the *Euler Symmetric Parameters* [2]:

$$q_1 = e_1 \sin\left(\frac{\Phi}{2}\right) \quad (4.6a)$$

$$q_2 = e_2 \sin\left(\frac{\Phi}{2}\right) \quad (4.6b)$$

$$q_3 = e_3 \sin\left(\frac{\Phi}{2}\right) \quad (4.6c)$$

$$q_4 = \cos\left(\frac{\Phi}{2}\right) \quad (4.6d)$$

or written in another way:  $\mathbf{q} = q_4 + \mathbf{q} = \cos\left(\frac{\Phi}{2}\right) + \hat{\mathbf{e}} \sin\left(\frac{\Phi}{2}\right)$ .

A vector rotation corresponding to multiplying a rotation matrix  $\mathbf{A}$  with a vector  $\mathbf{v}$ , i.e.  $\mathbf{v}' = \mathbf{Av}$ , can be accomplished using a unit quaternion by the relation given in equation (4.7).

$$\mathbf{v}' = \mathbf{qvq}^* \quad (4.7)$$

The direction cosine matrix corresponding to this operation is given in equation (4.8) [2].

$$\mathbf{A}(\mathbf{q}) = \begin{bmatrix} q_1^2 - q_2^2 - q_3^2 + q_4^2 & 2(q_1q_2 + q_3q_4) & 2(q_1q_3 - q_2q_4) \\ 2(q_1q_2 - q_3q_4) & -q_1^2 + q_2^2 - q_3^2 + q_4^2 & 2(q_2q_3 + q_1q_4) \\ 2(q_1q_3 + q_2q_4) & 2(q_2q_3 - q_1q_4) & -q_1^2 - q_2^2 + q_3^2 + q_4^2 \end{bmatrix} \quad (4.8)$$

Unlike the Euler Axis and Angle parametrization and Euler Angles parametrization described before, the quaternion parametrization does not have any singularities. In

addition to this, it is easy to compute multiple rotations represented by quaternions. Two successive rotations represented by quaternions  $\mathbf{q}$  and  $\mathbf{p}$  can be represented as a single rotation represented by the quaternion product  $\mathbf{qp}$  as shown in equation (4.9) [10].

$$\mathbf{v}'' = \mathbf{p}\mathbf{v}'\mathbf{p}^* = (\mathbf{qp})\mathbf{v}(\mathbf{qp})^* \quad (4.9)$$

The quaternion product can be expressed in matrix notation by equation (4.10).

$$\mathbf{pq} = \begin{bmatrix} p_4 & p_3 & -p_2 & p_1 \\ -p_3 & p_4 & p_1 & p_2 \\ p_2 & -p_1 & p_4 & p_3 \\ -p_1 & -p_2 & -p_3 & p_4 \end{bmatrix} \mathbf{q} \quad (4.10)$$

A practical example of this could arise when translating an attitude given in one frame to another frame. For example, when knowing the attitude of the CRF given in ECI, i.e.  ${}^c_i\mathbf{q}$ , but wanting it in the SRF, i.e.  ${}^s_i\mathbf{q}$ . This can be accomplished by multiplying with the quaternion  ${}^s_c\mathbf{q}$  representing the rotation from CRF to SRF, as shown in equation (4.11):

$${}^s_i\mathbf{q} = {}^s_c\mathbf{q} {}^c_i\mathbf{q} \quad (4.11)$$

In addition to this it can be noted that if  ${}^c_s\mathbf{q}$  describes the rotation from CRF to SRF, then the inverse quaternion corresponds to the rotation from SRF to CRF, as given by equation (4.12):

$${}^c_s\mathbf{q}^* = {}^s_c\mathbf{q} \quad (4.12)$$

#### 4.1.4 Summary

The primary attitude parametrization form used in this project will be the quaternions. However, for analytical purposes the other parametrizations mentioned in this chapter may sometimes be more convenient to use, and therefore these will occasionally be used as well.

## 4.2 Rotational Mechanics

Before modeling the satellite, the relevant quantities needed to describe rotational mechanics will be defined in this subsection. First of all the models are based on angular momentum and torque as variables. Angular momentum  $L$  is the product of the moment of inertia  $I$  and the angular velocity  $\omega$ , written as

$$L = I\omega \quad (4.13)$$

In translational mechanics, this corresponds to momentum, mass and velocity respectively. Torque  $\tau$  corresponds to force in translation and is equal to the time derivative of the angular momentum.

$$\tau = \frac{dL}{dt} = I \frac{d\omega}{dt} \quad (4.14)$$

An important property of angular momentum is that the angular momentum of a system is conserved, unless an external torque is applied. This property is especially important when modeling the reaction wheels.

For rotation in three dimensions, the aforementioned variables will be three dimensional vectors, except for the moment of inertia which is a real symmetric  $3 \times 3$  matrix. Because of this, it has three real eigenvalues and three orthogonal eigenvectors, satisfying the relation

$$\mathbf{I}\hat{\mathbf{p}}_i = I_i\hat{\mathbf{p}}_i \quad \text{for } i = 1, 2, 3 \quad (4.15)$$

where  $\mathbf{I}$  is the inertia matrix,  $I_i$  is the  $i$ 'th eigenvalue and  $\hat{\mathbf{p}}_i$  is the  $i$ 'th eigenvector. This means that every inertia matrix has an eigenvalue decomposition written as

$$\mathbf{I} = \mathbf{P}\mathbf{I}_D\mathbf{P}^T \quad (4.16)$$

where  $\mathbf{P}$  is the orthogonal matrix consisting of the three eigenvectors and  $\mathbf{I}_D$  is the diagonalized inertia matrix. The eigenvalues correspond to the principal moments of inertia and the eigenvectors correspond to the principal axes of the satellite of which the mass is symmetrically distributed. In other words, every inertia matrix can be represented as a diagonal matrix with its principal moments of inertia as the diagonal entries, provided that it is described in the coordinate system corresponding to its principal axes. This coordinate system is, as mentioned in section 2.2, referred to as the Control Reference Frame (CRF) throughout the report and will be used frequently to simplify the calculations involving the moment of inertia of the satellite. Therefore, whenever the inertia matrix appears in an equation, it will be assumed to be of the form given by:

$$\mathbf{I} = \begin{bmatrix} I_1 & 0 & 0 \\ 0 & I_2 & 0 \\ 0 & 0 & I_3 \end{bmatrix} \quad (4.17)$$

A group of students wrote their master's thesis regarding the development of AAUSAT3 [11]. Here they determined the inertia matrix of the satellite within the CRF as:

$${}^c\mathbf{I}_{\text{sat}} = \begin{bmatrix} 0.0017 & 0 & 0 \\ 0 & 0.0022 & 0 \\ 0 & 0 & 0.0022 \end{bmatrix} \quad (4.18)$$

And the rotation from SRF to CRF as:

$${}^s\mathbf{q} = [0.0207 \ 0.7147 \ 0.0073 \ 0.6991]^T \quad (4.19)$$

Since AAUSAT3 and AAUSAT6 have the same standard for the external size of the satellites, and iterations of the other AAUSATs have had the same general structure, the inertia matrix for AAUSAT3 seems as a good basis for AAUSAT6.

### 4.3 Kinematic Model

The kinematic model describes the motion of the satellite without consideration of the forces acting on it. The goal of this derivation is an expression of the time derivative of the attitude of the satellite.

As explained in section 4.1.3, the attitude of the satellite is described using a quaternion  $\mathbf{q}(t)$  given in the ECI reference frame. The attitude at time  $t + \Delta t$ , also given in the ECI frame, is described by the quaternion  $\mathbf{q}(t + \Delta t)$ . The relation between these two attitudes is given by the quaternion  $\mathbf{p}(\Delta t)$  representing the attitude at time  $t + \Delta t$  relative to the attitude at time  $t$ . In other words,  $\mathbf{p}(\Delta t)$  is the attitude at time  $t + \Delta t$  given in the frame defined by  $\mathbf{q}(t)$ . Thus  $\mathbf{q}(t + \Delta t)$  can be expressed by equation (4.20):

$$\mathbf{q}(t + \Delta t) = \mathbf{p}(\Delta t)\mathbf{q}(t) \quad (4.20)$$

The value of the quaternion  $\mathbf{p}$  is according to the Euler symmetric parameters given by

$$\mathbf{p}(\Delta t) = p_4(\Delta t) + \mathbf{p}(\Delta t) = \cos\left(\frac{\Delta\Phi}{2}\right) + \hat{\mathbf{e}} \sin\left(\frac{\Delta\Phi}{2}\right), \quad (4.21)$$

where  $\Delta\Phi$  is the rotated angle along the rotation axis  $\hat{\mathbf{e}}$  in the frame defined by  $\mathbf{q}(t)$ . By using the matrix notation for the quaternion product given by equation (4.10), equation (4.20) can be rewritten to

$$\mathbf{q}(t + \Delta t) = \left( \cos\left(\frac{\Delta\Phi}{2}\right) \mathbf{1} + \sin\left(\frac{\Delta\Phi}{2}\right) \mathbf{E} \right) \mathbf{q}(t) \quad (4.22)$$

where  $\mathbf{1}$  is the  $4 \times 4$  identity matrix and  $\mathbf{E}$  is the skew-symmetric matrix given by

$$\mathbf{E} = \begin{bmatrix} 0 & e_3 & -e_2 & e_1 \\ -e_3 & 0 & e_1 & e_2 \\ e_2 & -e_1 & 0 & e_3 \\ -e_1 & -e_2 & -e_3 & 0 \end{bmatrix} \quad (4.23)$$

The angle  $\Delta\Phi$  is equivalent to the satellite moving with angular velocity  $\omega$  about the rotation axis  $\hat{\mathbf{e}}$  for a time span  $\Delta t$ , that is  $\Delta\Phi = \omega\Delta t$ . By assuming that  $\Delta t$  is sufficiently small, the small angle approximations for cos and sin can be used. These are given by the first order Taylor approximation about the point 0:

$$\cos\left(\frac{\omega\Delta t}{2}\right) \approx 1 \quad \sin\left(\frac{\omega\Delta t}{2}\right) \approx \frac{1}{2}\omega\Delta t \quad (4.24)$$

Using the small angle approximations, equation (4.22) can be rewritten to

$$\mathbf{q}(t + \Delta t) = \left( \mathbf{1} + \frac{1}{2}\boldsymbol{\Omega}\Delta t \right) \mathbf{q}(t) \quad (4.25)$$

where  $\boldsymbol{\Omega}$  is the skew-symmetric matrix given by

$$\boldsymbol{\Omega} = \begin{bmatrix} 0 & \omega_3 & -\omega_2 & \omega_1 \\ -\omega_3 & 0 & \omega_1 & \omega_2 \\ \omega_2 & -\omega_1 & 0 & \omega_3 \\ -\omega_1 & -\omega_2 & -\omega_3 & 0 \end{bmatrix} \quad (4.26)$$

The time derivative of  $\mathbf{q}$  can now be found as the following:

$$\dot{\mathbf{q}} = \frac{d\mathbf{q}}{dt} = \lim_{\Delta t \rightarrow 0} \frac{\mathbf{q}(t + \Delta t) - \mathbf{q}(t)}{\Delta t} = \frac{1}{2}\boldsymbol{\Omega}\mathbf{q} \quad (4.27)$$

Equation (4.27) thus gives the expression for the rate of change in the attitude of the satellite in a given reference frame as a function of the angular velocity.

## 4.4 Dynamic Model

Here we wish to derive an expression for the dynamic model of the satellite, such that the behavior of the satellite can be calculated. We know from Newton that in inertial space, e.g. the ECI reference frame, the relation between angular momentum and torque is:

$$\frac{d^i \mathbf{L}}{dt} = {}^i \dot{\mathbf{L}} = {}^i \boldsymbol{\tau} \quad (4.28)$$

where the vector  $\mathbf{L}$  is the total angular momentum and the vector  $\boldsymbol{\tau}$  is the total applied torque. If we wish to express this relation relative to the CRF, we can multiply with a rotation matrix  $\mathbf{A}$ . Thus the relation between the angular momentum in ECI and CRF is:

$${}^c \mathbf{L} = {}_i^c \mathbf{A} {}^i \mathbf{L} \quad (4.29)$$

Taking the derivative of equation (4.29) using the chain rule yields:

$${}^c \dot{\mathbf{L}} = {}_i^c \dot{\mathbf{A}} {}^i \mathbf{L} + {}_i^c \mathbf{A} {}^i \dot{\mathbf{L}} \quad (4.30)$$

It can be shown that the derivative of a rotation matrix  $\mathbf{A}$  can be written as:

$$\dot{\mathbf{A}} = \boldsymbol{\Omega}' \mathbf{A} \quad (4.31)$$

where  $\boldsymbol{\Omega}'$  is the skew-symmetric matrix given by

$$\boldsymbol{\Omega}' = \begin{bmatrix} 0 & \omega_3 & -\omega_2 \\ -\omega_3 & 0 & \omega_1 \\ \omega_2 & -\omega_1 & 0 \end{bmatrix} \quad (4.32)$$

The derivation of equation (4.31) follows the same procedure as the derivation of the kinematic equation and will therefore not be repeated here.

Substituting equation (4.31) into equation (4.30) yields:

$${}^c \dot{\mathbf{L}} = {}^c \boldsymbol{\Omega}' {}_i^c \mathbf{A} {}^i \mathbf{L} + {}_i^c \mathbf{A} {}^i \dot{\mathbf{L}} \quad (4.33)$$

Recognizing that  ${}^i \mathbf{L}$  rotated by  ${}_i^c \mathbf{A}$  is equivalent to  ${}^c \mathbf{L}$ , equation (4.33) can be rewritten to:

$${}^c \dot{\mathbf{L}} = {}^c \boldsymbol{\Omega}' {}^c \mathbf{L} + {}_i^c \mathbf{A} {}^i \dot{\mathbf{L}} \quad (4.34)$$

Now since  $\boldsymbol{\Omega}'$  is a skew-symmetric matrix, the multiplication of  $\boldsymbol{\Omega}'$  and  $\mathbf{L}$  can be written as the cross product between the vector  $-\boldsymbol{\omega}$  and  $\mathbf{L}$ . Furthermore, the derivative of  $\mathbf{L}$  yields the torque  $\boldsymbol{\tau}$ , which is also rotated by  ${}_i^c \mathbf{A}$  into the CRF, giving  ${}^c \boldsymbol{\tau}$ .

$$\begin{aligned} {}^c \dot{\mathbf{L}} &= -{}^c \boldsymbol{\omega} \times {}^c \mathbf{L} + {}_i^c \mathbf{A} {}^i \dot{\mathbf{L}} \\ &= -{}^c \boldsymbol{\omega} \times {}^c \mathbf{L} + {}_i^c \mathbf{A} {}^i \boldsymbol{\tau} \\ &= -{}^c \boldsymbol{\omega} \times {}^c \mathbf{L} + {}^c \boldsymbol{\tau} \end{aligned} \quad (4.35)$$

Lastly the angular momentums can be considered as the product of the inertia matrix  $\mathbf{I}$  and the angular velocity vector  $\boldsymbol{\omega}$ :

$$\mathbf{I} {}^c \dot{\boldsymbol{\omega}} = {}^c \boldsymbol{\tau} - {}^c \boldsymbol{\omega} \times {}^c \mathbf{L} = {}^c \boldsymbol{\tau} - {}^c \boldsymbol{\omega} \times (\mathbf{I} {}^c \boldsymbol{\omega}) \quad (4.36)$$

Equation (4.36) is the basic equation of attitude dynamics as seen in the CRF. Because all the quantities in equation (4.36) are described in the same reference frame, the reference frame prescripts will be omitted further on, and unless otherwise specified, it will be assumed to be in the CRF.

The applied torque  $\tau$  is the sum of all external and internal torques, such as torques due to environmental disturbances and actuators. This can be expanded to become:

$$\tau = \tau_{\text{dist}} + \tau_{\text{rwc}} + \tau_{\text{mt}} \quad (4.37)$$

where  $\tau_{\text{dist}}$  is the disturbance torque,  $\tau_{\text{rwc}}$  is the control torque from the reaction wheels and  $\tau_{\text{mt}}$  is the control torque from the magnetorquers.

The term  $\omega \times (\mathbf{I}\omega)$  is due to the Coriolis effect, which results in nutation. This is present whenever the instantaneous rotation axis  $\omega$  is not parallel to a principal axis. The consequence of nutation is, as evident from equation (4.36), that the angular momentum is non-zero even when no external torque is applied.

It is now possible to use this equation to control the satellite. The equation is not linear however. The nonlinearity occurs because  $\omega \times (\mathbf{I}\omega)$  yields a vector containing the product of multiple variables.

#### 4.4.1 Dynamic Model with Reaction Wheels

When a wheel is spinning, it has an angular momentum  $h$ . As described in section 4.2, a change in angular momentum results in a torque  $\tau$ . By using this relation, it is possible to use a wheel as a way to generate a torque by changing its angular velocity, and this is why a reaction wheel can be used as an actuator for satellite attitude control. This relation is summarized in equation (4.38) in vector notation:

$$\dot{\mathbf{h}}_{\text{rw}} = \mathbf{I}_{\text{rw}}\dot{\omega}_{\text{rw}} = \tau_{\text{rw}} \quad (4.38)$$

When a reaction wheel is part of the satellite, the satellite dynamics will change. The total angular momentum of the satellite will now include the angular momentum of the reaction wheels as well:

$$\mathbf{L}_{\text{tot}} = \mathbf{I}_s\omega_s + \mathbf{h}_{\text{rw}} \quad (4.39)$$

where the matrix  $\mathbf{I}_s$  is the total moment of inertia of the satellite including the mass of the reaction wheels, and the vector  $\omega_s$  is the angular velocity of the satellite. Returning to the dynamic model of the satellite in equation (4.36), this can be extended to contain reaction wheels by substitution of equation (4.39) as follows:

$$\begin{aligned} \mathbf{I}_s\dot{\omega}_s + \dot{\mathbf{h}}_{\text{rw}} &= \tau - \omega_s \times (\mathbf{I}_s\omega_s + \mathbf{h}_{\text{rw}}) \\ \mathbf{I}_s\dot{\omega}_s + \tau_{\text{rw}} &= \tau - \omega_s \times (\mathbf{I}_s\omega_s + \mathbf{h}_{\text{rw}}) \\ \mathbf{I}_s\dot{\omega}_s &= \tau - \tau_{\text{rw}} - \omega_s \times (\mathbf{I}_s\omega_s + \mathbf{h}_{\text{rw}}) \end{aligned} \quad (4.40)$$

As seen from the derivation of this equation, the torque from the reaction wheels is not an external torque, but rather an internal torque. This means that the reaction wheels do not change the total angular momentum of the satellite, but only redistributes it. In other

words, when the reaction wheels are changing their angular velocity, the angular velocity of the satellite will change, but in the opposite direction. It is therefore apparent from equation (4.40) that the direction of the torque applied to the satellite from the reaction wheels will be opposite that generated by the reaction wheels, which agrees with Newton's third law. However, to be consistent with the sign of the control torques, we will use the following notation:

$$\boldsymbol{\tau}_{\text{rwc}} = -\boldsymbol{\tau}_{\text{rw}} \quad (4.41)$$

Thus the dynamic model can be written as

$$\mathbf{I}_s \dot{\boldsymbol{\omega}}_s = \boldsymbol{\tau}_{\text{dist}} + \boldsymbol{\tau}_{\text{rwc}} + \boldsymbol{\tau}_{\text{mt}} - \boldsymbol{\omega}_s \times (\mathbf{I}_s \boldsymbol{\omega}_s + \mathbf{h}_{\text{rw}}) \quad (4.42)$$

where  $\boldsymbol{\tau}_{\text{dist}}$  and  $\boldsymbol{\tau}_{\text{mt}}$  are the external torques from disturbances and the magnetorquers.

## 4.5 Reaction Wheels and DC Motors

The reaction wheels in the satellite are driven by DC motors. This requires having models of the motor dynamics, models of how the reaction wheels are placed inside the satellite body, and the considerations of a suitable bias point.

The DC motors used in the testbed are Maxon flat motors 362790 [12], and have the key parameters summarized in table 4.1. The motor friction and moment of inertia for the reaction wheels (including motors) are approximated by Thomsen and Jensen [7].

Parameter	Symbol	Value	Unit
Motor armature resistance	$R_a$	4.44	$\Omega$
Motor armature inductance	$L_a$	$0.12 \cdot 10^{-3}$	H
Motor constant / generator constant	$K_e, K_t$	$1.81 \cdot 10^{-3}$	Nm/A
Motor friction	$b$	$63.90 \cdot 10^{-9}$	Nm·s
Combined moment of inertia for wheel and motor	$I_{\text{rw}}$	$0.38 \cdot 10^{-6}$	kg · m <sup>2</sup>
Mechanical time constant (without reaction wheels)	$\tau_{\text{mech}}$	$32.10 \cdot 10^{-3}$	s

Table 4.1: List of essential motor parameters.

### 4.5.1 Reaction wheels driven by a DC motor

To drive the reaction wheels a DC motor will be used. Therefore it is desired to have a model of the reaction wheels involving the torque of the reaction wheels and an input voltage. The mechanical part of the DC motor with a mounted reaction wheel is shown in figure 4.2.

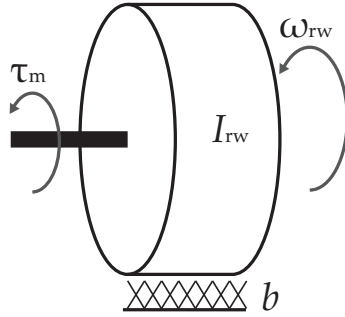


**Figure 4.2:** Mechanical diagram of a reaction wheel mounted on a DC motor.

Based on this model, the following equation can be written.

$$I_{rw}\dot{\omega}_{rw} = \tau_m - b\omega_{rw} = \tau_{rw} \quad (4.43)$$

where  $I_{rw}$  is the moment of inertia of both the reaction wheel and the DC motor, and  $b$  is the friction in the motor. The torque  $\tau_m$  is the torque delivered by the DC motor and is given as  $K_t \cdot i_a$ , where  $K_t$  is the motor constant and  $i_a$  is the armature current.

The electrical model of the DC motor is given by the circuit in figure 4.3.

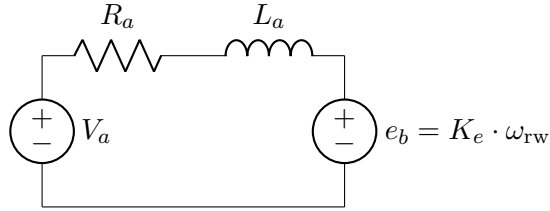


**Figure 4.3:** Electrical model for a DC motor.

Using Kirchoff's voltage law, the electrical model can be described by the following equation.

$$V_a = R_a \cdot i_a + L_a \frac{di_a}{dt} + e_b \quad (4.44)$$

where  $V_a$  is the applied voltage,  $R_a$  is the armature resistance,  $L_a$  is the armature inductance and  $i_a$  is the armature current. The term  $e_b$  is the back EMF of the motor, given by  $e_b = K_e \cdot \omega_{rw}$ , where  $K_e$  is the generator constant, and  $\omega_{rw}$  is the angular velocity of the motor.

According to the datasheet for the DC motor [12], the mechanical time constant is 32.1 ms, which will become larger when a reaction wheel is mounted. The electrical time constant is  $\frac{L_a}{R_a} = 0.027$  ms, so the electrical time constant is insignificant compared to the mechanical. Combining equation (4.43) and (4.44) is therefore most easily done by first assuming that the armature inductance  $L_a$  is small enough to be neglected. By setting  $L_a = 0$ , the two equations are easily combined by solving for  $i_a$  in equation (4.44) and inserting it into

equation (4.43). This yields the following equation:

$$\begin{aligned} I_{\text{rw}} \dot{\omega}_{\text{rw}} &= K_t \frac{V_a - K_e \omega_{\text{rw}}}{R_a} - b \omega_{\text{rw}} \\ &= \frac{K_t}{R_a} V_a - \left( \frac{K_t K_e}{R_a} + b \right) \omega_{\text{rw}} = \tau_{\text{rw}} \end{aligned} \quad (4.45)$$

Equation (4.45) gives an expression for the reaction wheel torque based on the armature voltage of the DC motor for a single reaction wheel. However, to get an expression for the total reaction wheel torque from all four of the reaction wheels used in the testbed in relation to the CRF, the reaction wheel configuration has to be taken into consideration. This will be investigated in the following.

#### 4.5.2 Reaction wheels in a tetrahedron configuration

The four reaction wheels on the testbed are placed in a tetrahedron (triangular pyramid) configuration as shown in figure 4.4.

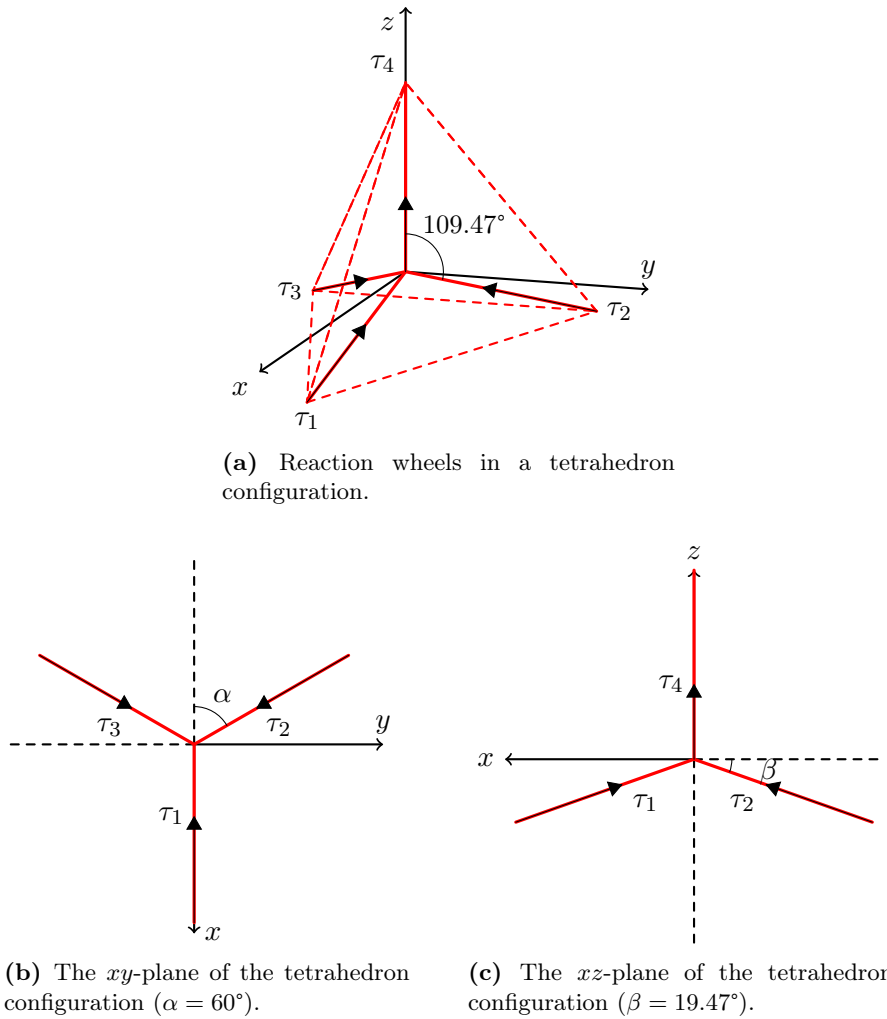


**Figure 4.4:** The tetrahedron configuration seen from different sides. The arrows indicate the torque vectors from the reaction wheels.

We want to express the torque from the reaction wheels in relation to the CRF. This is done by projecting the torque from each reaction wheel onto the axes in the CRF. For a

tetrahedron configuration like the one shown in figure 4.4, this can be expressed as follows [7, 13]:

$${}^c\tau_x = \tau_1 \cos \beta - \tau_2 \cos \beta \cos \alpha - \tau_3 \cos \beta \cos \alpha \quad (4.46a)$$

$${}^c\tau_y = \tau_2 \cos \beta \cos \frac{\alpha}{2} - \tau_3 \cos \beta \cos \frac{\alpha}{2} \quad (4.46b)$$

$${}^c\tau_z = -\tau_1 \sin \beta - \tau_2 \sin \beta - \tau_3 \sin \beta + \tau_4 \quad (4.46c)$$

In vector form this can be written as

$$\begin{bmatrix} {}^c\tau_x \\ {}^c\tau_y \\ {}^c\tau_z \end{bmatrix} = \mathbf{P} \begin{bmatrix} \tau_1 \\ \tau_2 \\ \tau_3 \\ \tau_4 \end{bmatrix} \quad (4.47)$$

where  $\mathbf{P}$  is the  $3 \times 4$  distribution matrix given by

$$\begin{aligned} \mathbf{P} &= \begin{bmatrix} \cos \beta & -\cos \beta \cos \alpha & -\cos \beta \cos \alpha & 0 \\ 0 & \cos \beta \cos \frac{\alpha}{2} & -\cos \beta \cos \frac{\alpha}{2} & 0 \\ -\sin \beta & -\sin \beta & -\sin \beta & 1 \end{bmatrix} \\ &= \begin{bmatrix} 0.94 & -0.47 & -0.47 & 0 \\ 0 & 0.82 & -0.82 & 0 \\ -0.33 & -0.33 & -0.33 & 1 \end{bmatrix} \end{aligned} \quad (4.48)$$

When looking at the distribution matrix for the tetrahedron configuration, it is evident that it is possible for the reaction wheel torques to cancel each other out in each axis when the value of the torques are the same. This means that it is possible to spin the reaction wheels up to a bias point without affecting the resulting torque on the satellite. It also means that it is possible to apply twice the amount of torque on an axis if the direction of the torques canceling each other out are reversed.

#### 4.5.3 Reaction wheel bias point

For the reaction wheels a bias point is used, because having the reaction wheels driving at or near its zero velocity is only for short term operation, in the sense that it wears harder on the motor driving them. Without a bias the reaction wheels will wear out faster after launch, besides the fact that the mechanical nature of the motors also gives them limited time before breaking, making it worse. In addition to this, the dry friction at zero velocity is nonlinear, which makes it harder to design a controller. The idea of a bias is illustrated in figure 4.5.

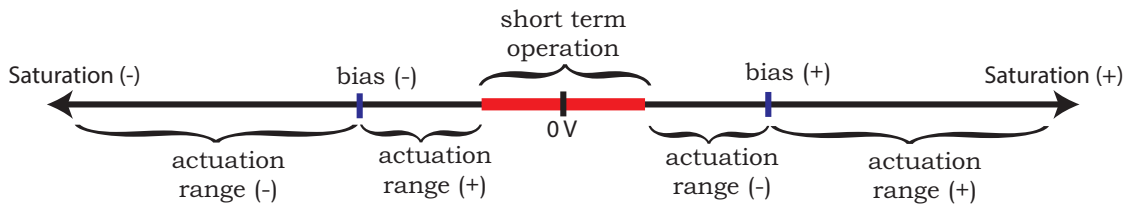


**Figure 4.5:** Illustration of how the bias point influences the actuation range.

The choice of bias point creates a new problem, because driving the reaction wheels costs power, which is a limited resource, so a compromise is needed. Typically it is desired to have the reaction wheels at a bias, which allows enough momentum to perform the current task without saturating the reaction wheels and without reaching zero velocity. For example, a slew maneuver requires greater range of actuation than stabilization, and therefore a higher bias. So the bias point will be an estimation of the needed range of actuation, based on the current task of the satellite.

For the satellite to track a point on Earth, as described in the requirement specification in section 3.1, the reaction wheels need to provide a certain amount of torque. Based on the trajectory shown in figure 3.2 on page 18, this torque can be calculated.

The required angular acceleration  $\alpha_p$  of the satellite can be found as the time derivative of the rotational speed:

$$\alpha_p = \frac{d\omega_p}{dt} \quad (4.49)$$

This is equivalent to the torque  $\tau_p$ :

$$\tau_p = \alpha_p \cdot I_{\text{sat},y} \quad (4.50)$$

The required torque as a function of time can be seen in the first plot in figure 4.6. Here it is seen that the largest instantaneous required torque is around  $350 \cdot 10^{-9}$  Nm.

The acceleration needed by the reaction wheel to provide the required torque can be found as:

$$\alpha_{\text{rw}} = \frac{\tau_p}{I_{\text{rw}}} \quad (4.51)$$

The rotational speed of the reaction wheel can then be found by integrating the acceleration over the duration of the tracking maneuver:

$$\omega_{\text{rw}} = \int_{t_0}^{t_1} \alpha_{\text{rw}} dt \quad (4.52)$$

In addition to the torque required by the tracking maneuver, the reaction wheels have to overcome the environmental disturbance torques as well. If the environmental torques are assumed to be constant for the duration of the tracking maneuver, this will be seen as an offset in the torque curve in figure 3.2. In figure 4.6, the required acceleration by the reaction wheel is shown with and without a disturbance torque offset equal to the worst case environmental torque (found to be  $113.5 \cdot 10^{-9}$  Nm in section 2.3). In the same figure is shown the rotational speed of the reaction wheel with and without the disturbance torque.

As seen from the plots, the tracking maneuver itself only requires the reaction wheel to spin up to around 90 rad/s or 870 RPM, with the worst case environmental disturbance torque being the dominant torque to overcome. Without any environmental torques to overcome, a suitable bias point would be around 150 rad/s or 1500 RPM as this would be enough to perform the tracking maneuver in either direction with a small safety margin. With a constant disturbance torque, the reaction wheels would reach saturation at some

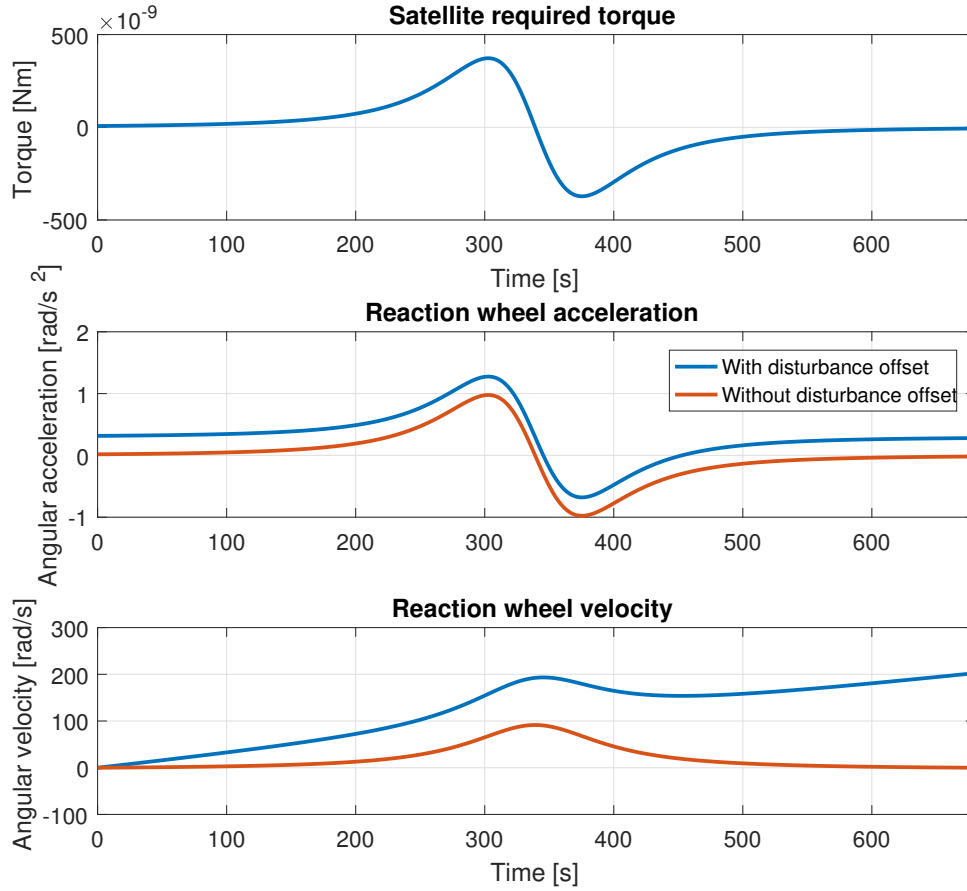


**Figure 4.6:** Plots showing the reaction wheel acceleration and the reaction wheel velocity with and without the disturbance torque.

point no matter what, but assuming that the environmental torque is only constant for the duration of the tracking maneuver, the required actuation range would be around 200 rad/s or 2000 RPM as seen from the lower plot in figure 4.6. A suitable bias point would thus be 314.16 rad/s equal to about 3000 RPM.

### Bias power consumption

When the reaction wheels are running at constant rotational speed at this bias, the resulting torque is zero, and this means the torque delivered by the motor is equal to the motor friction from table 4.1, as described by the following equation:

$$0 = \tau_m - b\omega_{rw} \quad (4.53)$$

$$\tau_m = b\omega_{rw} = 63.9 \cdot 10^{-9} \text{ Nms} \cdot 314.16 \text{ rad/s} = 20.08 \cdot 10^{-6} \text{ Nm}$$

Knowing the torque delivered by the motor, it is possible to calculate the armature current as follows:

$$I_a = \frac{\tau_m}{K_t} = 11.09 \text{ mA} \quad (4.54)$$

Based on the armature current, the armature voltage can be calculated using the electrical motor model described by equation (4.44). Because the current in the bias is considered to be constant, the inductance term will be zero. The armature voltage is thus:

$$V_a = R_a \cdot I_a + K_e \cdot \omega_{rw} = 0.618 \text{ V} \quad (4.55)$$

Knowing both the armature current and armature voltage at the bias point, the consumed power for each motor at the bias point can be calculated as:

$$I_a \cdot V_a = 6.86 \text{ mW} \quad (4.56)$$

The four reaction wheels thus consume approximately a total of 27.5 mW when driving at the bias point.



# 5 | Controller Design

In this chapter the attitude controller for the satellite will be designed based on analysis done in the  $s$ -domain. This is done by first investigating the simplified case of control in one axis. The dynamics related to rotation in other axes are here omitted to make the general properties of the system more clear.

Next the case of control in three axes will be considered. First the dynamic model of the satellite is linearized and converted to the  $s$ -domain, and then a controller is designed and verified based on simulations of the linearized system.

## 5.1 Attitude Control in One Axis

Before designing an attitude controller for attitude in three dimensions, we will first consider the case for attitude control of one axis. A general block diagram for attitude control in one axis is shown in figure 5.1.

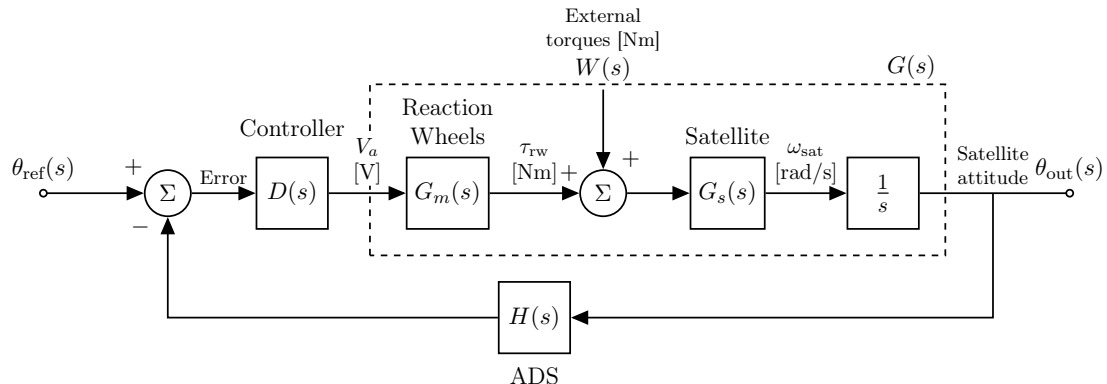


**Figure 5.1:** Block diagram of the attitude controller for one axis.

As seen in the figure, the input is an attitude reference described by an angle about the axis which we wish to control, and the output is the satellite attitude, also described by an angle about the same axis. The block diagram consists of a controller  $D(s)$ , which outputs a voltage to the DC motors driving the reaction wheels. The motor dynamics are found in the transfer function  $G_m(s)$ , whose output is the reaction wheel torque, which is input to the satellite dynamics described by  $G_s(s)$ . In addition to the reaction wheel torque, the external torques  $W(s)$  from the environment is input to  $G_s(s)$  as well and is seen as a disturbance. The output of  $G_s(s)$  is the angular velocity of the satellite, so in order to get the satellite angle, the angular velocity has to be integrated with respect to time. The

combination of  $G_m(s)$ ,  $G_s(s)$  and the integrator  $\frac{1}{s}$  will be referred to as the plant  $G(s)$ . Finally, in the feedback path a sensor block  $H(s)$  is placed, but this will just assumed to be a unity gain block unless specified otherwise.

In order to design a controller, the plant transfer function has to be known. This will be investigated in the following.

### 5.1.1 Plant transfer function

In section 4.4.1 it was found that the reaction wheels can be described by the following equation:

$$\tau_{rw}(t) = I_{rw} \dot{\omega}_{rw}(t) = V_a(t) \cdot \frac{K_e}{R_a} - \omega_{rw}(t) \cdot \left( b + \frac{K_e K_t}{R_a} \right) \quad (5.1)$$

Laplace-transforming this equation yields:

$$sI_{rw} \omega_{rw}(s) = V_a(s) \cdot \frac{K_e}{R_a} - \omega_{rw}(s) \cdot \left( b + \frac{K_e K_t}{R_a} \right) \quad (5.2)$$

The term  $\omega_{rw}$  can be written as:

$$\omega_{rw}(s) = \frac{\tau_{rw}}{sI_{rw}} \quad (5.3)$$

By substituting this into equation (5.2), it can be rearranged to form the following transfer function from armature voltage to reaction wheel torque, equivalent to  $G_m(s)$  in the block diagram in figure 5.1:

$$G_m(s) = \frac{\tau_{rw}(s)}{V_a(s)} = \frac{s \frac{I_{rw} K_e}{K_t K_e + b R_a}}{s \frac{I_{rw} R_a}{K_t K_e + b R_a} + 1} \quad (5.4)$$

In section 4.4 the satellite dynamics was described. However, for one axis it is greatly simplified and is simply given by the following equation (assuming the external torques from magnetorquers and disturbances are zero):

$$I \dot{\omega}_{sat}(t) = -\tau_{rw}(t) \quad (5.5)$$

Laplace-transforming this equation yields:

$$sI_{sat} \omega_{sat}(s) = -\tau_{rw}(s) \quad (5.6)$$

This can be rearranged to form the following transfer function from output torque of the reaction wheels to rotational speed of the satellite, equivalent to  $G_s(s)$  in the block diagram in figure 5.1:

$$G_s(s) = \frac{\omega_{sat}(s)}{\tau_{rw}(s)} = -\frac{1}{sI_{sat}} \quad (5.7)$$

Multiplying the two transfer functions from equation (5.4) and (5.7) will result in the transfer function from armature voltage to satellite rotational speed:

$$\frac{\omega_{sat}(s)}{V_a(s)} = \frac{\tau_{rw}(s)}{V_a(s)} \cdot \frac{\omega_{sat}(s)}{\tau_{rw}(s)} = -\frac{\frac{I_{rw}}{I_{sat}} \frac{K_e}{K_t K_e + b R_a}}{s \frac{I_{rw} R_a}{K_t K_e + b R_a} + 1} \quad (5.8)$$

To get the attitude of the satellite, we would have to use the kinematic equation derived in section 4.3. However, as we are only considering one axis, the attitude is just described by an angle  $\theta$  which can simply be found by integrating the angular velocity with respect to time, which in the  $s$ -domain corresponds to multiplying with  $\frac{1}{s}$ . This will result in the following transfer function:

$$G(s) = \frac{\theta_{\text{out}}(s)}{V_a(s)} = \frac{\omega_{\text{sat}}(s)}{V_a(s)} \cdot \frac{1}{s} = -\frac{\frac{I_{\text{rw}}}{I_{\text{sat}}} \frac{K_e}{K_t K_e + b R_a}}{s^2 \frac{I_{\text{rw}} R_a}{K_t K_e + b R_a} + s} \quad (5.9)$$

### 5.1.2 System Analysis

Now that the transfer function for the plant has been determined, it is possible to design a controller. In this analysis we will consider attitude control about the  $z$ -axis, using the values listed in table 4.1. In all the following considerations, it will be assumed that  $H(s) = 1$ .

First we will consider the case of a simple proportional controller with gain  $K$ . In this case the open loop transfer function is given by:

$$\begin{aligned} \text{Open loop} &= D(s)G(s)H(s) \\ &= -K \frac{\frac{I_{\text{rw}}}{I_{\text{sat}}} \frac{K_e}{K_t K_e + b R_a}}{s^2 \frac{I_{\text{rw}} R_a}{K_t K_e + b R_a} + s} = -K \frac{0.0881}{0.4753s^2 + s} \end{aligned} \quad (5.10)$$

To see how this gain affects the closed loop pole placements, we will look at the root locus. This can for positive gains be seen in figure 5.2a. A root locus diagram shows how the system's poles "moves" as a function of the gain, enabling the user to see specific gain ranges that might lead to instability of the system. Furthermore it is possible to interpret the damping factor, and here by the overshoot of a step response, by looking at the pole location with respect to the imaginary axis.

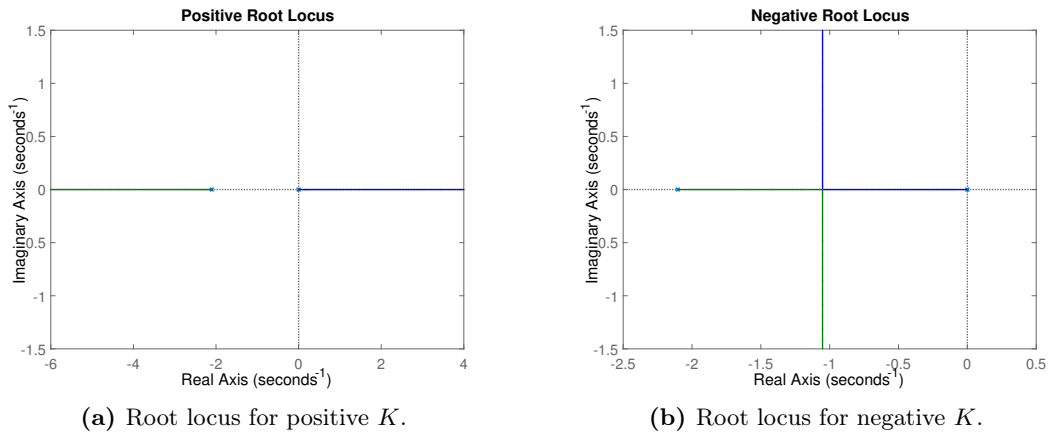


**Figure 5.2:** Root locus of the system.

As can be seen from the root locus, the closed loop system will have a pole in the right half plane for gains  $K > 0$ . The reason for this is the negative sign in  $G_2(s)$ , which arises due to the nature of how the reaction wheels interact with the satellite. Therefore to

compensate for this negative sign, the gain has to be negative to make the system stable. A root locus for negative gains is shown in figure 5.2b, where it can be seen that the poles will be strictly in the left half plane for gains  $K < 0$ .

Another way to verify the stability of the system is by making a bode plot of the open loop transfer function. This is shown in figure 5.3 with the controller gain and feedback simply set to  $-1$  and  $1$  respectively.

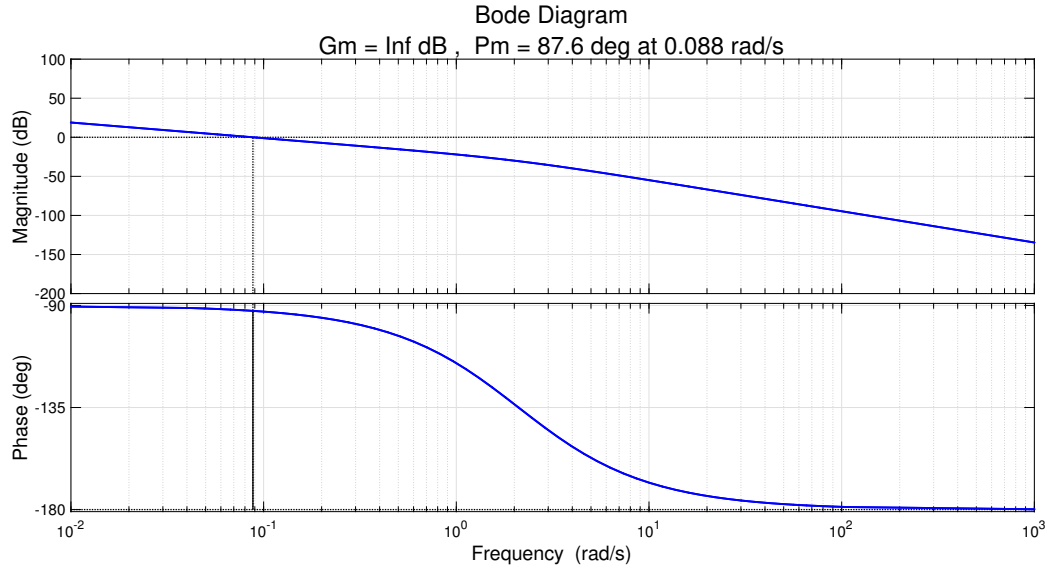


**Figure 5.3:** Bode plot of the open loop system.

As seen from the bode plot, the phase margin is  $87.6^\circ$  and the gain margin is infinite, which means the system is stable. A rule of thumb says that the gain margin has to be at least  $45^\circ$ . The gain can thus be increased a lot before reaching this point.

There are two different cases that are of interest when designing the attitude controller. One is how the system reacts to an input on the reference, and the other is how the system reacts to an input on the disturbance.

To get a grasp of how the satellite behaves in the time domain we will look at the step responses of the closed loop system. The closed loop transfer function from reference to output is given by:

$$\begin{aligned} \frac{\theta_{\text{out}}(s)}{\theta_{\text{ref}}(s)} &= \frac{D(s)G(s)}{1 + D(s)G(s)H(s)} \\ &= -\frac{K \frac{K_e}{I_{\text{sat}}R_a}}{s^2 + \frac{K_e K_t + b R_a}{I_{\text{rw}} R_a} s - K \frac{K_e}{I_{\text{sat}} R_a}} = -\frac{K \cdot 0.1853}{s^2 + 2.1038s - K \cdot 0.1853} \end{aligned} \quad (5.11)$$

The closed loop transfer function from the disturbances to the attitude can be obtained

as:

$$\begin{aligned} \frac{\theta_{\text{out}}(s)}{W(s)} &= \frac{G_s(s) \frac{1}{s}}{1 + G_s(s) \frac{1}{s} H(s) D(s) G_m(s)} \\ &= -\frac{1}{I_{\text{sat}}} \cdot \frac{s + \frac{K_e K_t + b R_a}{I_{\text{rw}} R_a}}{s^3 + \frac{K_e K_t + b R_a}{I_{\text{rw}} R_a} s^2 - K \frac{K_e}{I_{\text{sat}} R_a} s} = -454.54 \cdot \frac{s + 2.1038}{s^3 + 2.1038 s^2 - K \cdot 0.1853 s} \end{aligned} \quad (5.12)$$

The step response of the closed loop system for both a step on the reference and on the disturbance, respectively, can be seen in figure 5.4. For the reference input, the amplitude is 1, and for the input on the disturbance the amplitude of the step is  $113.5 \cdot 10^{-9}$ , which is equal to the sum of the worst case disturbance torques discussed in section 2.3.

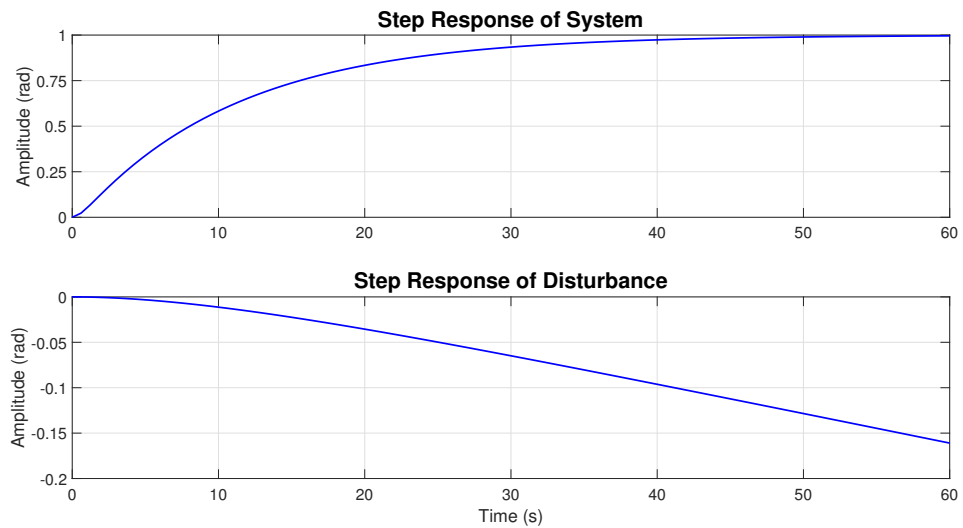


**Figure 5.4:** Step response of the closed loop system for a unit step input on the reference (above) and for a step input on the disturbance with amplitude  $113.5 \cdot 10^{-9}$  (below).

From the response to the step input on the reference it can be seen that the system is quite slow to. By increasing the gain of the controller, the system will get a faster response.

From the response to the step input on the disturbance it is evident that the system has no disturbance rejection, and that the steady state error goes towards infinity with a constant input at the disturbance. A solution to this problem is to add an integrator to the controller, but this will be discussed further when the three axis control is analyzed.

Transfer functions for the other axes will be similar. And while the goal is to design an three axes ACS, only minor details will differ with respect to the given axis, the argument being that if the control works for one axis, there is a good chance that similar results is gained from the same controller in three axes. In the next section the case of three-axes control will be investigated.

## 5.2 Attitude Control in Three Axes

A general block diagram for attitude control in three axes is shown in figure 5.5

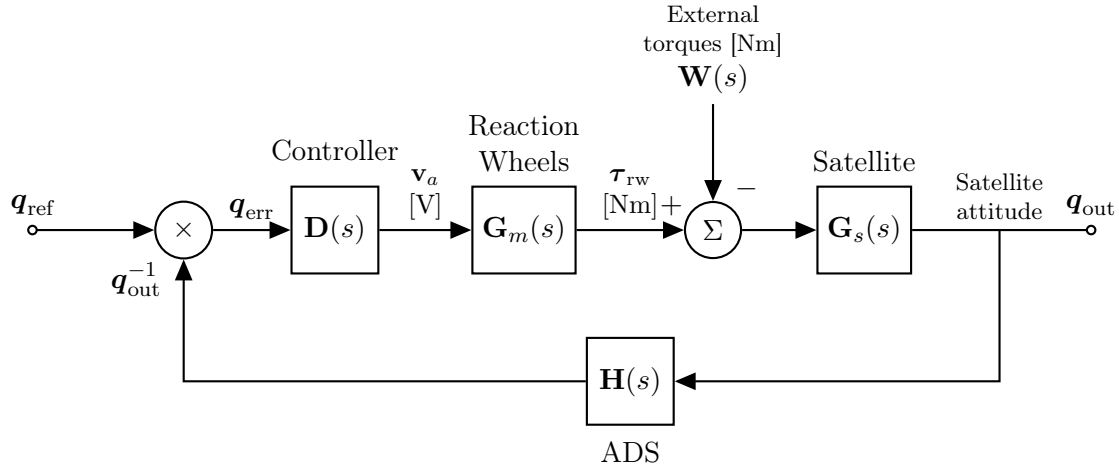


**Figure 5.5:** Block diagram of the attitude controller in three axes.

Compared to the diagram for one axis control in figure 5.1, the three axes controller is very similar. The main difference is that this system is a MIMO (multiple-input multiple-output) system with three inputs and three outputs. This means every block is a  $3 \times 3$  transfer function matrix and every signal is a  $3 \times 1$  vector, except for the attitude which is parametrized using quaternions. This means that instead of finding the error by subtracting the output from the reference input in the feedback loop, the error is instead found by multiplying the reference input quaternion by the inverse of the output quaternion, that is  $\mathbf{q}_{\text{err}} = \mathbf{q}_{\text{out}}^{-1} \mathbf{q}_{\text{ref}}$ .

As was the case for the one axis control considerations, the plant transfer function matrix has to be found before designing a controller. This is not as straightforward as in the one axis case, because each axis has an impact on the two remaining axes. A good option for finding the transfer matrix is by first writing the satellite models as a state-space model.

The reason to use state space for multiple axis control, is its convenience of how the state-space models handles MIMO systems. While the use of state-space representations often happen with systems in time domain, it can still be used to represent systems in the frequency domain as long as the system is an LTI system (Linear Time-Invariant system).

The state-space representation has the following form:

$$\begin{aligned}\dot{\mathbf{x}}(t) &= \mathbf{Ax}(t) + \mathbf{Bu}(t) \\ \mathbf{y}(t) &= \mathbf{Cx}(t) + \mathbf{Du}(t)\end{aligned}\tag{5.13}$$

where:

- |                                     |  |
|-------------------------------------|--|
| $\mathbf{x}(t)$ is the state vector | $\mathbf{y}(t)$ is the output vector   |
| $\mathbf{u}(t)$ is the input vector | $\mathbf{C}$ is the feedforward matrix |
| $\mathbf{A}$ is the state matrix    | $\mathbf{D}$ is the output matrix      |
| $\mathbf{B}$ is the input matrix    |  |

Laplace transforming equation (5.13) yields:

$$\begin{aligned}s\mathbf{X}(s) &= \mathbf{AX}(s) + \mathbf{BU}(s) \\ \mathbf{Y}(s) &= \mathbf{CX}(s) + \mathbf{DU}(s)\end{aligned}\tag{5.14}$$

As mentioned before, equation (5.14) is only valid for linear systems. The equation for the kinematic model (4.27) and the dynamic model (4.36) can be rearranged and written as:

$$\begin{bmatrix} \dot{\mathbf{q}} \\ \dot{\boldsymbol{\omega}}_s \\ \dot{\mathbf{h}}_{rw} \end{bmatrix} = \begin{bmatrix} \frac{1}{2}\Omega\mathbf{q} \\ \mathbf{I}_s^{-1}(\boldsymbol{\tau} - \boldsymbol{\omega}_s \times (\mathbf{I}_s \boldsymbol{\omega}_s + \mathbf{h}_{rw})) \\ -\boldsymbol{\tau}_{rw} \end{bmatrix} \quad (5.15)$$

These equations are not linear, so in order to be able to Laplace transform the state-space representation of these equations, they have to be linearized.

### 5.2.1 Linearization of dynamic model

The dynamic equation of motion 4.36 with the addition of reaction wheels becomes:

$$\mathbf{I}_s \dot{\boldsymbol{\omega}}_s = \boldsymbol{\tau} - \boldsymbol{\omega}_s \times (\mathbf{I}_s \boldsymbol{\omega}_s + \mathbf{h}_{rw}) \quad (5.16)$$

Splitting all the variables  $\boldsymbol{\omega}$ ,  $\boldsymbol{\tau}$  and  $\mathbf{h}$  in equation (5.16) into the sum of an operating point value (indicated with a bar) and a small signal value (indicated by a tilde) representing small deviations from the operation point will result in equation (5.17):

$$\mathbf{I}_s(\dot{\boldsymbol{\omega}}_s + \dot{\tilde{\boldsymbol{\omega}}}_s) = \bar{\boldsymbol{\tau}} + \tilde{\boldsymbol{\tau}} - (\bar{\boldsymbol{\omega}}_s + \tilde{\boldsymbol{\omega}}_s) \times (\mathbf{I}_s(\bar{\boldsymbol{\omega}}_s + \tilde{\boldsymbol{\omega}}_s) + \bar{\mathbf{h}}_{rw} + \tilde{\mathbf{h}}_{rw}) \quad (5.17)$$

The nonlinear terms in equation (5.17) are linearized by a first order Taylor approximation around the operating point. The first order Taylor approximation of the term  $\boldsymbol{\tau}$  is already explicitly written in equation (5.17).

The first order Taylor approximation of the cross product  $\boldsymbol{\omega}_s \times (\mathbf{I}_s \boldsymbol{\omega}_s + \mathbf{h}_{rw})$  is given by the equation :

$$\boldsymbol{\omega}_s \times (\mathbf{I}_s \boldsymbol{\omega}_s + \mathbf{h}_{rw}) \approx \bar{\boldsymbol{\omega}}_s \times (\mathbf{I}_s \bar{\boldsymbol{\omega}}_s + \bar{\mathbf{h}}_{rw}) + \mathbf{J}_{cp} \Big|_{\bar{\boldsymbol{\omega}}_s, \bar{\mathbf{h}}_{rw}} \begin{bmatrix} \tilde{\boldsymbol{\omega}}_s \\ \tilde{\mathbf{h}}_{rw} \end{bmatrix} \quad (5.18)$$

where  $\mathbf{J}_{cp}$  is the Jacobian matrix of the vector resulting from the cross product  $\boldsymbol{\omega} \times (\mathbf{I}\boldsymbol{\omega} + \mathbf{h}_{rw})$ . This vector is written explicitly in equation (5.19):

$$\boldsymbol{\omega}_s \times (\mathbf{I}_s \boldsymbol{\omega}_s + \mathbf{h}_{rw}) = \begin{bmatrix} -I_2\omega_2\omega_3 + I_3\omega_3\omega_2 - \omega_{s3}h_{rw2} + \omega_{s2}h_{rw3} \\ I_1\omega_1\omega_3 - I_3\omega_3\omega_1 + \omega_{s1}h_{rw1} - \omega_{s3}h_{rw3} \\ -I_1\omega_2\omega_1 + I_2\omega_2\omega_1 - \omega_{s2}h_{rw1} + \omega_{s1}h_{rw2} \end{bmatrix} \quad (5.19)$$

The Jacobian matrix contains the derivatives of each element in the vector with respect to each variable. It is written out explicitly in equation (5.20):

$$\mathbf{J}_{cp} = \begin{bmatrix} 0 & I_{s3}\omega_{s3} - I_2\omega_{s3} + h_{rw3} & I_{s3}\omega_{s2} - I_{s2}\omega_{s2} - h_{rw2} & 0 & -\omega_{s3} & \omega_{s2} \\ I_{s1}\omega_{s3} - I_{s3}\omega_{s3} - h_{rw3} & 0 & I_{s1}\omega_{s1} - I_{s3}\omega_{s1} + h_{rw1} & \omega_{s3} & 0 & -\omega_{s1} \\ I_{s2}\omega_{s2} - I_{s1}\omega_{s2} + h_{rw2} & I_{s2}\omega_{s1} - I_1\omega_1 - h_{rw1} & 0 & -\omega_{s2} & \omega_{s1} & 0 \end{bmatrix} \quad (5.20)$$

Inserting the Taylor approximation of  $\boldsymbol{\omega}_s \times (\mathbf{I}_s \boldsymbol{\omega}_s + \mathbf{h}_{rw})$  in equation (5.17) results in the linearized model given by equation (5.21):

$$\mathbf{I}_s(\dot{\boldsymbol{\omega}}_s + \dot{\tilde{\boldsymbol{\omega}}}_s) \approx \bar{\boldsymbol{\tau}} + \tilde{\boldsymbol{\tau}} - \left( \bar{\boldsymbol{\omega}}_s \times (\mathbf{I}_s \bar{\boldsymbol{\omega}}_s + \bar{\mathbf{h}}_{rw}) + \mathbf{J}_{cp} \Big|_{\bar{\boldsymbol{\omega}}_s, \bar{\mathbf{h}}_{rw}} \begin{bmatrix} \tilde{\boldsymbol{\omega}}_s \\ \tilde{\mathbf{h}}_{rw} \end{bmatrix} \right) \quad (5.21)$$

The small signal equation is found by subtracting the operation point, which results in equation (5.22):

$$\mathbf{I}_s \dot{\tilde{\boldsymbol{\omega}}}_s \approx \tilde{\boldsymbol{\tau}} - \mathbf{J}_{cp} \Big|_{\bar{\boldsymbol{\omega}}, \bar{\mathbf{h}}_{rw}} \begin{bmatrix} \tilde{\boldsymbol{\omega}}_s \\ \tilde{\mathbf{h}}_{rw} \end{bmatrix} \quad (5.22)$$

This equation is linear and describes the dynamics for small perturbations about an arbitrary operating point.

### 5.2.2 Linearization of kinematic model

The kinematic model was in section 4.3 found to be:

$$\dot{\mathbf{q}} = \frac{1}{2} \boldsymbol{\Omega} \mathbf{q} \quad (5.23)$$

where  $\boldsymbol{\Omega}$  is the skew-symmetric matrix given by

$$\boldsymbol{\Omega} = \begin{bmatrix} 0 & \omega_3 & -\omega_2 & \omega_1 \\ -\omega_3 & 0 & \omega_1 & \omega_2 \\ \omega_2 & -\omega_1 & 0 & \omega_3 \\ -\omega_1 & -\omega_2 & -\omega_3 & 0 \end{bmatrix} \quad (5.24)$$

To get a linearized small signal approximation we cannot use the normal Taylor approximation directly, as it is not possible to add two quaternions. Instead we must look at how the quaternion was defined to begin with.

The quaternion is defined by the Euler symmetric parameters, as described in section 4.1.3. We will now decide to have our operating point to be  $\tilde{\Phi} = 0$ , i.e.  $\tilde{\mathbf{q}} = [0 \ 0 \ 0 \ 1]^T$ . The quaternion small signal value  $\tilde{\mathbf{q}}$  about this operating point can thus be approximated by using the small angle approximations for sin and cos in the Euler symmetric parameters, as shown in equation (5.25):

$$\tilde{\mathbf{q}} = \begin{bmatrix} \tilde{q}_1 \\ \tilde{q}_2 \\ \tilde{q}_3 \\ \tilde{q}_4 \end{bmatrix} = \begin{bmatrix} e_1 \sin\left(\frac{\tilde{\Phi}}{2}\right) \\ e_2 \sin\left(\frac{\tilde{\Phi}}{2}\right) \\ e_3 \sin\left(\frac{\tilde{\Phi}}{2}\right) \\ \cos\left(\frac{\tilde{\Phi}}{2}\right) \end{bmatrix} \approx \begin{bmatrix} \frac{1}{2}\tilde{\omega}_1 dt \\ \frac{1}{2}\tilde{\omega}_2 dt \\ \frac{1}{2}\tilde{\omega}_3 dt \\ 1 \end{bmatrix} \quad (5.25)$$

Substituting  $\mathbf{q}$  with  $\tilde{\mathbf{q}}$  in equation (5.23) and letting  $dt \rightarrow 0$  will thus give the derivative of the quaternion small signal, resulting in:

$$\dot{\tilde{\mathbf{q}}} = \begin{bmatrix} \dot{\tilde{q}}_1 \\ \dot{\tilde{q}}_2 \\ \dot{\tilde{q}}_3 \\ \dot{\tilde{q}}_4 \end{bmatrix} = \frac{1}{2} \boldsymbol{\Omega} \tilde{\mathbf{q}} = \begin{bmatrix} \frac{1}{2}\tilde{\boldsymbol{\omega}} \\ 0 \end{bmatrix} \quad (5.26)$$

Equation (5.26) is linear and describes the kinematics for small perturbations in the attitude.

### 5.2.3 Linear state-space model

A linearized model for the state of the system has now been derived. The summary of the linearized model is given as equation (5.27):

$$\begin{bmatrix} \dot{\tilde{\mathbf{q}}} \\ \dot{\tilde{\boldsymbol{\omega}}}_s \\ \dot{\tilde{\mathbf{h}}}_{\text{rw}} \end{bmatrix} = \begin{bmatrix} \frac{1}{2}\tilde{\boldsymbol{\omega}}_s \\ \mathbf{I}_s^{-1} \left( \tilde{\boldsymbol{\tau}} - \mathbf{J}_{\text{cp}} \Big|_{\bar{\boldsymbol{\omega}}_s, \bar{\mathbf{h}}_{\text{rw}}} \begin{bmatrix} \tilde{\boldsymbol{\omega}}_s & \tilde{\mathbf{h}}_{\text{rw}} \end{bmatrix}^T \right) \\ -\tilde{\boldsymbol{\tau}}_{\text{rwc}} \end{bmatrix} \quad (5.27)$$

Equation (5.27) can then be split up into the matrices **A**, **B**, **C** and **D**, and the vectors **X**, **U** and **Y**. The state vector **X** is containing the satellite's angular velocity, current attitude and angular momentum of the reaction wheels:

$$\mathbf{x} = \begin{bmatrix} \tilde{\boldsymbol{\omega}}_{s1} & \tilde{\boldsymbol{\omega}}_{s2} & \tilde{\boldsymbol{\omega}}_{s3} & \tilde{q}_1 & \tilde{q}_2 & \tilde{q}_3 & \tilde{\mathbf{h}}_1 & \tilde{\mathbf{h}}_2 & \tilde{\mathbf{h}}_3 \end{bmatrix}^T \quad (5.28)$$

The matrix **A** describes how these states relate to each other, which yields the following  $9 \times 9$  matrix, where  $\dots$  indicate three zeros:

$$\mathbf{A} = \begin{bmatrix} 0 & -\frac{\bar{h}_3 - I_{s2}\bar{\omega}_{s3} + I_{s3}\bar{\omega}_{s2}}{I_{s1}} & \frac{\bar{h}_2 + I_{s2}\bar{\omega}_{s2} - I_{s3}\bar{\omega}_{s2}}{I_{s1}} & \dots & 0 & \frac{\bar{\omega}_{s3}}{I_{s1}} & -\frac{\bar{\omega}_{s2}}{I_{s1}} \\ \frac{\bar{h}_3 - I_{s1}\bar{\omega}_{s3} + I_{s3}\bar{\omega}_{s2}}{I_{s2}} & 0 & -\frac{\bar{h}_1 + I_{s1}\bar{\omega}_{s1} - I_{s3}\bar{\omega}_{s1}}{I_{s2}} & \dots & -\frac{\bar{\omega}_{s3}}{I_{s2}} & 0 & \frac{\bar{\omega}_{s1}}{I_{s2}} \\ -\frac{\bar{h}_2 - I_{s1}\bar{\omega}_{s2} + I_{s2}\bar{\omega}_{s1}}{I_{s3}} & \frac{\bar{h}_1 + I_{s1}\bar{\omega}_{s1} - I_{s2}\bar{\omega}_{s1}}{I_{s3}} & 0 & \dots & \frac{\bar{\omega}_{s2}}{I_{s3}} & -\frac{\bar{\omega}_{s1}}{I_{s3}} & 0 \\ \frac{1}{2} & 0 & 0 & \dots & 0 & 0 & 0 \\ 0 & \frac{1}{2} & 0 & \dots & 0 & 0 & 0 \\ 0 & 0 & \frac{1}{2} & \dots & 0 & 0 & 0 \\ 0 & 0 & 0 & \dots & 0 & 0 & 0 \\ 0 & 0 & 0 & \dots & 0 & 0 & 0 \\ 0 & 0 & 0 & \dots & 0 & 0 & 0 \end{bmatrix} \quad (5.29)$$

Next is the input vector **U**, containing the control torque from the reaction wheels:

$$\mathbf{u} = \begin{bmatrix} \tilde{\tau}_{\text{rwc1}} & \tilde{\tau}_{\text{rwc2}} & \tilde{\tau}_{\text{rwc3}} \end{bmatrix}^T \quad (5.30)$$

The  $9 \times 3$  input matrix **B** describes how the input relates to the other states of the system and is given by:

$$\mathbf{B} = \begin{bmatrix} I_{s1}^{-1} & 0 & 0 \\ 0 & I_{s2}^{-1} & 0 \\ 0 & 0 & I_{s3}^{-1} \\ \vdots & \vdots & \vdots \\ -1 & 0 & 0 \\ 0 & -1 & 0 \\ 0 & 0 & -1 \end{bmatrix} \quad (5.31)$$

The output of the system is the quaternion, so the output vector **Y** is given as:

$$\mathbf{y} = \begin{bmatrix} \tilde{q}_1 & \tilde{q}_2 & \tilde{q}_3 \end{bmatrix}^T \quad (5.32)$$

The output matrix  $\mathbf{C}$  describes how the output relates to the states, which results in a  $3 \times 9$  output matrix:

$$\mathbf{C} = \begin{bmatrix} 0 & 0 & 0 & 1 & 0 & 0 & 0 & 0 & 0 \\ 0 & 0 & 0 & 0 & 1 & 0 & 0 & 0 & 0 \\ 0 & 0 & 0 & 0 & 0 & 0 & 1 & 0 & 0 \end{bmatrix} \quad (5.33)$$

And lastly the feedforward matrix  $\mathbf{D}$  only contains zeros because the system does not have any feedforward.

Before inserting the values of the satellite, the operating points have to be determined.

### Choice of operating points

The operating point of the satellite is chosen based on nadir pointing as this is assumed to be the default mode. In this mode, the satellite is rotating about the  $y$ -axis with an angular velocity of one rotation per orbit, which is equal to 0.0011 rad/s, as described in the requirements in section 3.1. Since the rotation is counterclockwise, the operating point becomes:

$$\bar{\omega}_s = [0 \ -0.0011 \ 0]^T \text{ rad/s} \quad (5.34)$$

The operating point of the angular momentum of the reaction wheels is based on the bias point of the reaction wheels. However, if all four reaction wheels in the tetrahedron configuration are driving with the same rotational speed, the angular momentums will cancel each other out, as described in section 4.4.1, and the resulting angular momentum will be zero. The operating point for the angular momentum of the reaction wheels is therefore chosen to be zero:

$$\bar{\mathbf{h}}_{rw} = [0 \ 0 \ 0]^T \quad (5.35)$$

#### 5.2.4 System analysis

Now that the operating points have been chosen, the transfer function matrix for the satellite dynamics can be calculated. Inserting the values for the satellite's moment of inertia and the operating point values into the matrices will reduce the state matrix  $\mathbf{A}$  to the following:

$$\mathbf{A} = \begin{bmatrix} 0 & 0 & 0 & 0 & 0 & 0 & 0 & 0 & 0.6471 \\ 0 & 0 & 0 & 0 & 0 & 0 & 0 & 0 & 0 \\ 0.0003 & 0 & 0 & 0 & 0 & 0 & -0.5000 & 0 & 0 \\ 0.5000 & 0 & 0 & 0 & 0 & 0 & 0 & 0 & 0 \\ 0 & 0.5000 & 0 & 0 & 0 & 0 & 0 & 0 & 0 \\ 0 & 0 & 0.5000 & 0 & 0 & 0 & 0 & 0 & 0 \\ 0 & 0 & 0 & 0 & 0 & 0 & 0 & 0 & 0 \\ 0 & 0 & 0 & 0 & 0 & 0 & 0 & 0 & 0 \\ 0 & 0 & 0 & 0 & 0 & 0 & 0 & 0 & 0 \end{bmatrix} \quad (5.36)$$

As can be seen, most of the elements are reduced to zero because of the operating points and because the moment of inertia of the satellite is equal in the  $y$ - and  $z$ -axis.

Now that the state-space representation has been defined based on the linear equations of motion, it can safely be Laplace transformed. Equation (5.14) can be rearranged to the following, where  $\mathbf{1}$  is the  $3 \times 3$  identity matrix:

$$\mathbf{Y}(s) = (\mathbf{C}(s\mathbf{1} - \mathbf{A})^{-1} \mathbf{B} + \mathbf{D}) \mathbf{U}(s) \quad (5.37)$$

This equation can be used to arrive at a transfer function matrix, containing 3 inputs and 3 outputs. Inserting the values into equation (5.37) will result in the following transfer matrix, describing the attitude quaternion relative to the input reaction wheel torque:

$$\mathbf{G}_s(s) = \begin{bmatrix} \frac{294.1}{s^2} & 0 & \frac{0.3235}{s^3} \\ 0 & \frac{227.3}{s^2} & 0 \\ \frac{-0.3235}{s^3} & 0 & \frac{227.6s^2 - 80.88 \cdot 10^{-6}}{s^4} \end{bmatrix} \quad (5.38)$$

To get the transfer matrix from input armature voltage on the motors to the attitude quaternion, the transfer matrix for the motor dynamics has to be multiplied onto  $\mathbf{G}_s(s)$ . The motor transfer function was found as equation (5.4) in section 5.1. When values for the motor parameters are inserted into the transfer function of the motors,  $G_m(s)$  becomes:

$$G_m(s) = \frac{0.1938 \cdot 10^{-3}s}{0.4753s + 1} \quad (5.39)$$

The four motors driving the reaction wheels in the tetrahedron configuration are assumed to be identical, and the tetrahedron distribution matrix will be disregarded in the transfer functions for the system, and only be considered during the implementation of the controller. Because the motors are modeled linearly, the dynamics will be the same regardless of the distribution matrix. The motor transfer matrix will therefore be a diagonal  $3 \times 3$  matrix, where the diagonal elements are given by  $G_m(s)$ . This matrix is written as:

$$\mathbf{G}_m(s) = \begin{bmatrix} \frac{0.1938 \cdot 10^{-3}s}{0.4753s+1} & 0 & 0 \\ 0 & \frac{0.1938 \cdot 10^{-3}s}{0.4753s+1} & 0 \\ 0 & 0 & \frac{0.1938 \cdot 10^{-3}s}{0.4753s+1} \end{bmatrix} \quad (5.40)$$

The total transfer matrix for the satellite from input voltage to output attitude is thus given by  $\mathbf{G}_{\text{tot}}(s) = \mathbf{G}_m(s) \cdot \mathbf{G}_s(s)$ :

$$\mathbf{G}_{\text{tot}}(s) = \begin{bmatrix} \frac{0.12}{s^2 + 2.1s} & 0 & \frac{1.32 \cdot 10^{-4}}{s^3 + 2.1s^2} \\ 0 & \frac{0.0926}{s^2 + 2.1s} & 0 \\ -\frac{1.32 \cdot 10^{-4}}{s^3 + 2.1s^2} & 0 & \frac{0.0926s^2 - 3.3 \cdot 10^{-8}}{s^4 + 2.1s^3} \end{bmatrix} \quad (5.41)$$

This transfer function matrix describes how the attitude of the satellite is influenced by the control torque from the reaction wheels. As can be seen from the matrix, the attitude in the  $x$ - and  $z$ -axis depends on the input to both the  $x$ - and  $z$ -axis reaction wheel. However, it is difficult to see how big this dependence is just by looking at the matrix. One way to quantify the amount of interaction between each input and each output is by the use of a Relative Gain Array (RGA).

The RGA gives the ratio between the gain for one loop when all other loops are open and the gain for one loop when all loops are closed [14].

For example, the first output  $y_1$  is given by:

$$y_1(s) = G_{11}(s)u_1(s) + G_{12}(s)u_2(s) + G_{13}(s)u_3(s) \quad (5.42)$$

The gain from  $u_1$  to  $y_1$  when all other loops are open is equivalent to other inputs being zero. This yields:

$$\frac{y_1(s)}{u_1(s)} \Big|_{u_2=u_3=0} = G_{11}(s) \quad (5.43)$$

The gain from  $u_1$  to  $y_1$  when all other loops are closed is equivalent to all other outputs being zero (assuming perfect control, i.e. the error is zero):

$$\frac{y_1}{u_1} \Big|_{y_2=y_3=0} \quad (5.44)$$

This equation can be found by algebraic manipulation of equation (5.42) and the two similar equations for the two remaining axes. However, for more than two input/output pairs this quickly gets tedious.

The (1,1) entry in the RGA is then the ratio between equation (5.43) and (5.44), and similarly the other entries will be the ratio in relation to the other input/output combinations. This can be generalized to form the full RGA, given as the following equation, where  $\cdot *$  denotes element wise multiplication [14]:

$$\mathbf{R} = \mathbf{G}(s) \cdot * \mathbf{G}(s)^{-T} \quad (5.45)$$

The assumption about perfect control in equation (5.44) only holds for steady state (i.e.  $s = 0$ ), but due to the poles at zero in the satellite dynamics, evaluating the RGA at  $s = 0$  will not yield any useful results in this case. However, the RGA is still a useful approximation at other frequencies [14]. Therefore, the RGA for the satellite dynamics is evaluated at the frequencies 0.01 Hz to 10 Hz. These values are chosen based on the sample rate of the testbed, which is 10 Hz. The RGAs at these frequencies are shown in equation (5.46):

$$\mathbf{R}(j0.02\pi) = \begin{bmatrix} 0.9996 & 0 & 0.0004 \\ 0 & 1 & 0 \\ 0.0004 & 0 & 0.9996 \end{bmatrix} \quad \mathbf{R}(j20\pi) = \begin{bmatrix} 1 & 0 & 0 \\ 0 & 1 & 0 \\ 0 & 0 & 1 \end{bmatrix} \quad (5.46)$$

Because the RGA describes the relative gain between different cases, the rows and columns in the RGA all sum to 1. When looking at the resulting RGAs above, it is evident that the diagonal values are close to 1, which means that the influence from the other inputs is very low. Because the contribution from the other axes are negligible, we can choose to completely ignore all the off-diagonal entries in the transfer function matrix and instead consider the complete satellite dynamic system as three SISO systems with the input-output pairings 1-1, 2-2 and 3-3. This means that three different controllers, one for each

axis, need to be designed. The respective transfer functions for each axis are thus:

$$G_x(s) = \frac{0.12}{s^2 + 2.1s} \quad (5.47a)$$

$$G_y(s) = \frac{0.0926}{s^2 + 2.1s} \quad (5.47b)$$

$$G_z(s) = \frac{0.0926s^2 - 3.3 \cdot 10^{-8}}{s^4 + 2.1s^3} \quad (5.47c)$$

It can be seen that  $G_x(s)$  and  $G_y(s)$  are both of the same form as the system considered in the one axis case in section 5.1. However,  $G_z(s)$  is vastly different. It has three poles in 0 and one pole in -2.1, and two zeros in  $\pm 0.6$ . This is quite a problematic combination when the loop is closed, because it results in a closed loop pole in the right half plane, which makes the system unstable. This is evident when looking at the root locus in figure 5.8a, which is plotted for a proportional controller with gain  $K$ .

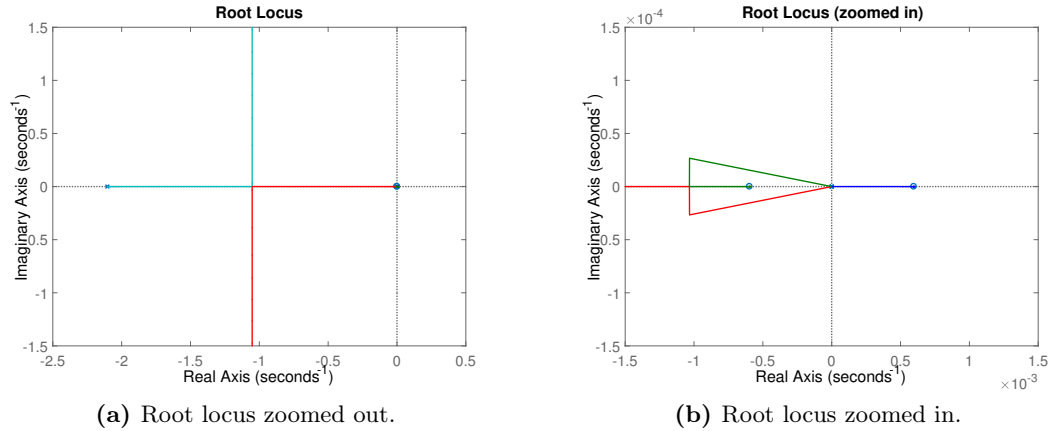


**Figure 5.6:** Root locus for  $G_z(s)$  with a proportional controller.

As can be seen in from the root locus, the RHP zero attracts one of the poles in origin as the gain increases. Most traditional controllers such as PID, lead, lag and notch will not be able to help this problem, as one of the main rules of the root locus say that for  $n$  poles and  $m$  zeros, the  $m$  poles will move toward and end up in a zero as the gain increases.

One way to help this problem is by doing a pole-zero cancellation on the RPH zero. In practice, it will never be possible to place a pole in exactly the same spot as the zero, and because this requires placing a pole in the RHP it is not a feasible solution.

Another solution is to increase the gain so the pole will travel all the way to the RHP zero and cancel it out. However, this is not feasible either, because this will in practice only be possible with infinite gain. In addition to this, if the gain would decrease, for example due to the reaction wheels saturating, the pole would be moved from the zero towards origin and no longer even be close to canceling out with the zero.

Instead of trying to stabilize the system by traditional means, we will instead try to remove the cause of the RHP zero by compensating for the term that introduces the problem.

### 5.2.5 Pre-compensation using disturbance attenuation

To find the cause of the RHP zero we will look back at the state matrix  $\mathbf{A}$  in equation (5.29) and with the values inserted in (5.36). Here it can be seen that the RHP zero most likely emerges due to the last three columns, which are the columns associated with the cross product term  $\boldsymbol{\omega}_s \times \mathbf{h}_{rw}$ . By removing this term from the system, the resulting transfer matrix should no longer contain the RHP zero. This can be accomplished by introducing a new loop in the block diagram as shown in figure 5.7.

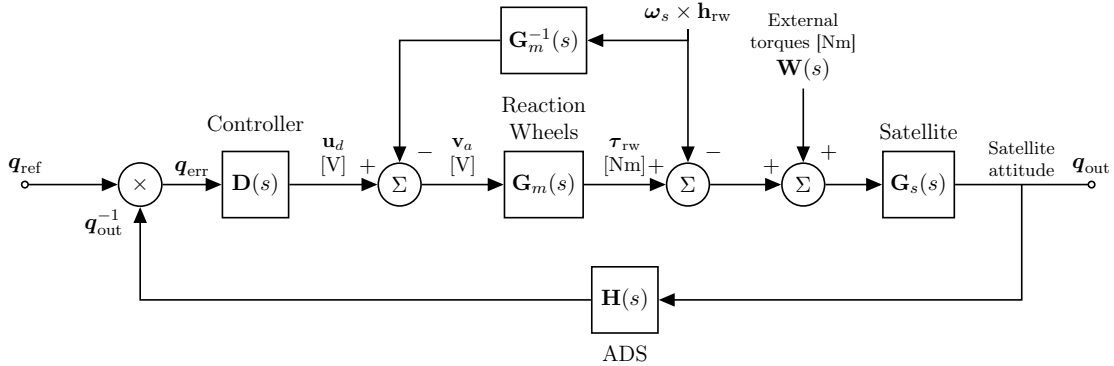


**Figure 5.7:** Block diagram for the attitude controller with pre-compensation.

As seen in the figure, the aforementioned cross product is added to the input torque to the satellite in a way similar to the environmental torques. Because this term only contains the angular velocity of the satellite  $\boldsymbol{\omega}_s$  and the angular momentum of the reaction wheels  $\mathbf{h}_{rw}$ , which are both easy to measure and calculate, the term can be subtracted from the input voltage to the motors. The block containing the inverse of  $\mathbf{G}_m(s)$  ensures that the cross product can be compensated by the dynamics of the DC motors. The transfer matrix  $\mathbf{G}_m^{-1}(s)$  is thus a  $3 \times 3$  diagonal matrix with the diagonal entries given by:

$$G_m^{-1}(s) = 5.16 \cdot 10^3 \cdot \frac{0.4753s + 1}{s} \quad (5.48)$$

As seen from the control diagram, the armature voltage is now given by:

$$\mathbf{v}_a = \mathbf{u}_D - \mathbf{G}_m^{-1}(s) \cdot (\boldsymbol{\omega}_s \times \mathbf{h}_{rw}) \quad (5.49)$$

This means the reaction wheel torque can be written as follows:

$$\begin{aligned} \tau_{rw} &= \mathbf{G}_m(s) \cdot \mathbf{v}_a \\ &= \mathbf{G}_m(s) \cdot \left( \mathbf{u}_D - \mathbf{G}_m^{-1}(s) \cdot (\boldsymbol{\omega}_s \times \mathbf{h}_{rw}) \right) \\ &= \mathbf{G}_m(s) \cdot \mathbf{u}_D - \boldsymbol{\omega}_s \times \mathbf{h}_{rw} \end{aligned} \quad (5.50)$$

In the summation point right of  $\mathbf{G}_m(s)$ , the cross product term in equation (5.50) will cancel out with the cross product term entering the summation point from above. With this pre-compensation controller implemented, the dynamic model for the satellite can be simplified to no longer contain this cross product term. A new transfer matrix can then

be constructed in the same manner as before, but this time the last three columns in the state matrix  $\mathbf{A}$  will be all 0. The resulting transfer matrix is found to be:

$$\mathbf{G}_{\text{tot}}(s) = \begin{bmatrix} \frac{0.12}{s^2+2.1s} & 0 & \frac{3 \cdot 10^{-5}}{s^3+2.1s^2} \\ 0 & \frac{0.0926}{s^2+2.1s} & 0 \\ 0 & 0 & \frac{0.0926}{s^2+2.1s} \end{bmatrix} \quad (5.51)$$

When compared to the old transfer matrix in equation (5.41) it is evident that the new one is simpler. Most importantly the RHP zero from the  $z$ -axis transfer function is gone, which was the purpose of this pre-compensation. Additionally, it can be noticed that the transfer function for the second and third axis is the same, due to their equal inertia. It can also be seen that the lower-left off-diagonal entry has disappeared, meaning that the only coupling between different axes now is from input 3 to output 1. It is therefore even less problematic than before to divide the system into three SISO systems with a 1-1, 2-2 and 3-3 input-output relationship. The next step is now to design a separate controller for each of the three SISO systems corresponding to each axis.

### 5.2.6 Controller requirements

In nadir mode, the satellite is rotating about the  $y$ -axis with a constant angular velocity equal to one rotation per orbit, that is  $\omega_{\text{nad}} = -0.0011 \text{ rad/s}$ . The reference attitude input in this case is therefore a line with a slope equal to  $\omega_{\text{nad}}$ .

In the requirements it was found that the required precision is  $\pm 1.24^\circ$ . The controller is therefore required to have a steady state error on the aforementioned ramp input of less than  $1.24^\circ$ .

When the satellite is changing from nadir mode to point tracking mode, this is equivalent to a step on the reference with magnitude  $90^\circ - 20.78^\circ = 69.22^\circ$  in the  $y$ -axis. As described in the requirements in section 3.1, the settling time of this step response has to be less than 100 seconds. There are also strict requirements to the precision for this step. It is required to have an overshoot of less than  $15.25^\circ$  during this step, which is equal to 22%.

In addition, the satellite has to keep the required pointing precision when affected by disturbance torques. As was found in section 2.3, the worst case disturbance is  $113.5 \cdot 10^{-9} \text{ Nm}$ . A simple worst case scenario to model is when the disturbance is constant with this amplitude. The controller is therefore required to keep a steady state error of less than  $1.24^\circ$ , when a disturbance step with amplitude  $113.5 \cdot 10^{-9} \text{ Nm}$  is applied, combined with the steady state error of a ramp input.

Finally, as the sample rate is given as 10 Hz, the closed loop bandwidth should be no more than 5 Hz, i.e. half the sampling speed. However, to ensure good performance of the controller, the sampling rate should preferable be between 20 to 40 times the closed loop bandwidth [15]. This means the bandwidth in this case should be no more than 0.5 Hz.

The controller will mainly be designed with nadir mode in mind. Depending on the performance of the controller in point tracking mode, it will be discussed whether or not a separate controller for point tracking mode needs to be designed or if the nadir controller is sufficient.

The controller requirements are summarized in table 5.1.

Parameter	Value	Unit
<i>W.r.t. reference step input</i>		
Settling time	< 100	seconds
Overshoot	< 22	%
Closed loop bandwidth	< 0.5	Hz
<i>Steady state error</i>		
W.r.t. reference ramp input	< 1.24	°
W.r.t. disturbance step input	< 1.24	°

**Table 5.1:** Requirements for the controller.

### 5.2.7 Controller for the $y$ - and $z$ -axis

The transfer function for the satellite dynamics is the same in the  $y$ - and  $z$ -axis, and because the requirements are identical for both axes, the same controller will be used in both axes as well.

One of the main requirements for the controller is to have a low steady state error when a constant disturbance is applied. In the following analysis, the controller will be a proportional controller with gain  $K_p$  to determine whether a more complex controller is needed. For the closed loop system with respect to the reference, the feedback path is unity. In this case, it can be seen by the number of integrators in the open loop, that the system is type 1, which means the system will have no steady state error on a step input and a constant steady state error on a ramp input. However, with respect to the disturbance, it is not seen as easily. Instead the steady state error can be calculated as follows. According to the control diagram, the error  $E(s)$  can be described as the following, where  $R(s)$  is the reference and  $W(s)$  is the disturbance:

$$E(s) = \frac{R(s)}{1 + D(s) \cdot G_m(s) \cdot G_s(s)} - \frac{W(s) \cdot G_s(s)}{1 + D(s) \cdot G_m(s) \cdot G_s(s)} \quad (5.52)$$

Inserting numbers the equation becomes:

$$E(s) = R(s) \cdot \frac{0.4752s^2 + s}{0.4752s^2 + s + 0.04405 \cdot D(s)} - W(s) \frac{108.0s + 227.3}{0.4752s^3 + s^2 + 0.04405s \cdot D(s)} \quad (5.53)$$

The steady state error can be found by using the Final Value Theorem, which is given in equation (5.54), which is valid as long as all poles of  $Y(s)$  are in the left half of the  $s$ -plane [15].

$$\lim_{t \rightarrow \infty} y(t) = \lim_{s \rightarrow 0} sY(s) \quad (5.54)$$

As we are only interested in calculating the steady state error with respect to the disturbance, the reference will be set to  $R(s) = 0$ . Usage of the final value theorem and giving a unit step input on the disturbance, that is  $W(s) = \frac{1}{s}$ , will then result in the following:

$$e_{ss,W} = \lim_{s \rightarrow 0} sE(s) \Big|_{W(s)=\frac{1}{s}} = \infty \quad (5.55)$$

This means that a step input on the disturbance will result in an unbounded steady state error which is not desirable. It can be seen from the function that if the controller was to contain an integrator, the steady state error would instead be a constant. Therefore a PI controller with transfer function  $D(s) = K_p + \frac{K_i}{s} = \frac{s + \frac{K_i}{K_p}}{s}$  will be considered next. In this case the steady state error becomes:

$$e_{ss,W} = \frac{227.3}{0.04405 \cdot K_i} = \frac{5154.75}{K_i} \quad (5.56)$$

This means that when a constant disturbance is applied, the steady state error will be a constant depending on  $K_i$ . In addition to this, the system with respect to the reference will now be a type 2 system, which means the steady state error will be 0 on both a step and a ramp input, and a constant on a parabola input.

Because of this, the controller to be designed will be a PI controller. The first thing to consider is the placement of the zero. In general, a zero added by the controller will add overshoot to the step response. The closer to origin the zero is placed, the better the damping and the less the step response will overshoot. However, as seen from equation (5.56), the closer the zero is to origin (meaning a smaller  $K_i$ ), the bigger the steady state error will be.

Based on the requirements to the steady state error with a constant disturbance of  $113.5 \cdot 10^{-9}$  and equation (5.56), a maximum value for  $K_i$  can be calculated. In quaternion units,  $1.24^\circ = 0.02$  rad is equivalent to 0.01, using the small angle approximation saying that  $q_1 \approx \frac{1}{2}\theta$  [2]. The minimum value for  $K_i$  can therefore be found by solving the following equation:

$$113.5 \cdot 10^{-9} \cdot \frac{5154.75}{K_i} = 0.01 \quad (5.57)$$

This results in  $K_i \geq 0.059$ . A suitable zero placement is -0.05, considering that the zero is determined by  $z = -\frac{K_i}{K_p}$ . Next is to decide on a gain  $K_p$ . To see how the gain affects the closed loop poles with the chosen zero, we will look at the root locus, which can be seen in figure 5.8.

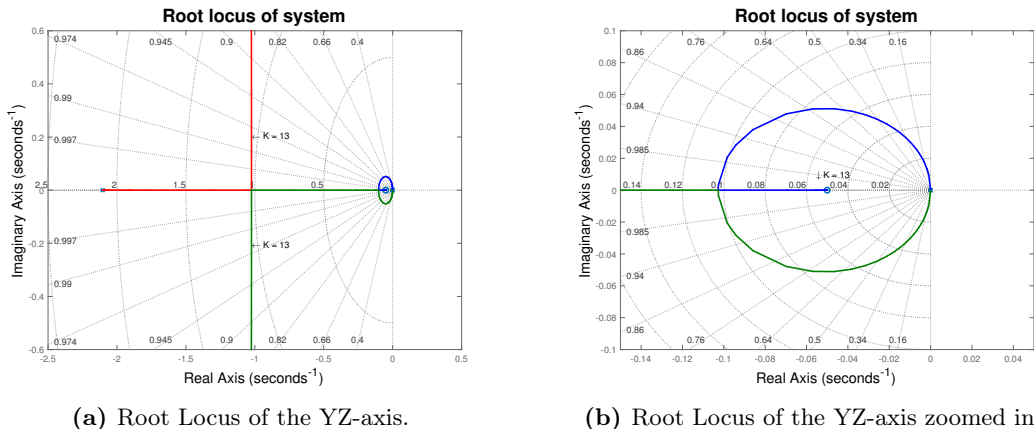


**Figure 5.8:** Root locus for the  $D_{yz}(s)$  controller.

Looking at the root locus it can be seen that the system will not have any poles in the RHP no matter the gain (as long as it does not change sign) and will therefore be stable. Which is important, because when the reaction wheels reach saturation, the actuation of the wheels decreases, equivalent to a lower gain in Laplace domain.

To prevent oscillatory behavior and overshoot, the damping factor should be close to 1, which is the case when the closed loop poles are placed close to or on the real axis. When the gain is increased, two of the poles will travel upwards/downwards away from the real axis, which means the overshoot and oscillatory behavior will increase. With a gain of  $K_p = 13$  we get the poles indicated by the small arrows in figure 5.8. The step response for this gain is shown in figure 5.9 with respect to the reference and in figure 5.10 with respect to the disturbance.

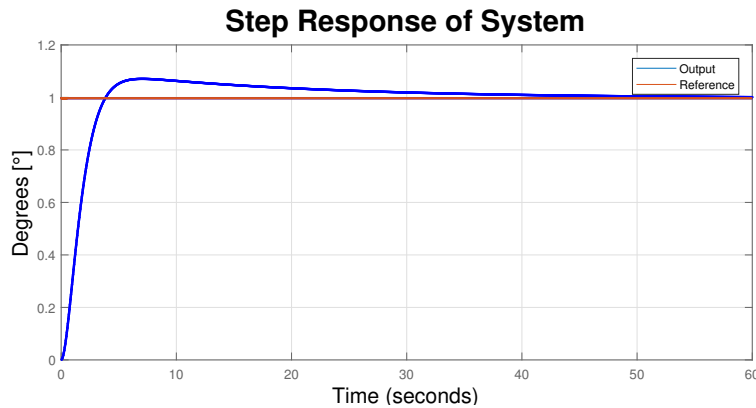


**Figure 5.9:** Response for a step input on the reference with magnitude  $1^\circ$ .

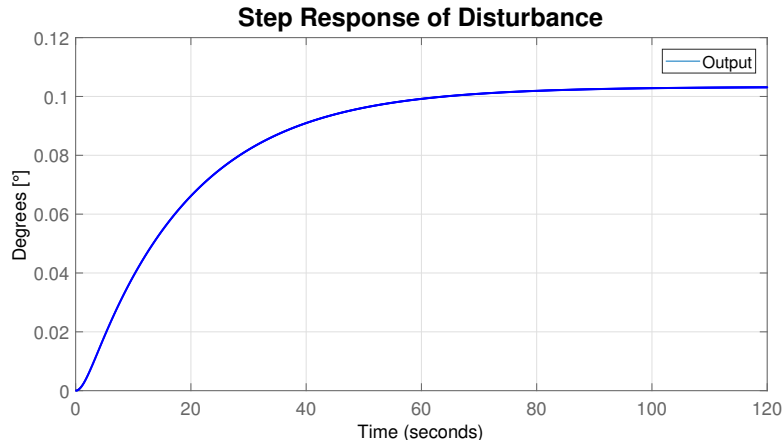


**Figure 5.10:** Response for a step input on the disturbance with magnitude  $113.5 \cdot 10^{-9}$  Nm.

As seen from these step responses, the system is relatively fast to react to changes on the reference with a rise time of 2.47 seconds. The settling time is a bit slow, however. The overshoot is 7.4%, which is acceptable. When looking at how it reacts to a step on the disturbance, it can be seen that the steady state error is constant at around  $0.1^\circ$ , which is lower than required. All in all, the response is acceptable. In figure 5.11 the response for a ramp input on the reference is shown.

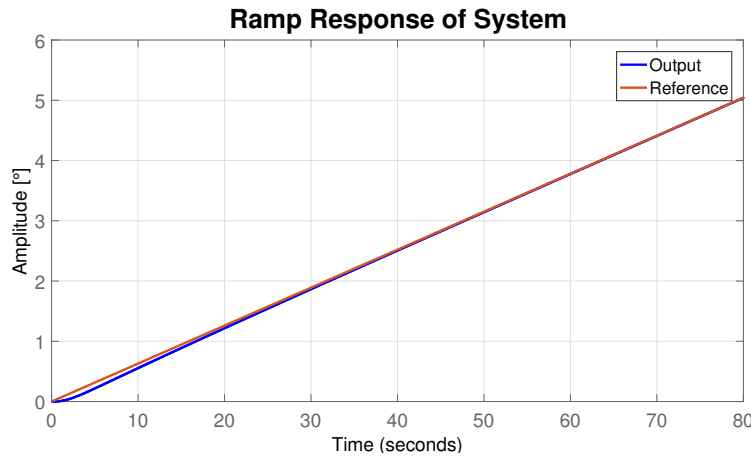
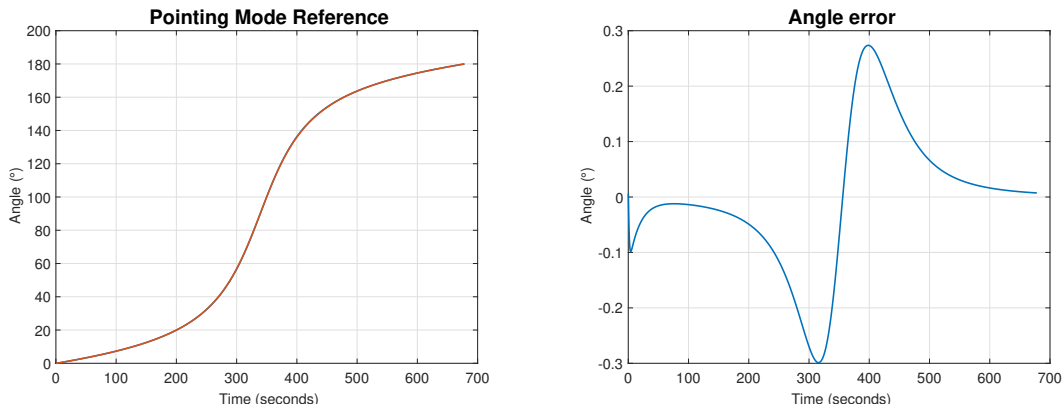


**Figure 5.11:** Response for a ramp input on the disturbance with slope 0.0011 rad/s.

As seen from the ramp response, the system is able to follow the ramp without any steady state error. As mentioned in the discussion of steady state errors earlier, this is a Type 2 system, which means the steady state error will be 0 on a ramp input. Furthermore the system can be examined, when it is given the reference used for point tracking mode as in figure 5.12.



(a) System response of point tracking mode input reference. (b) System error of point tracking mode input reference.

**Figure 5.12:** System response to the point tracking trajectory reference.

As it can be seen, the system response is close to the given input of the pointing mode reference. With the biggest difference in angle being  $0.3^\circ$  well within the required  $1.24^\circ$ , which makes the initial nadir controller adequate for pointing mode control as well.

To see how the frequency response is we will look at the bode plot of the open loop system. This is shown in figure 5.13.

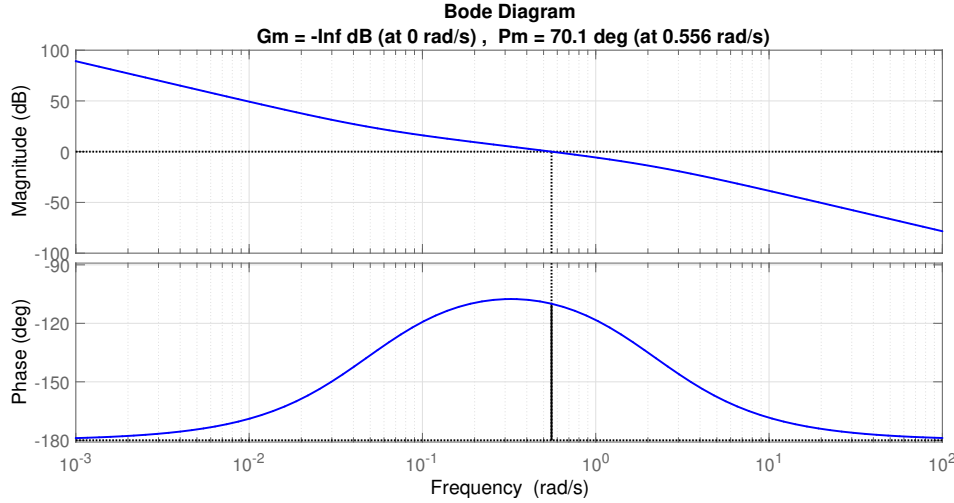


**Figure 5.13:** Bode plot of the open loop system.

From the bode plot it can be seen that the phase margin is  $70^\circ$ , which means the system is in no danger of becoming unstable. The gain margin, however, is minus infinity, because the phase starts at  $-180^\circ$ , but because of the zero pulling the phase up towards  $-90^\circ$  afterwards, the phase will in practice never be  $-180^\circ$ . Therefore the system is stable. The essential parameters and values of the step and ramp responses are listed table 5.2.

Parameter	Value	Unit
<i>W.r.t reference</i>		
Rise time	2.47	seconds
Settling time	31.7	seconds
Overshoot	7.4	%
Steady state error	0	°
<i>W.r.t disturbance</i>		
Steady state error	0.103	°

**Table 5.2:** Values of YZ-axis with controller

So in summary, the controller given by

$$D_y(s) = D_z(s) = 13 \cdot \frac{s + 0.05}{s} = 13 + \frac{0.65}{s} \quad (5.58)$$

gives an acceptable response.

The controller is designed, with mainly disturbance rejection and overshoot in mind. A faster correction of the disturbance results in more overshoot, which also threatens the required precision. The step response of the system, as well as a step response of the disturbance, of the y-axis controller can be seen in figure 5.9 and 5.10.

### 5.2.8 Controller for the $x$ -axis

For the  $x$ -axis the transfer function is almost identical, the difference being the gain. Small adjustments of the gain of the controller for the  $y$ - and  $z$ -axis yields similar results for the

*x*-axis. The chosen controller is as follows:

$$D_x(s) = 12.5 \cdot \frac{s + 0.05}{s} \quad (5.59)$$

This results in the values seen in table 5.3, having values for the controller which is similar to the *y*- and *z*-axis.

Parameter	Value	Unit
<i>W.r.t reference</i>		
Rise time	1.98	seconds
Settling time	27.1	seconds
Overshoot	6.99	%
Steady state error	0	°
<i>W.r.t disturbance</i>		
Steady state error	0.107	°

**Table 5.3:** Values of *x*-axis with controller

### 5.2.9 Limitations of the controller

The controller is designed under the assumption, that the input voltage to the motors has no limit, but in practice this is not the case. The testbed provides up to 3.3 V to the motor, which means the gain of the controller will be limited as well. The biggest input to the motors is when the satellite is changing from nadir to point tracking mode. In this case, the error will momentarily be around 70°, which in quaternion units corresponds to  $\sin \frac{70^\circ}{2} = 0.57$ . The output of the controller with gain  $K_p = 13$  will then be  $0.57 \cdot 13 = 7.46$  V. As this voltage cannot be provided to the motors, the motors will instead only get 3.3 V, which corresponds to a gain of  $K_p = \frac{3.3}{0.57} = 5.75$ . This means the closed loop pole placement will not be as expected, and this can be investigated through the root locus of the system, which is shown in figure 5.8.

The step response for a gain of  $K_p = 5.75$  is shown in figure 5.14.

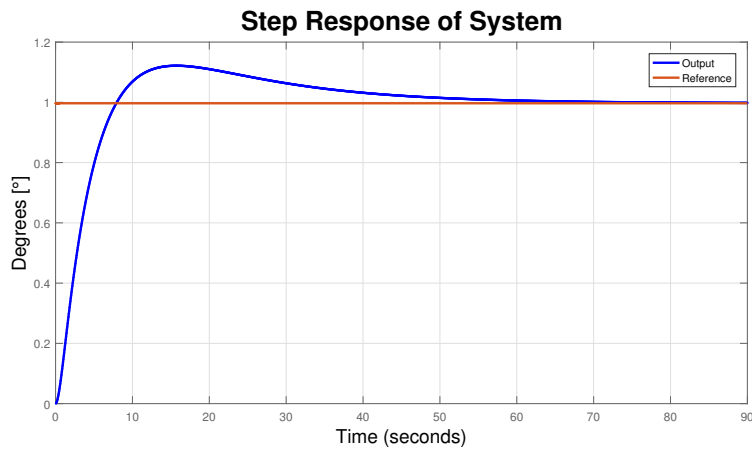


**Figure 5.14:** Response for a step input on the reference with a gain of  $K_p = 5.75$ .

In this case, the system response gets slower and the overshoot increases. Overall the response is still acceptable, as it still fulfills all the requirements.

### 5.2.10 Discretization and effect of sampling

When the controller is implemented in practice, the controller will be time discrete with a sampling rate of 10 Hz. This will have an effect on the controller performance, because all considerations so far have been with basis in a continuous time controller.

The closed loop bandwidth is  $\omega_{BW} = 0.054$  Hz, which fulfills the requirement of being a factor of 20 below the sample rate. Therefore the sample rate is not expected to have a big impact on the controller performance.

A good approximation for discretization of the system is the zero-order hold (ZOH), which approximates the system by assuming that the sampled value is kept constant for the duration of the sample period. This is the case for the testbed, which is why the ZOH is chosen as the discretization method.

The continuous controller  $D(s)$  can be converted to the time discrete controller  $D(z)$  with basis in the ZOH method by use of the following equation [15]:

$$D(z) = \left(1 - z^{-1}\right) \mathcal{Z} \left( \mathcal{L}^{-1} \left( \frac{D(s)}{s} \right) \Big|_{t=kT} \right) \quad (5.60)$$

where  $\mathcal{Z}$  is the Z-transform and  $\mathcal{L}^{-1}$  is the inverse Laplace transform. The result of the inverse Laplace transform is evaluated at  $t = kT$ , where  $T$  is the sampling period and  $k$  is the sample index.

Using equation (5.60) to convert the continuous controllers  $D_x(s)$  and  $D_{yz}(s)$  to time discrete equivalents will result in the following controllers:

$$D_x(z) = \frac{12.5 - 12.44z^{-1}}{1 - z^{-1}} \quad (5.61a)$$

$$D_{yz}(z) = \frac{13 - 12.94z^{-1}}{1 - z^{-1}} \quad (5.61b)$$

To verify that the controller works as intended when sampling is taken into account, we will look at a step response for the discrete controller compared to the continuous controller. For the  $yz$ -axis controller, this is shown in figure 5.15.

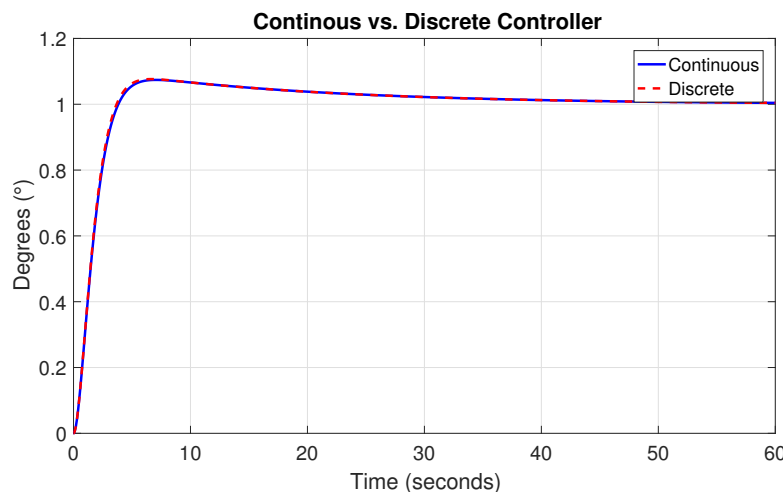


**Figure 5.15:** Step response of the continuous controller compared to the discrete controller.

As seen from the step responses, the discrete controller gives almost the exact same output as the continuous controller. This means the controller works as intended when sampling at 10 Hz.

### 5.2.11 Summary

Based on linear small signal approximations, controllers for each axis have been designed to comply with the given requirements. These controllers should be able to suppress disturbances and maintain nadir pointing during orbits based on the calculated model. It was investigated whether or not the controller was able to follow the point tracking trajectory as well, where it showed that it was able to follow it and still comply with the requirements. The model does not take into account limitations of possible gains due to saturation in the motors, which leads to a lower gain in practice when a too large step on a reference input is made. The initial controller is still implemented, yet with the knowledge of the limitations regarding large step changes.

Before the controllers can be tested on the testbed, the controllers will be implemented within the simulation environment to ensure that the controllers work as intended on the nonlinear satellite model as well.



# 6 | Simulation of Attitude Control System

In this chapter, the controller designed in chapter 5 will be implemented in a simulation environment. The simulation is done in **Matlab/Simulink** utilizing libraries made by former AAU students during the development of earlier AAUSAT satellites. The simulation enables the possibility to test the controllers on the nonlinear dynamic model with disturbances included along with other elements such as reaction wheel bias and saturation.

First some details related to the simulation implementation will be described, and afterwards the simulation results will be discussed.

## 6.1 Implementation in Simulink

The simulation environment is based on the AAUSAT library. The following building blocks are used:

- AAUSAT block which contains:
  - Spacecraft dynamics
  - Disturbances - based on models of magnetic field, orbit, albedo and eclipse
  - Ephemeris
- TLE
- SPG4

### 6.1.1 Nonlinear spacecraft dynamics

The AAUSAT block is used for simulating the dynamics of the satellite as it orbits the Earth, along with environmental disturbances as described in section 2.3. The spacecraft dynamics in the simulation are implemented using the nonlinear dynamic and kinematic equations of motion as described in chapter 4. The input to the block is thus the torque generated by the reaction wheels, and the output is the satellite attitude and angular velocity.

Another input to this block is a TLE data set. TLE stands for Two-Line Element set and contains information of a specific satellite, including information about the orbital movement such as inclination and eccentricity - in short, information necessary to give an approximative position and to estimate the future trajectory of the satellite. Based on TLE data for a specific satellite and SGP4, it is possible to obtain a position vector and a velocity vector for the given satellite at any given time.

The SPG4 stands for Simplified General Perturbations, an open source algorithm which tries to predict a satellite's position as it orbits Earth. The prediction is made by knowing the conditions of the satellite, such as launch date, orbit distance from the Earth, etc. It uses models of the perturbations found in space, but have reduced precision when the satellite is more than 6000 km above the surface of the Earth. The models include perturbations such as Earth's shape, atmospheric drag and gravitational differences along Earth. It also includes models for gravitational effects from the sun and the moon and solar radiation pressure on the satellite. The simulation is based on TLE data from AAUSAT4 from May 13 2018 from CelesTrak [1].

### 6.1.2 Input reference quaternion

The reference for nadir pointing is equivalent to the ORF and is computed by usage of TLE and SGP4. As described above, the SGP4 gives a position vector  $\mathbf{r}$  and velocity vector  $\mathbf{v}$  given in the ECI reference frame, where the position vector is the vector from the center of Earth to the center of the satellite. The axes corresponding to the ORF are thus easily found, respectively, by the negative of the normalized position vector, the normalized velocity vector, and the cross product between the two:

$${}^o\mathbf{z} = -\frac{\mathbf{r}}{|\mathbf{r}|} \quad (6.1a)$$

$${}^o\mathbf{x} = \frac{\mathbf{v}}{|\mathbf{v}|} \quad (6.1b)$$

$${}^o\mathbf{y} = {}^o\mathbf{z} \times {}^o\mathbf{x} \quad (6.1c)$$

The direction cosine matrix describing the ORF is thus given by:

$${}_i^o\mathbf{A} = \begin{bmatrix} {}^o\mathbf{x} & {}^o\mathbf{y} & {}^o\mathbf{z} \end{bmatrix} \quad (6.2)$$

The direction cosine matrix is then translated to a quaternion as described by equation (A.10) in appendix A, which is the reference quaternion used for nadir pointing.

To simulate the point tracking maneuver, the reference is set to change from nadir mode to point tracking mode after a set amount of time, and to change back to nadir again after the maneuver is done.

The reference input for the pointing mode maneuver was found in figure 3.2 on page 18. This trajectory is implemented as an angle rotation about the  $y$ -axis of the ORF, which is converted to a quaternion. This quaternion, called  ${}^t\mathbf{q}$ , symbolizes the rotation required to track the point relative to nadir pointing. This quaternion is then used to rotate the ORF quaternion to obtain the quaternion describing the tracking attitude, as described by the following relation:

$${}^t_i\mathbf{q} = {}^t\mathbf{q} \ {}^o_i\mathbf{q} \quad (6.3)$$

The change from nadir mode to point tracking mode is equivalent to a step of  $69.22^\circ$ . This step is implemented in a manner similar to the above.

Finally, when the reference and feedback signal are combined to produce an error signal to the controller, it is necessary to multiply the inverse of the feedback signal with the

reference, as described in the beginning of section 5.2. Because of the nature of quaternions, the computed reference quaternion will at some point change sign, which in turn makes the error signal change sign. To prevent this from influencing the control, the error quaternion is multiplied with the sign of  $q_{err4}$  to make sure the error quaternion does not suddenly change sign.

### 6.1.3 Motor dynamics and torque distribution

The motor dynamics are implemented as described in section 4.5.1 using continuous transfer functions from input voltage to angular velocity, and from angular velocity to torque.

The three controllers are implemented as the discrete transfer functions found in section 5.2.10. Because the controllers are designed without consideration of the tetrahedron configuration, the three control outputs has to be converted to match the four input voltages to the four motors. The relationship between the three control torques and the four reaction wheel torques was in section 4.5.2 found to be given by the following, where  $\mathbf{P}$  is the  $3 \times 4$  distribution matrix:

$$\begin{bmatrix} \tau_x \\ \tau_y \\ \tau_z \end{bmatrix} = \mathbf{P} \begin{bmatrix} \tau_1 \\ \tau_2 \\ \tau_3 \\ \tau_4 \end{bmatrix} \quad (6.4)$$

We need to find  $\boldsymbol{\tau}_{1234}$  given that we know  $\boldsymbol{\tau}_{xyz}$ . Because  $\mathbf{P}$  is not square, it cannot be inverted to solve this system, and this system therefore has infinite solutions. One solution is given by the following:

$$\begin{bmatrix} \tau_1 \\ \tau_2 \\ \tau_3 \\ \tau_4 \end{bmatrix} = \mathbf{P}^+ \begin{bmatrix} \tau_x \\ \tau_y \\ \tau_z \end{bmatrix} \quad (6.5)$$

where  $\mathbf{P}^+$  is the pseudoinverse of  $\mathbf{P}$  given by:

$$\mathbf{P}^+ = \mathbf{P}^T (\mathbf{P} \mathbf{P}^T)^{-1} = \begin{bmatrix} 0.70 & 0 & -0.25 \\ -0.35 & 0.61 & -0.25 \\ -0.35 & -0.61 & -0.25 \\ 0 & 0 & 0.75 \end{bmatrix} \quad (6.6)$$

This solution has the desirable property that it minimizes the norm of the vector  $\boldsymbol{\tau}_{1234}$ , which is why it is chosen [16].

The chosen bias point for the reaction wheels is implemented by adding a bias voltage of 0.618 V, as found in section 4.5.3, to each of the four motors, which results in the bias velocity of 320 rad/s or around 3000 RPM. In addition to this, the input voltage to the motors is limited to 0-3.3 V, which is the maximum voltage output of the testbed.

The full simulation environment can be seen in figure 6.1.

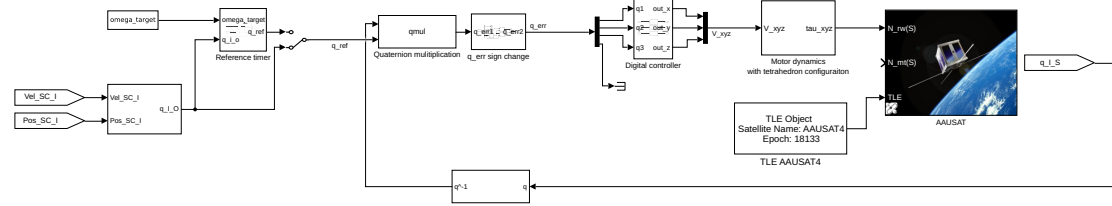


Figure 6.1: Implementation of the simulation environment.

## 6.2 Simulation Results

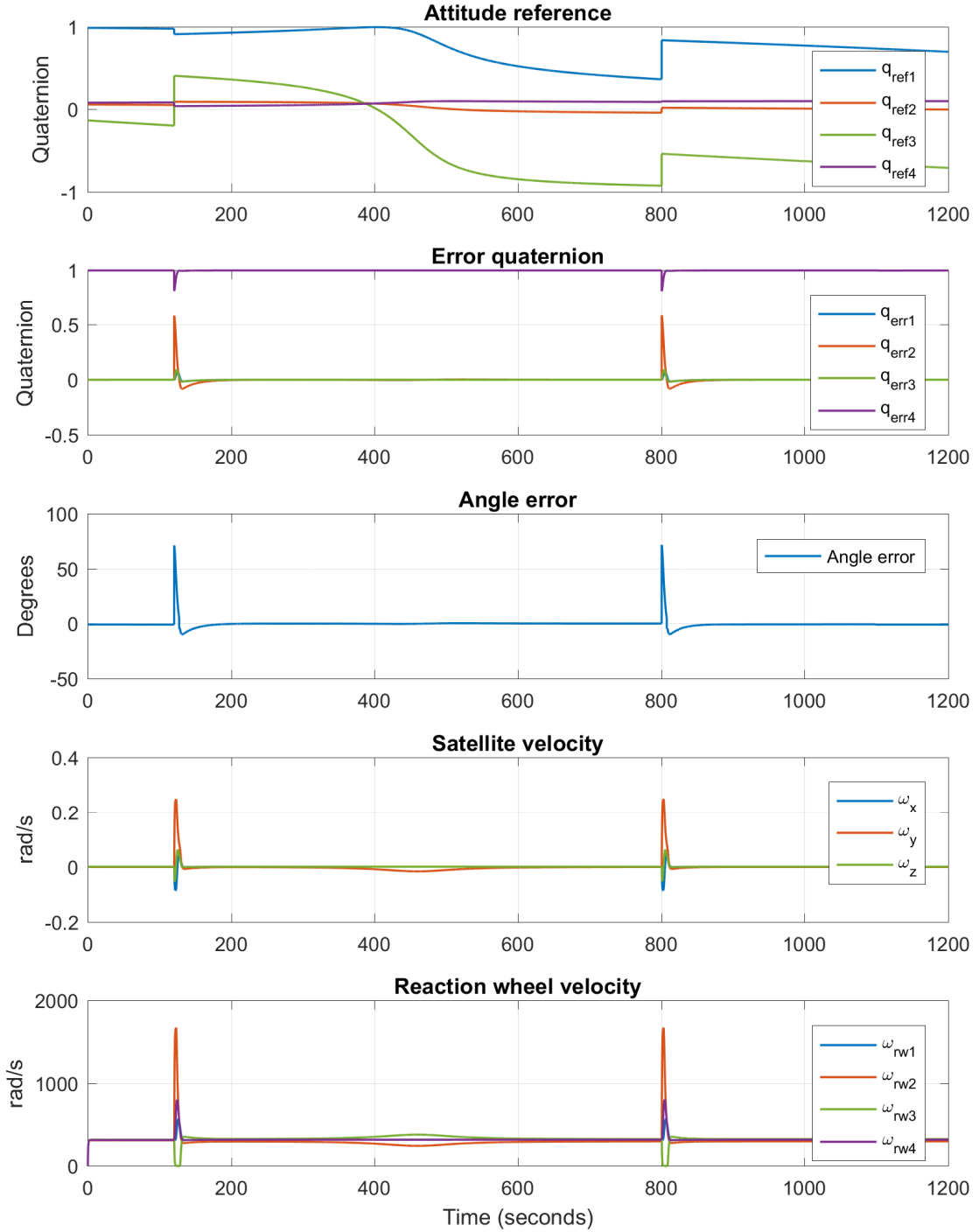
The simulation model is evaluated for 1200 seconds - equal to about 1/5 of an orbit. During this simulation the satellite is requested to perform nadir pointing for the first 120 seconds, then change to point tracking mode by doing a  $69.22^\circ$  step, then follow the point tracking trajectory, and then finally change back to nadir pointing 678 seconds later. The remaining time, the satellite is asked to perform nadir pointing. The simulation results are shown in figure 6.2.

Figure 6.2 contains from top to bottom:

- The attitude of the satellite described by a quaternion  ${}_I^S\mathbf{q}$ .
- The error quaternion  $q_{err}$ , describing the error between the reference and the present attitude.
- The error described as the angle  $\Phi$  about the rotation axis. This is calculated as  $\Phi = 2 \cdot \arccos(q_{err4})$ .
- The angular velocity of the satellite in all three axes, given in radians per second.
- Lastly, the velocity of the four reaction wheels in the tetrahedron configuration, given in radians per second.

From the figure the change of reference is clear in that the satellite changes to point tracking mode at time  $t = 120$  and back to nadir at  $t = 798$ . Both the satellite and the reaction wheels gain a burst in speed when the reference is changed from nadir to point tracking mode. A closer look at this change is found in figure 6.3. Here the change to point tracking mode around the time  $t = 120$  is evaluated. Looking at the error quaternion and the satellite velocity, it can be seen that even though the step on the reference only happens in the  $y$ -axis, the satellite starts rotating about the two other axes as well. This is due to the Coriolis effect stemming from the cross product term  $\boldsymbol{\omega}_s \times (\mathbf{I}_s \boldsymbol{\omega}_s + \mathbf{h}_{rw})$  in the dynamic model. Because the angular velocity of the satellite  $\boldsymbol{\omega}_s$  increases, the Coriolis effect will be larger, which in turn will make the satellite rotate more about the other axes.

Looking at the velocity of the reaction wheels, it can be seen that when one reaction wheel reaches saturation it will have an effect on the rest of the reaction wheels. As RW3 saturates, it will cause an imbalance in the tetrahedron configuration, because RW2 and RW3 only cancels out in the other axes when they give the same torque. This can be seen by looking at the distribution matrix  $\mathbf{P}$  for the tetrahedron configuration in equation (4.48) on page 32. When RW3 saturates, RW1 and RW4 begins to change velocity to cancel out RW2's contribution to the  $x$ - and  $z$ -axis, respectively.



**Figure 6.2:** Simulated model evaluated for 1200 seconds.

Looking at the angle error, it can be seen that the error is larger than  $\pm 1.24^\circ$  up until around 175 seconds, which means that the system fulfills the precision requirement after this time. In general, the system seems to follow the step quite well in a fashion similar to the one designed for in chapter 5.

In figure 6.4 the simulation is zoomed in around the point tracking maneuver. First of all,

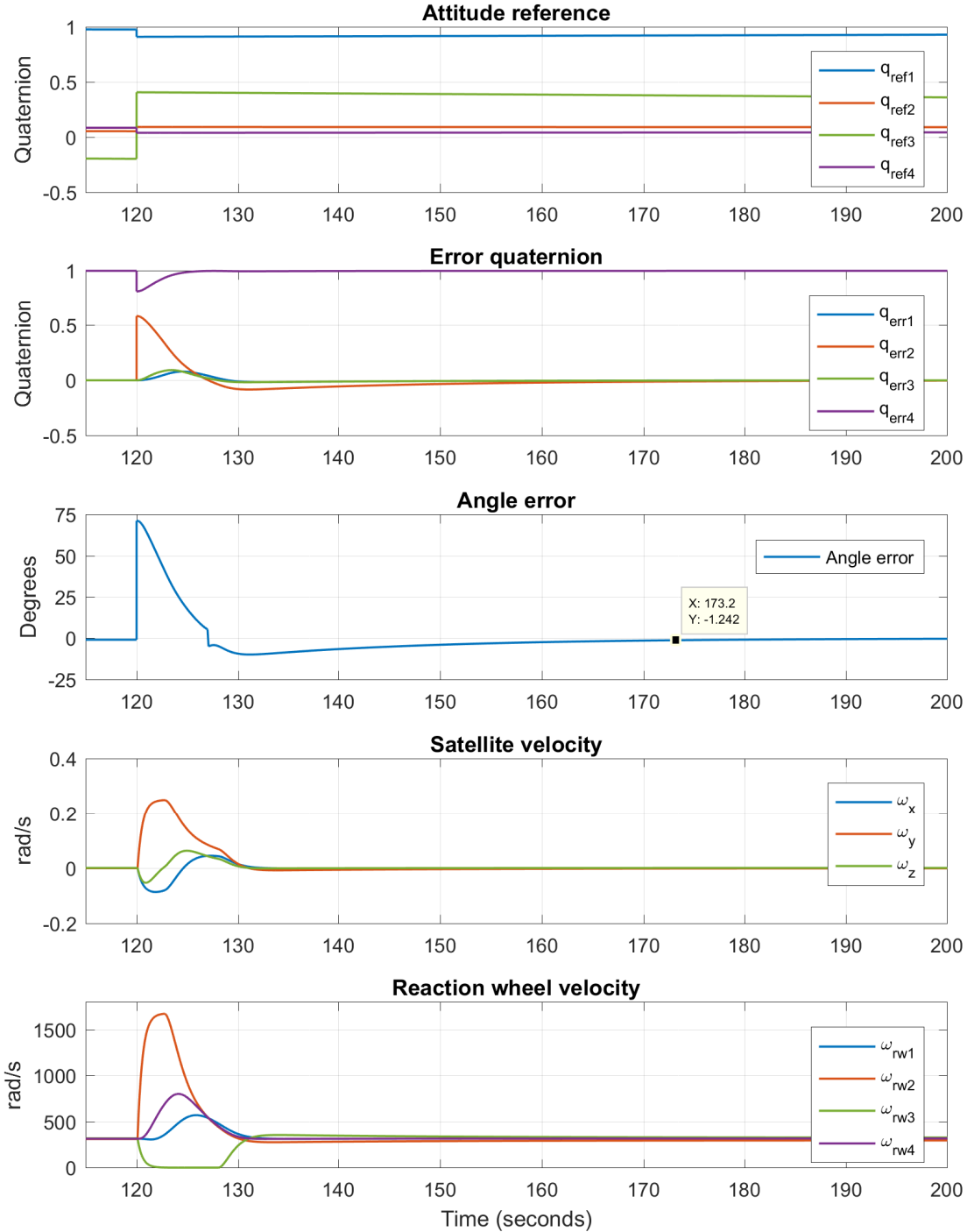


**Figure 6.3:** Simulation with zoom on step from nadir to point tracking mode.

when looking at the angle error it can be seen that the error around time  $t = 200$  seconds is well below the required  $\pm 1.241^\circ$ . Then as the reference starts to change, the error starts to increase again. It can be seen that the error seems to follow a similar curve to the one observed in figure 5.12 on page 55 during the controller design on the linear model. This error is never larger than  $\pm 0.3^\circ$ , which is well within the precision requirement.

Looking at the satellite velocity, it can be seen that the velocity of the satellite follows

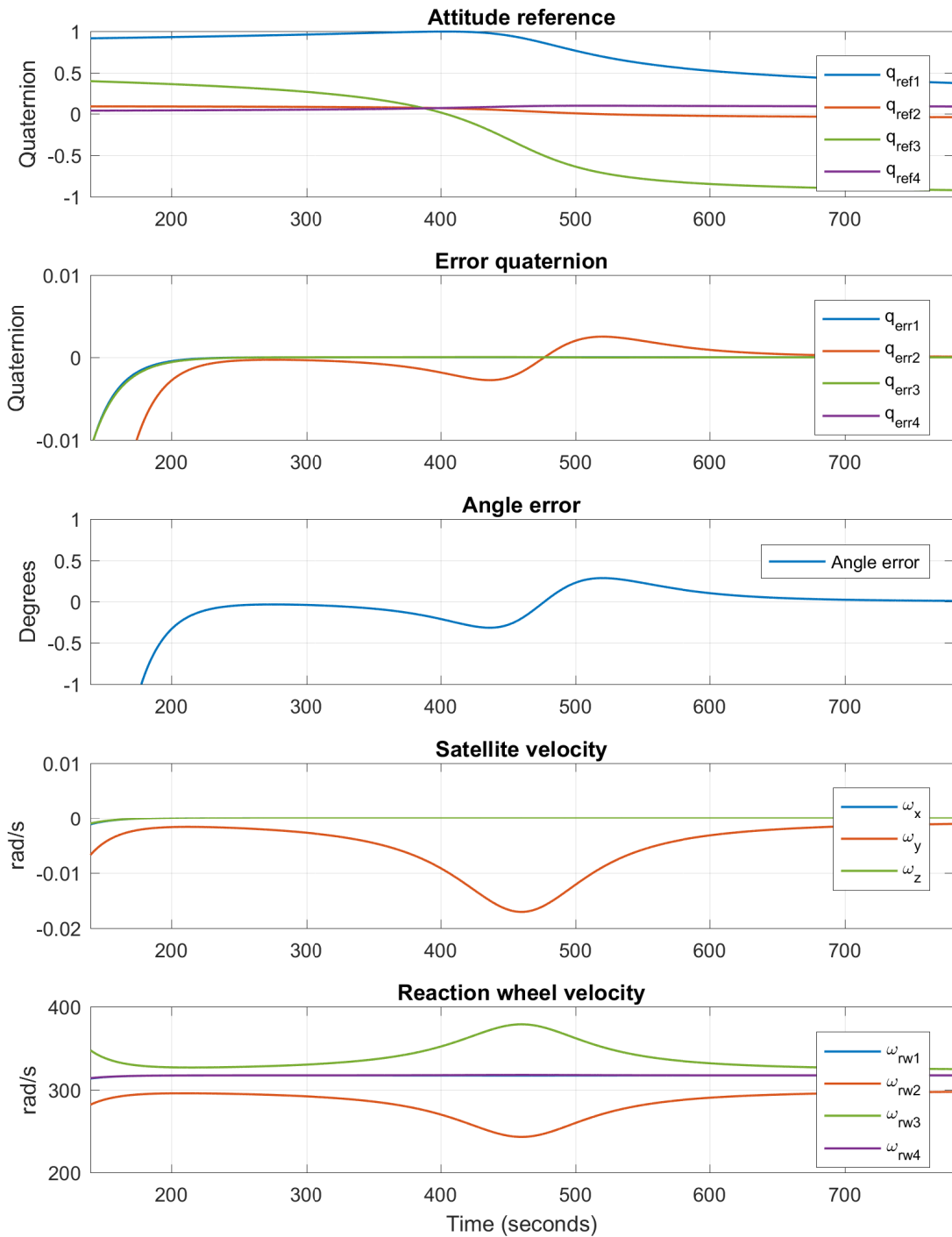


**Figure 6.4:** Simulation with zoom on tracking trajectory.

a curve similar to the one in figure 3.2 from the reaction wheel bias section on page 18, and that the velocity reaches around 0.0169 rad/s as required. In a similar manner, the velocity of the reaction wheels seems to match the curve shown in figure 4.6 on page 34. In summary, the system seems to perform as expected and fulfills the requirements.

### 6.2.1 Impact of environmental disturbance torque

In order to see how the environmental disturbances affect the system performance, the simulated environmental disturbance torque is shown in figure 6.5.

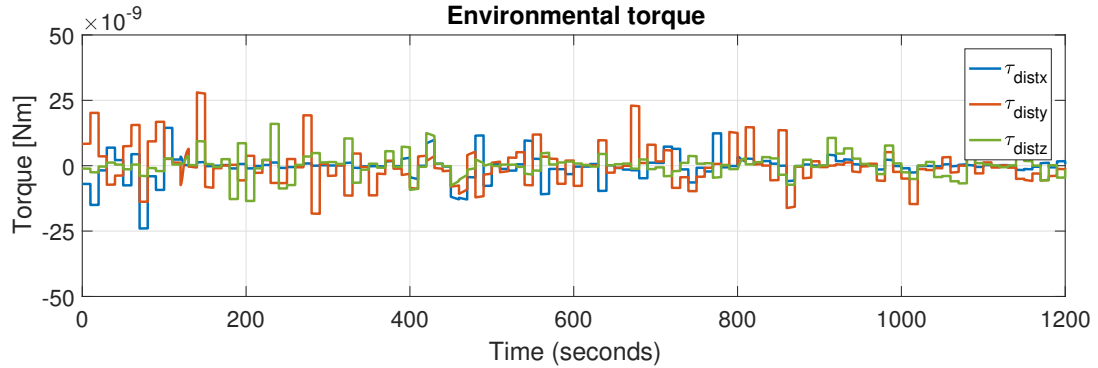


**Figure 6.5:** Simulation of environmental disturbance torque.

The figure shows that the disturbances are well below the estimated worst case value of  $113.5 \cdot 10^{-9}$  Nm, determined in section 2.3. This means that the controller does not have any difficulties suppressing these during the required maneuvers. The disturbance only has a visible impact on the simulations results when looking closely at the error, where it can be seen that the angle error is around  $0.05^\circ$ . However, when subject to a constant disturbance over longer periods of time, the reaction wheels will eventually reach saturation, if momentum dumping is not happening, due to the reaction wheels having to provide a constant torque to compensate for the disturbance. To investigate this further, the model is simulated for 7 days of nadir pointing. The results of this simulation are shown in figure 6.6.

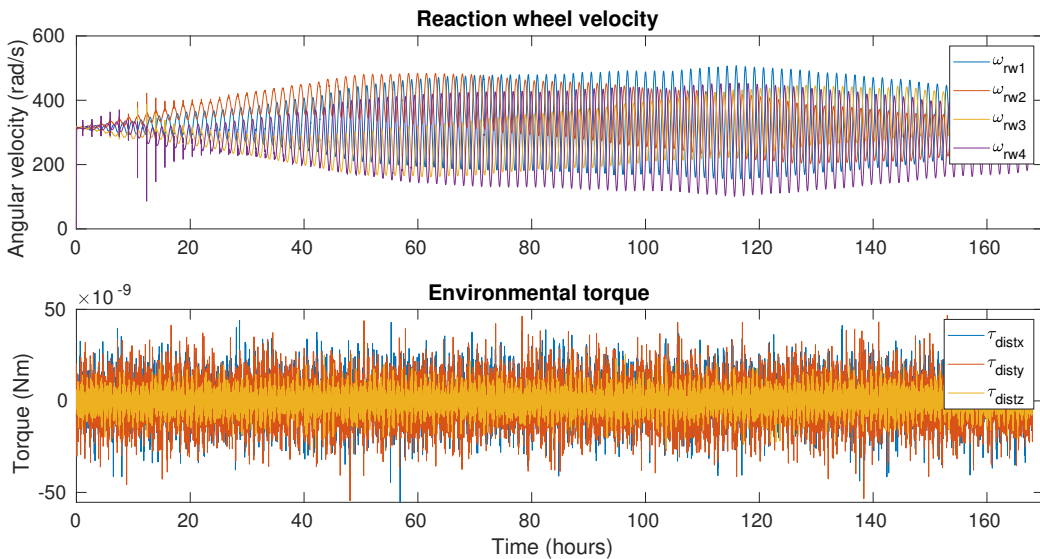


**Figure 6.6:** Simulation of 7 days of nadir pointing with disturbances.

It can be seen that the reaction wheels actually do not saturate during this time. This

might be due to the fact that some of the disturbances are periodic due to the satellite moving in a periodic orbit, and that way they might cancel themselves out. It might also be due to how the disturbance torques are calculated in the simulation environment. Because they are taken from the AAUSAT library, it has not been investigated closely in this project how they are actually calculated. This might be relevant to investigate further, especially if magnetorquers and momentum dumping were to be implemented, but this is considered out of scope of this project.

### 6.2.2 Impact of the pre-compensation in the controller

One of the premises for being able to stabilize the system was the pre-compensation introduced in the diagram in figure 5.7 on page 50. To investigate how much effect this pre-compensation really has on the system, the magnitude of the Coriolis effect stemming from the cross product term  $\omega_s \times \mathbf{h}_{rw}$  is plotted in figure 6.7. In the same figure the output of the  $\mathbf{G}_m^{-1}(s)$  block is plotted as well to see how big the voltage contribution is from this term.

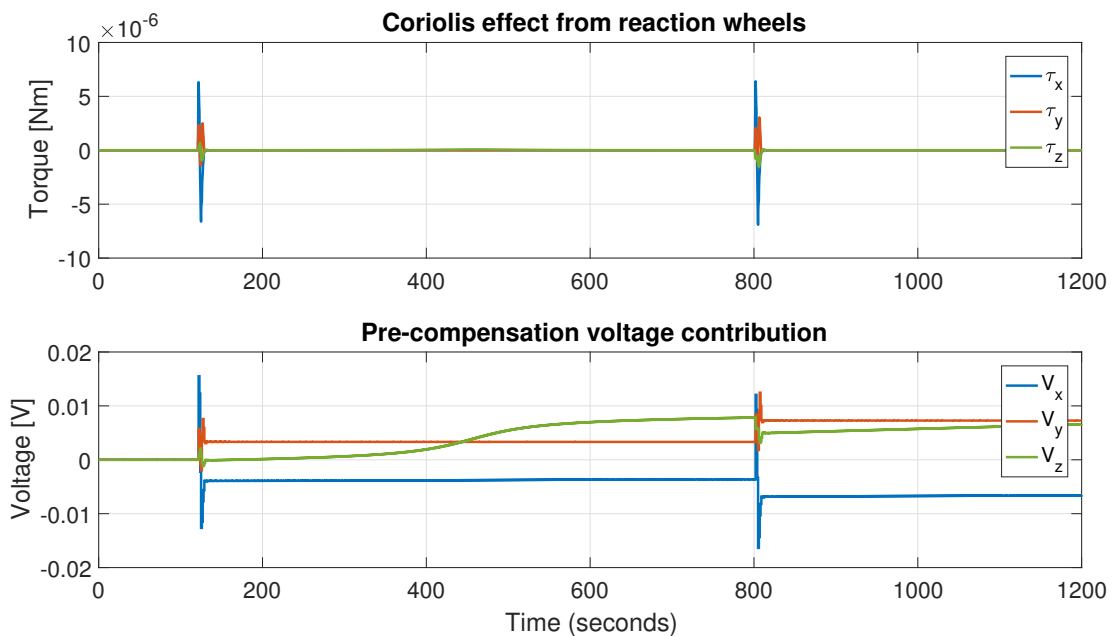


**Figure 6.7:** Simulation of coriolis effect from the reaction wheels and the pre-compensation voltage contribution.

As seen from the figure, the torque due to Coriolis effect from the reaction wheels is up to around 5  $\mu$ Nm during the 70° step, and in the order of 10 nNm during nadir pointing and the point tracking maneuver. This means this effect is almost negligible, and as seen from the voltage contribution, the voltage resulting from the pre-compensation is only up to around 0.01 V. This pre-compensation does only have a very low influence on the response of the system during these maneuvers and might as well be completely absent. It might, however, have a greater effect during other maneuvers, but as this is not the case for this project, this pre-compensation will not be taken into consideration further on.

### 6.2.3 Summary

The simulation environment is implemented in **Simulink** using sections of the AAUSAT library. Both nadir and point tracking mode references are given to the satellite, as well as a step change between the two modes. The simulations show that the system is able to follow all reference inputs satisfactorily, and that the nonlinear model and the linear model seem to give similar results. The simulations also show that the disturbance torques were less than the calculated worst case values and that they did not have a big impact on the response. Similarly, the Coriolis effect from the reaction wheels and the pre-compensation controller did not have a big impact on the system either.

# 7 | Acceptance Test

In this chapter the testbed introduced in section 2.4 will be used to test the controller designed in section 5, which was further implemented and simulated in section 6. Before discussing the test results, some of the features and limitations of the testbed will be discussed.

## 7.1 Implementation on the Testbed

In this section some of the details related to the implementation of the controller on the testbed will be discussed along with some of the limitations of the testbed.

### 7.1.1 Testbed description

As briefly mentioned in section 2.4, the ACS testbed consists of a satellite model in an acrylic ball, which is able to move freely due to an air bearing stand. Besides the air bearing stand, the testbed consists of three parts:

- An actuator board on the satellite model containing the actuators with relevant firmware
- A main board on the satellite model containing the sensors and an XBee wireless module with relevant firmware
- A PC containing an XBee wireless module and relevant software incorporating ROS and Matlab/Simulink

The main board is the master of the system and controls the sampling rate of 10 Hz. It sends a sample of sensor data to the PC using the XBee wireless module, which is then processed on the PC in Matlab/Simulink. The PC sends a control signal back to the main board, which is then sent from the main board to the actuator board. The PC then waits for another sample of measurements and does not perform any computations during this waiting time.

All firmware on the satellite model will be assumed to work correctly and only be treated as a black box. The same goes for the software running on the PC, except for the control algorithm which is written anew. The following data from the testbed is used:

- Satellite attitude described by a quaternion
- Angular velocity of the satellite
- Angular velocity of the reaction wheels

This data is determined using gyroscopes, accelerometers and magnetometers, and encoders for measuring the angular velocity of the reaction wheels. The attitude determination is done using these sensors in combination with an extended Kalman filter, making predictions of the future attitude, and then later compare the predictions with the measured attitude. Given that the testbed among others is using measured data of the magnetic field to determine the attitude, a problem arises since a satellite normally would use Earth's magnetic field, but at Earth's surface the magnetic field is very weak compared to other man made magnetic fields, such as the ones that come from the power grid. Furthermore, the Earth's magnetic field has an inconvenient angle in Aalborg, which makes it difficult to use for correct attitude determination. This means that the testbed benefits greatly from having a strong magnetic field produced by other means, which in this case is produced by a Helmholtz coil. This produces a magnetic field stronger than Earth's and others, and leads to a more accurate attitude determination [7].

Like the simulation described in chapter 6, the data processing is made in Matlab/Simulink. This includes calibration of the sensors, attitude determination and the control algorithm itself.

### 7.1.2 Testbed controller adjustment

The testbed satellite model is different compared to AAUSAT3, which the designed controller is based on. Because the testbed model is only containing equipment necessary for testing controllers using reaction wheels and possibly magnetorquers, the model weighs less than a complete CubeSat such as AAUSAT3, which results in a lower moment of inertia. The moment of inertia of the testbed satellite model is approximated by Thomsen and Nielsen in their thesis [7], which can be seen in the matrix below compared to the inertia used from equation (4.18). Additionally, in this estimation the CRF and the SRF are assumed to be aligned.

$$\mathbf{I}_{\text{AAUSAT3}} = \begin{bmatrix} 1.7 & 0 & 0 \\ 0 & 2.2 & 0 \\ 0 & 0 & 2.2 \end{bmatrix} \cdot 10^{-3} \text{ kg} \cdot \text{m}^2 \quad \mathbf{I}_{\text{testbed}} = \begin{bmatrix} 0.67 & 0 & 0 \\ 0 & 0.70 & 0 \\ 0 & 0 & 0.73 \end{bmatrix} \cdot 10^{-3} \text{ kg} \cdot \text{m}^2 \quad (7.1)$$

As it can be seen the inertia is approximately three times smaller. A smaller inertia means that the testbed model requires less torque to rotate it. The lesser inertia has to be taken into account, if a similar result is desired compared to the simulations in chapter 6. Another controller with proportional gain  $K_p = 5$  was tested, but because no big difference was evident between the results from the old controller and the new controller, the results from the new controller have been omitted from this chapter. Instead these results can be found in appendix B. Only the results from the original controller designed in chapter 5 will be addressed in this chapter, but with the knowledge that the moment of inertia is lower on the testbed than in the simulations.

### 7.1.3 Testbed disturbance torque

During the test session of the testbed, a considerable disturbance is noticed. The ball which contains the satellite model is accelerating without any actuation due to uneven

mass distribution. This is expected as it was concluded by Thomsen and Nielsen [7]. The satellite model is equipped with adjustable mass elements to make it possible to adjust the center of mass. This is however very difficult to get right by hand, which makes it impossible to make attitude control in three axes. As Thomsen and Nielsen concluded it is instead possible to stabilize the satellite in the  $z$ -axis by only using the lower half of the acrylic ball, which makes it possible to make attitude control in the  $z$ -axis.

In addition to the disturbance due to the mass distribution, another source of disturbance exist when the satellite model is stabilized in the  $z$ -axis. This other disturbance is most likely due to small variations in the airflow, which may result from both uneven airflow holes in the testbed and uneven surface of the acrylic ball. This disturbance results in a constant torque being applied to the ball, making it spin in a clockwise direction. The torque is estimated to have a magnitude of  $1\text{--}22 \mu\text{Nm}$ . This value is found from inspecting the reaction wheel torque when the satellite is having zero angular velocity. This is around 10-200 times the disturbance of  $113.5 \text{ nNm}$  estimated in section 2.3.

As a consequence of the clockwise torque applied to the testbed, the satellite will have to overcome a significantly higher disturbance than designed for. This means that rotating the satellite in a clockwise direction requires little actuation torque, but rotating counterclockwise requires immense actuation compared to the torque the reaction wheels are able to produce making it nearly impossible to rotate counterclockwise for more than a few seconds.

The satellite model is still tested, yet only instructed to rotate in clockwise directions in steps and ramp inputs, such that the momentum of the reaction wheels is used for stabilization or keeping the given reference. Another precaution made due to the disturbance is to change all motor biases from  $314.16 \text{ rad/s}$  determined in section 4.5.3, to half the supply voltage, which is  $1.65 \text{ V}$ , equal to around  $840 \text{ rad/s}$  or  $8021 \text{ RPM}$ .

## 7.2 Controller Tests on Testbed

The tests performed on the testbed are aimed at being as close as possible to the situations analyzed during the controller design and the simulation. This means that ideally the controller should be tested with a  $70^\circ$  step on the reference, nadir pointing equivalent to a ramp reference with slope  $-0.0011 \text{ rad/s}$ , and the point tracking trajectory reference. However, due to the limitations of the testbed, namely the large disturbance torque, it is not possible to test the controller in this exact way because the reaction wheels will reach saturation too fast. Instead the tests are scaled appropriately to match the testbed environment. The nadir and point tracking trajectories are both scaled up by multiplying the rotational speed with 20, and the step is decreased to  $35^\circ$ . The controller will therefore be tested with the following reference inputs:

- Step amplitude  $-35^\circ$
- Ramp with slope  $-0.022 \text{ rad/s}$
- The point tracking trajectory (scaled by a factor 20)

A test journal of the test can be found in appendix B. The following figures starts around the time of a new input. Prior to the 20 seconds of adjusting the reaction wheels to the

given bias.

### 7.2.1 Step response

The results of the test with a  $-35^\circ$  step input on the reference are shown in figure 7.1.

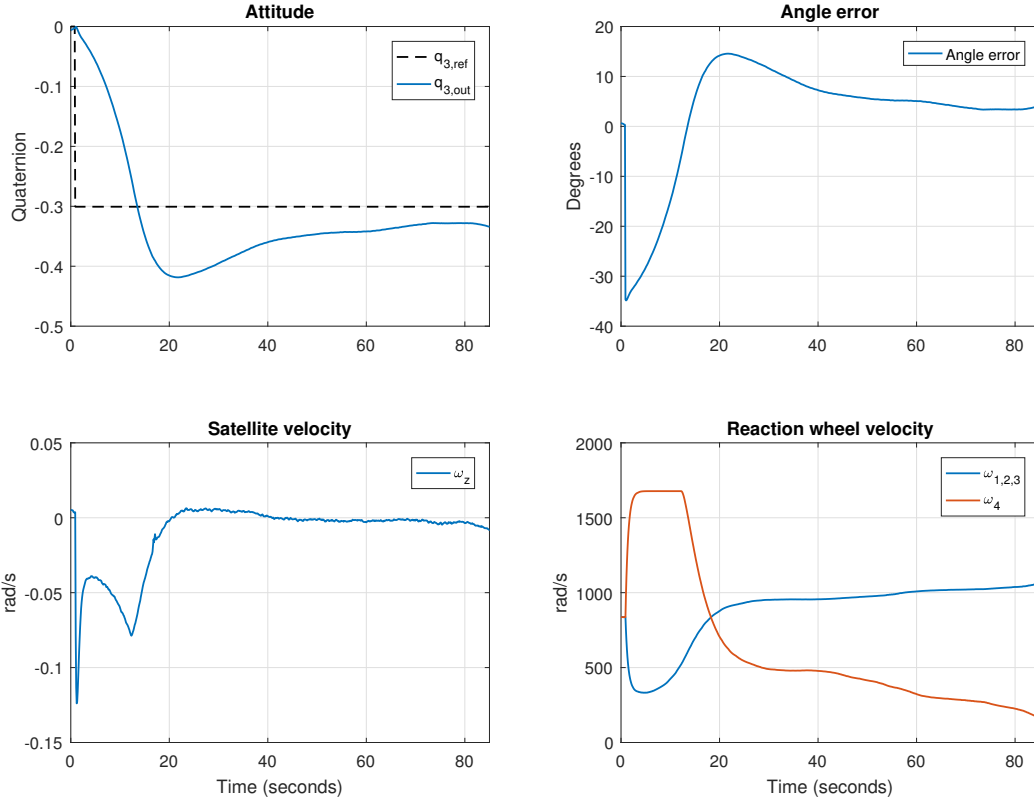


**Figure 7.1:** Step of  $-35^\circ$  about the  $z$ -axis.

From the step response it can be seen that the controller is able to follow the step with a rise time of approximately 8 seconds and with a small amount of overshoot. As was analyzed during the controller design in section 5.2.7, the system with a PI controller is type 0 with respect to the disturbance, which means the system will have a constant steady state error when subject to a constant disturbance. This is seen to be the case during the tests as well, and because the disturbance torque from the testbed is large, the steady state error is large as well. It is difficult to judge the settling time, because the reaction wheels reach saturation too fast, so it is hard to say how much of the error is due to the steady state error and how much is due to the system still settling in. It can be seen that the controller is able to keep the satellite steady for almost 90 seconds before the reaction wheels reach saturation.

The controller might be able to keep the satellite steady for a longer time if the bias point for the reaction wheels are different. Because the torque is distributed unevenly between the four reaction wheels in the tetrahedron configuration (reaction wheel number 1, 2 and 3 each contribute -33% and reaction wheel number 4 contribute 100%), reaction wheel 4

will reach saturation before the three others. By taking this into account when assigning the bias point, the reaction wheels will be able to drive longer before reaching saturation.

### 7.2.2 Nadir pointing

The results of the nadir pointing test (ramp reference input) are shown in figure 7.2.

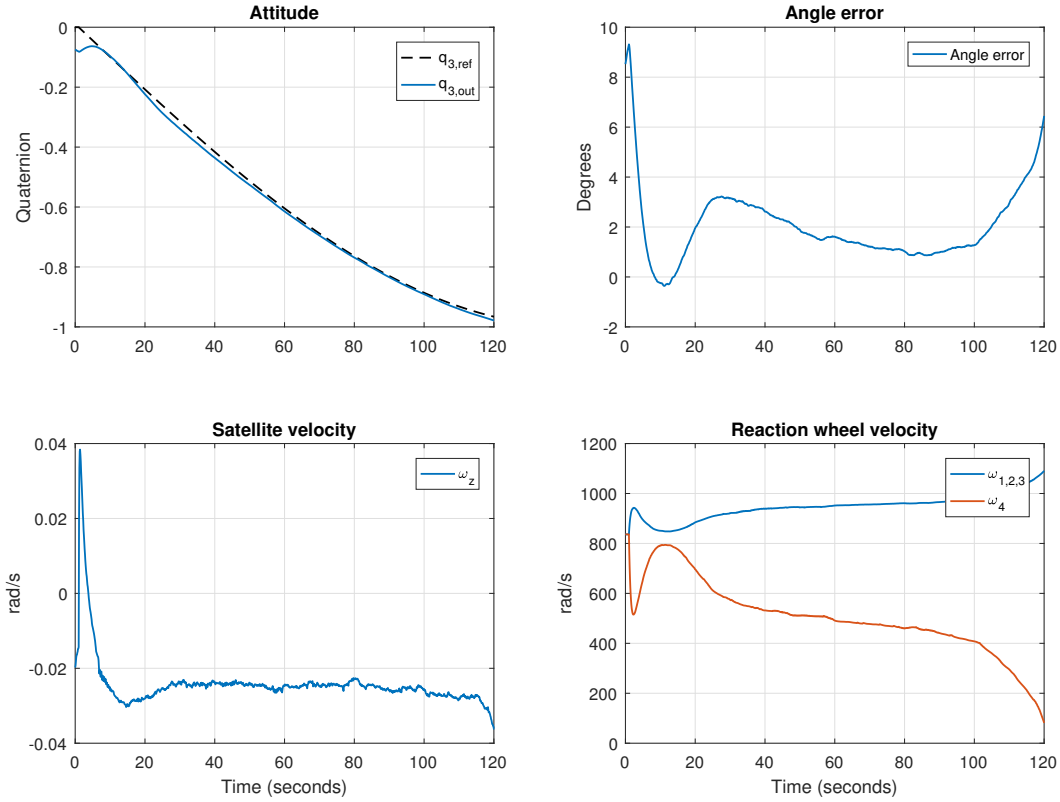


**Figure 7.2:** Ramp input with slope  $-0.022 \text{ rad/s}$  about the  $z$ -axis.

From the nadir pointing test it can be seen that the controller is able to follow the reference for approximately 100 seconds. Looking at the satellite velocity it can be seen that the satellite keeps a constant velocity close to the  $-0.022 \text{ rad/s}$  expected from the ramp input.

The system has an error larger than required. For a ramp reference input with no disturbance, the steady state error is zero, as described during the controller design in section 5.2.7, due to the system being type 2. As in the case for the step test, the steady state error is therefore due to the constant disturbance. The steady state error is therefore expected to be the same as in the step test. This does indeed seem to be the case, but it is hard to judge because the system may not have settled completely in the step test.

After about 120 seconds the reaction wheels reach saturation and the system is no longer able to follow the reference.

### 7.2.3 Point tracking

The results of the point tracking test are shown in figure 7.3.

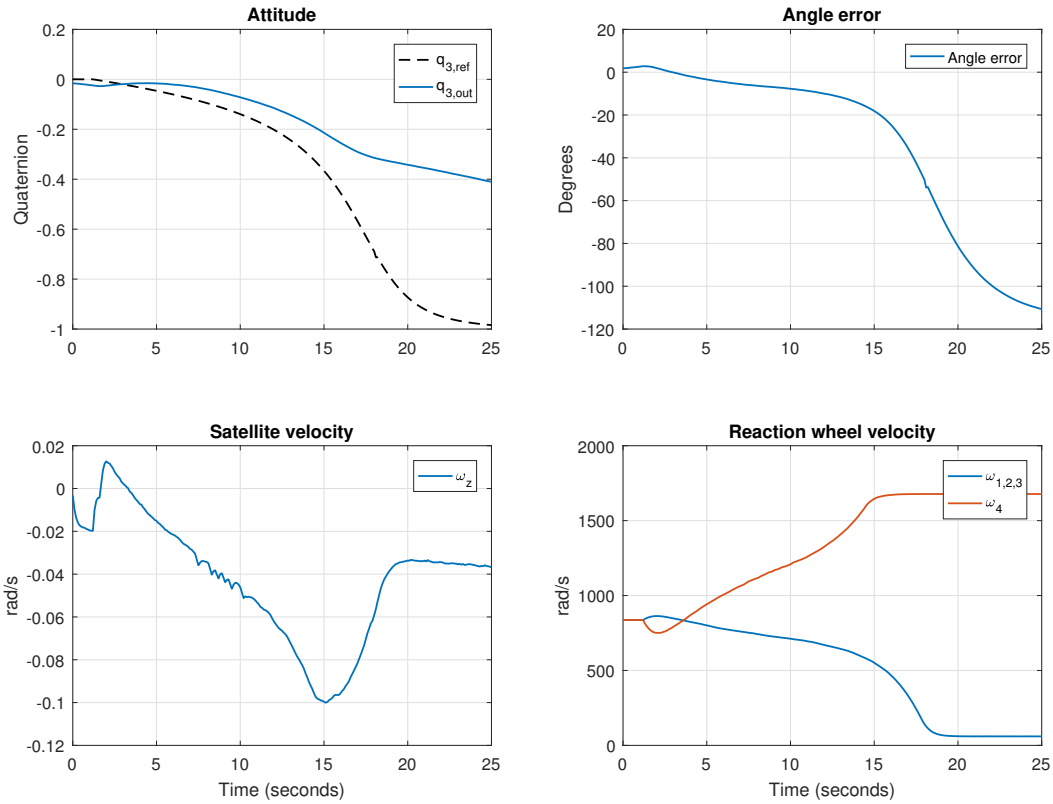


**Figure 7.3:** Point tracking trajectory (scaled by a factor 20) about the  $z$ -axis.

From the point tracking test it can be seen that the system is able to follow the reference to some degree. Based on the observations done during the controller design and the non-linear simulations, the system was expected to have an error during the point tracking maneuver. This is indeed the case, and just as in the other tests, the constant disturbance makes this error larger. When looking at the satellite velocity, it is evident that the velocity follows a similar curve as the one shown in figure 3.2 on page 18. However, the velocity peak is lower than the required peak during the maneuver, which is  $20 \cdot 0.0167 \text{ rad/s} = 0.332 \text{ rad/s}$ . This might be related to the error. It can also be seen that the reaction wheels reach saturation after just 14 seconds, which is very low. Because the trajectory is scaled by a factor 20, the maneuver will require more torque from the reaction wheels in general, so it might be possible that it might not be able to perform the maneuver even without the disturbances.

#### 7.2.4 Summary

None of the tests were able to prove that the controller fulfills the requirements because the disturbance torque proved to have too much of an impact on the results. Other options for testing the system is therefore considered, and it is decided to have the satellite suspended into the air using a fishing line, as an attempt to reduce the disturbance torque.

### 7.3 Tests Using a Suspended Satellite Model

The biggest benefit of using the air bearing testbed is that it, in theory, allows for movement in three dimensions, but due to the limitations mentioned earlier, it is in practice only possible to control the movement in one axis. Since the tests on the testbed did not show satisfying results because of the disturbance produced by the air bearing of the testbed, the satellite model of the testbed is instead suspended into the air using a fishing line, such that it hangs freely within the Helmholtz coil. This still allows for movement in one axis, and the expectation is that the fishing line suspending the satellite applies less disturbance than the testbed, and therefore yields better results. To minimize the disturbance originating from the torsion in the fishing line, the fishing line is fastened as high as possible above the ground, which is around 3.5 m in the laboratory.

Furthermore as the tests performed on the testbed did not indicate any big differences with regards to the new controller, it has been decided that only the original controller will be tested, as it is presumed that the new controller once again will not have a noticeable difference on the system. The implementation is otherwise the same as in the testbed, with the only difference being that the satellite is suspended without being in the testbed's air bearing, as can be seen in appendix B.2. The suspended system is given the following reference inputs:

- Step amplitude  $-35^\circ$
- Ramp with slope  $-0.022 \text{ rad/s}$
- The point tracking trajectory (not scaled)

The point tracking is in the suspended case not scaled, as it was quickly experienced that the suspended system allowed for lower angular velocities compared to the testbed. The suspended system gave similar poor results when the point tracking maneuver is scaled by a factor 20, as it can be seen in figure B.13, presumably because the increased angular velocity is too demanding for the system in general. As in the case for the air bearing tests, all test results for the fishing line suspended test can be found in appendix B.2.

### 7.3.1 Step response

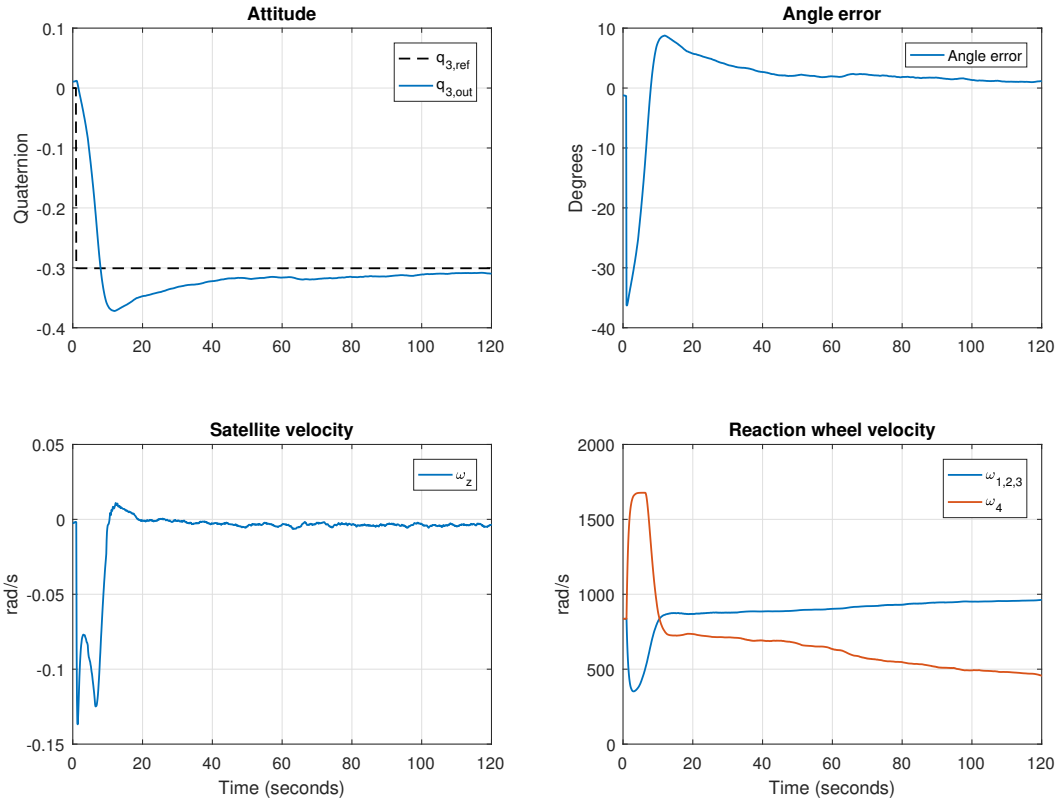


**Figure 7.4:** Step response of a  $-35^\circ$  reference change about the  $z$ -axis

Figure 7.4 shows a step response of  $-35^\circ$ , the same as for the air bearing test. It can be seen that it takes 103.2 seconds for the system to settle below the required  $1.241^\circ$ . This is a big improvement compared to the same test performed on the air bearing testbed, which never reaches the required precision. It is however 3.2 seconds too long to fulfill the requirements of 100 seconds.

Furthermore, it can be seen that the overshoot is lower. The error due to the overshoot is  $8.74^\circ$ , which for a  $35^\circ$  step is equal to 24.9% overshoot. This is a bit more than what is allowed by the requirements. Compared to the simulations, this increase might be both due to the lower moment of inertia and the fact that the wheels saturate during the first 10 seconds, which increases the overshoot as seen in section 5.2.9. Compared to the air bearing test, the reaction wheels are in saturation for a shorter period of time during the fishing line test.

Looking at the rise time of the system, it can be seen that it is slower in the test compared to the simulations. This is most likely due to the reaction wheels saturating earlier when adjusting to the step in the test than in the simulations.

It can also be seen that the system is stable for a longer span of time. As can be seen in appendix B.2, the system was able to hold the reference for 300 seconds before the reaction wheels saturated. Compared to the 90 seconds of the air bearing testbed, this is

an obvious improvement as well.

### 7.3.2 Nadir pointing

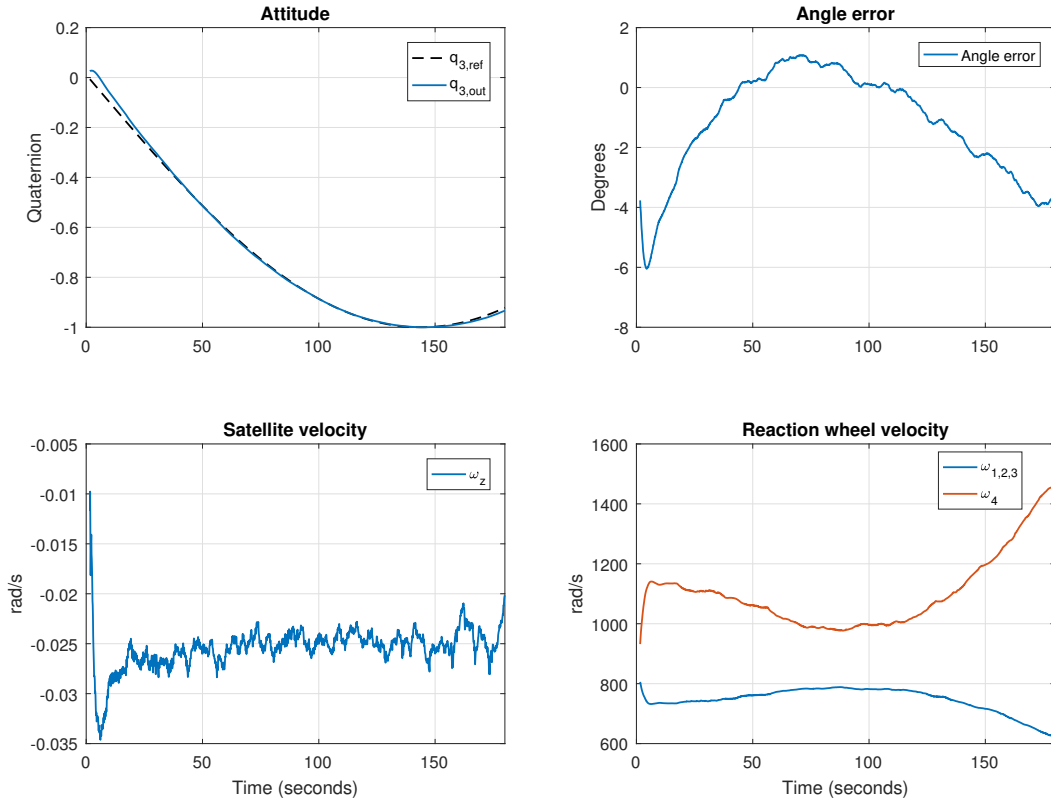


**Figure 7.5:** Ramp input with a slope of  $-0.022 \text{ rad/s}$  about the  $z$ -axis.

Figure 7.5 shows the response of a ramp input, equal to 20 times the velocity required for nadir pointing - the same velocity tested on the testbed. As was the case for the step test, the suspended system performed better than the air bearing test, with higher precision and a longer time span before the reaction wheels saturates.

The system seems to never truly reach a stable error, as the reaction wheels reaches saturation before this can happen, which happens around 180 seconds into the test. The system is however within the required precision for around 100 seconds from  $t = 30$  to  $t = 130$ . This test thus shows that the system is able to follow a nadir-like reference satisfactorily.

### 7.3.3 Point tracking

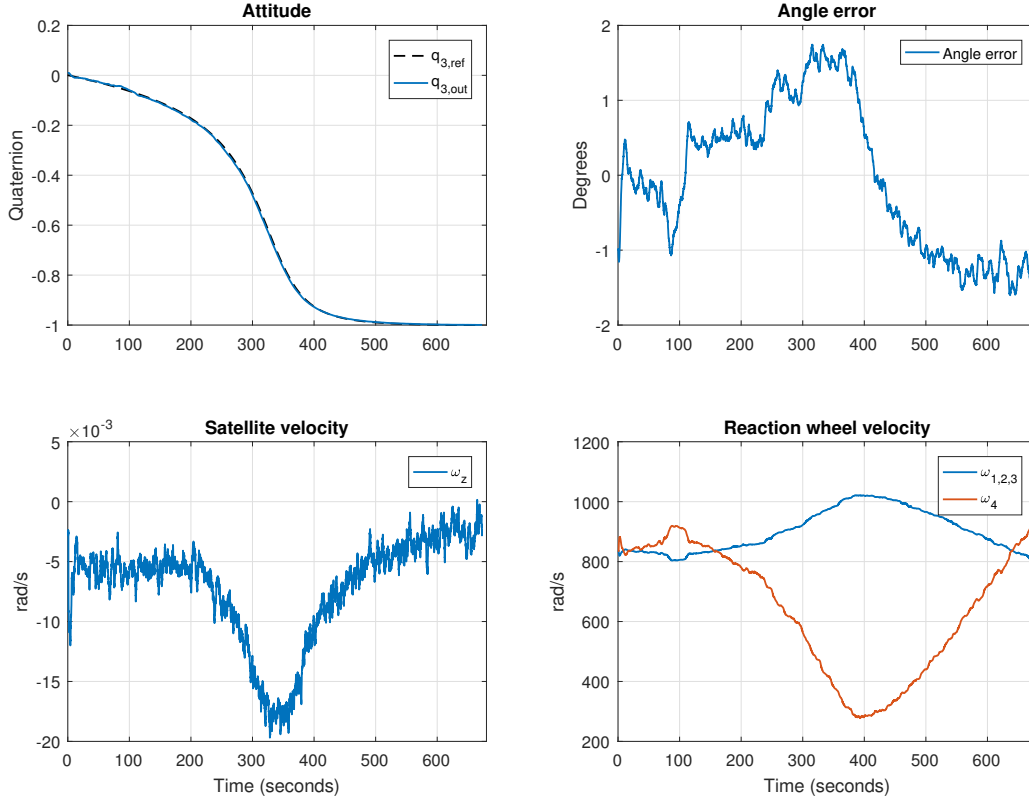


**Figure 7.6:** Point tracking trajectory (no scaling) about the  $z$ -axis.

In figure 7.6 the system is tested with respect to tracking a point. Compared to the air bearing testbed, the fishing line suspended system allowed for the right angular velocity to perform point tracking at the intended reference input. It can be seen that the system is able to perform the whole maneuver without the reaction wheels reaching saturation. The error during the maneuver is mostly within the requirement, but not during the entirety of the test. Compared to the simulation in figure 6.4, which had an error no larger than  $\pm 0.3^\circ$ , this test performed significantly worse. The inferior performance is assumed to be caused by the larger disturbances and the different moment of inertia.

Compared to the expected velocity curve of both the satellite velocity and reaction wheel velocity, the test seems to follow these curves well. Especially the satellite velocity can be seen to follow the curve well as it reaches about 0.0169 rad/s at the right time. The error follows a similar curve as the errors in the simulations as well noting that the error changes sign around 400 seconds (see simulations in figure 5.12 and figure 6.4), except for the magnitude of the error.

## 7.4 Summary

Both a new and the initial controller was tested on the testbed. The purpose of the new controller were to take into account the change of inertia. The new controller did not prove

unambiguous effects, compared to the initial controller. Most significantly about the test is the testbed's relative large disturbance which required precautions. Therefore it was not possible to give the testbed the same reference as the simulations, and it was only possible to test in one axis. Yet the test did prove the concept of the controller, as it was able to keep a steady reference, but with a large steady state error due to the disturbance.

It is clear that using the testbed for making comparisons between reality and simulations is difficult as the physical aspects of the testbed are too different compared to the simulations. It is however possible to prove a controller is capable of controlling a system for short periods.

As an attempt to achieve better results, the system was suspended into the air using a fishing line, which yielded better results in terms of the disturbance applied to the satellite. As a consequence the response of the system improved significantly, enough to be able to compare the test results with the simulations.

Referring to the test specifications in section 3.2, it can now be concluded whether or not the requirements are fulfilled. The results are summarized in table 7.1.

Requirement	Passed
T.1: Nadir pointing	(✓)
T.2: Point tracking	✗
T.3: Pointing precision	✗
T.4a: Step change settling time	✗
T.4b: Step change pointing precision	✗

**Table 7.1:** Technical requirements from section 3.1, passed ✓/not passed ✗.

T.1: The nadir pointing test proved that the system was able to follow the nadir reference with the required precision for most of the duration of the test. This test was not performed with the exact nadir angular velocity of 0.0011 rad/s, but instead with a scaled version. It is however assumed that if it is able to follow the scaled version, it should equally be able to follow the non-scaled version if not for the large disturbance.

T.2: The point tracking test proved that the system was able to follow the point tracking trajectory in a manner similar to the simulations. It was, however, not withing the required precision, most likely due to large disturbance torques. Therefore this requirement is not fulfilled.

T.3: The pointing precision requirement is not fulfilled because T.2 was not fulfilled.

T.4a/T.4b: The step test showed that the system was able to follow the step reference in a satisfactory manner with a response not unlike the simulations. The test result, however, showed that the system was significantly slower than the simulations, both in relation to rise time and settling time. The overshoot was too large as well. The reason for the system to perform worse in the tests is most likely due to the different moment of inertia and the disturbance torque making the reaction wheels reach saturation too fast initially when the step is happening.



# 8 | Closure

Through the project, an attitude control system for a CubeSat has been designed. A model of the satellite was developed using reaction wheels as actuators, and a linear controller was designed and implemented in both simulations and on a testbed made by former AAU students, and tested on these. In this section the conclusions drawn is summarized and ideas for future improvements are described.

## 8.1 Conclusion

With basis in the upcoming AAUSAT6, assumed to be carrying a camera payload, an attitude control system is needed. The aim of this project has been to answer the problem statement written in chapter 3 and repeated below:

*How can a control algorithm be developed that enables a CubeSat to obtain the pointing precision required for a camera payload?*

- *How can this be done through full 3-axes attitude control with basis in the available testbed using reaction wheels for actuation?*

To achieve this goal, requirements were derived with basis in three actions: Nadir pointing, point tracking, and a step change between the two.

Before designing a controller, a dynamic model for the satellite was derived along with a model for the DC motors driving the reaction wheels. This nonlinear model was linearized in order to transform the model to the Laplace domain, where a transfer function matrix was obtained. An analysis of the system showed that this MIMO system could be reduced to three SISO systems. A PI controller was then designed for each of the three axes. Based on the requirements to steady state errors, a PI controller was chosen.

The controller was implemented in a simulation environment along with the nonlinear satellite model and environmental disturbance torques. The simulations showed that the nonlinear model and the linearized model gave similar responses, and that the simulations fulfilled the requirements.

Next the controller was tested on a testbed developed by former AAU students with the intention of being able to test attitude control algorithms in three dimensions. This testbed proved to only be able to be used for attitude control in one axis due to an uneven mass distribution of the satellite model. In addition to this, the air bearing of the testbed

caused a large disturbance torque to the satellite model making the reaction wheels reach saturation too fast and thus making the test results hard to compare to simulations.

Instead the testbed satellite model was suspended using a fishing line. Here the disturbance proved to be less dominant than the air bearing. Tests here showed that the satellite was able to follow a reference equivalent to a velocity-wise faster nadir pointing and still fulfill the precision requirement. The system was able to follow the point tracking trajectory as well in a similar fashion to the simulations, but not withing the required pointing precision. The system was also able to follow a step response, but at a slower rate than what the simulations showed, and unable to fulfill the requirements regarding settling time and overshoot, although it was only by small margins. These differences between simulations and tests were deemed to be due to the large disturbance during the tests and due to the different moment of inertia between the simulated satellite and the testbed satellite model.

All in all, the tests and simulations showed that the designed attitude control system was able to successfully prove the concept of controlling the attitude of a CubeSat, but not quite able to meet the strict requirements.

## 8.2 Future Improvements

Through the project and based on the results, wishes for future improvements has been noted, and will in this section be gone through.

### 8.2.1 Momentum dumping and magnetorquers

A solution to the reaction wheels reacting saturation on the testbed, is to implement magnetorquers on the system, which would allow the system to perform momentum dumping via the magnetic field introduced by the Helmholtz coil. The finished AAUSAT6 satellite will undoubtedly be equipped with magnetorquers, and this addition to the testbed satellite would prove useful, as it allows for testing momentum dumping and control of magnetorquers in collaboration with reaction wheels, which would produce valuable knowledge.

### 8.2.2 Specified controller for the testbed

It was evident that the adjustment envisioned for the controller, as an attempt to tackle the change of inertia, when going from the simulated satellite to the testbed system were ineffective, as the result of tests on the testbed showed no clear improvement to the new controller's regulation of the satellite. It is believed that if a controller, with the disturbance produced by the testbed taken into account, was produced, the results gained would be improved. The reaction wheels would still reach saturation, if no other actuators are introduced, so maybe it would be best to implement this in conjunction with the aforementioned magnetorquers.

### 8.2.3 Multiple controllers

As the control is based on linear models with basis in a specific operation point, multiple controllers could be implemented to handle the changing points of operation during the

point tracking maneuver. This would lead to a general smaller error between the linearized model and the nonlinear model, especially with relation to the operation point of the satellite angular velocity.

#### 8.2.4 Investigation of simulated disturbances

The unexpected results of the simulated long term disturbance effects on the reaction wheels velocity, shown in figure 6.6, is counterintuitive and the physical test resulted in saturation fairly fast. It would therefore be interesting to further investigate the cause whether it is due to the simulations not being correct, the periodicity in an orbit or other reasons.



# Bibliography

- [1] celestrak.com [website]. CSSI (Center for Space Standards and Innovations); [cited 25-05-2018]. Available from: <https://celestrak.com>.
- [2] Wertz JR. Spacecraft Attitude Determination and Control. D. Reidel Publishing Company; 1978.
- [3] Starin SR, Eterno J. Attitude Determination and Control Systems [NASA Technical Report Server]. NASA Goddard Space Flight Center; 2011. Available from: <https://ntrs.nasa.gov/search.jsp?R=20110007876>.
- [4] Ebert H, Raskmark P. Grundlæggende Maxwellsk Feltteori. Aalborg Universitet; 1998.
- [5] Ebert H. Transducere - Note til kurset "Elektromagnetisme". AUC; 1989.
- [6] Holst R. Satellite Attitude Control Using Magnetorquers with Magnetic Dipole Moment Cancellation [Master's Thesis]. Aalborg University; 2014.
- [7] Thomsen BG, Nielsen J. CubeSat Sliding Mode Attitude Control - Developing Testbed for Verification of Attitude Control Algorithms [Master's Thesis]. Aalborg University; 2016.
- [8] Bolet OKS, Clausen HG, Jensen JK, Köhne JB, Seindal MS. AAUSAT-kamera [P4 Semester Project]. Aalborg University; 2017.
- [9] OreSat - Cubesat Camera Field of View [Article on the internet]. Oregon Small Satellite Project; [cited 03-04-2018]. Available from: <http://oresat.org/field-of-view/>.
- [10] Kuipers JB. Quaternions and Rotation Sequences: A Primer with Applications to Orbits, Aerospace, and Virtual Reality. Princeton University Press; 1999.
- [11] Jensen KF, Vinther K. Attitude Determination and Control System for AAUSAT3 [Master's Thesis]. Aalborg University; 2010.
- [12] EC 9.2 flat Ø10 mm, brushless, 0.5 Watt: Part number 371119 [Datasheet]. Maxon Motors; 2015.
- [13] Kök I. Comparison and Analysis of Attitude Control Systems of a Satellite Using Reaction Wheel Actuators [Master's Thesis]. Luleå University of Technology; 2012.
- [14] Skogestad S, Postlethwaite I. Multivariable Feedback Control: Analysis and Design. 2nd ed. Wiley-Interscience; 2005.

- [15] Franklin GF, Powell JD, Emami-Naeini A. Feedback Control of Dynamic Systems.  
4th ed. Prentice Hall; 2002.
- [16] Sidi MJ. Spacecraft Dynamics and Control: A Practical Engineering Approach.  
Cambridge University Press; 1997.

# A | Quaternions

Quaternions are hypercomplex numbers composed of a real part (called the scalar part) and three imaginary parts with imaginary units  $i$ ,  $j$  and  $k$ , which can be written as:

$$\mathbf{q} = q_4 + q_1i + q_2j + q_3k \quad (\text{A.1})$$

Quaternions can be represented as a four-vector:

$$\mathbf{q} = \begin{bmatrix} q_1 \\ q_2 \\ q_3 \\ q_4 \end{bmatrix} = \begin{bmatrix} \mathbf{q} \\ q_4 \end{bmatrix} \quad (\text{A.2})$$

The value  $q_4$  is called the scalar part and  $\mathbf{q}$  is called the vector part. A quaternion with a scalar part equal to zero is called a pure quaternion.

The fundamental identity of quaternions is given by:

$$i^2 = j^2 = k^2 = ijk = -1 \quad (\text{A.3a})$$

$$ij = -ji = k \quad (\text{A.3b})$$

$$jk = -kj = i \quad (\text{A.3c})$$

$$ki = -ik = j \quad (\text{A.3d})$$

This means that quaternion multiplication is non-commutative. Quaternion multiplication is performed in the same way as multiplication by complex numbers, except that the order of operations is important due to the non-commutativity.

The quaternion norm is given by:

$$|\mathbf{q}| = \sqrt{\mathbf{q}^* \mathbf{q}} = \sqrt{q_1^2 + q_2^2 + q_3^2 + q_4^2} \quad (\text{A.4})$$

The complex conjugate of a quaternion is given by:

$$\mathbf{q}^* = q_4 - q_1i - q_2j - q_3k \quad (\text{A.5})$$

The inverse of a quaternion is given by:

$$\mathbf{q}^{-1} = \frac{\mathbf{q}^*}{|\mathbf{q}|^2} \quad (\text{A.6})$$

This means that for a unit quaternion, the complex conjugate and the inverse is the same.

A quaternion with norm 1 is called a unit quaternion and represents a rotation. A rotation about an axis  $\hat{\mathbf{e}}$  by an angle  $\Phi$  can be described by the Euler Symmetric Parameters:

$$q_1 = e_1 \sin\left(\frac{\Phi}{2}\right), \quad (\text{A.7a})$$

$$q_2 = e_2 \sin\left(\frac{\Phi}{2}\right), \quad (\text{A.7b})$$

$$q_3 = e_3 \sin\left(\frac{\Phi}{2}\right), \quad (\text{A.7c})$$

$$q_4 = \cos\left(\frac{\Phi}{2}\right) \quad (\text{A.7d})$$

The direction cosine matrix rotation matrix described using quaternions can be expressed as [2]:

$$\mathbf{A}(\mathbf{q}) = \begin{bmatrix} q_1^2 - q_2^2 - q_3^2 + q_4^2 & 2(q_1 q_2 + q_3 q_4) & 2(q_1 q_3 - q_2 q_4) \\ 2(q_1 q_2 - q_3 q_4) & -q_1^2 + q_2^2 - q_3^2 + q_4^2 & 2(q_2 q_3 + q_1 q_4) \\ 2(q_1 q_3 + q_2 q_4) & 2(q_2 q_3 - q_1 q_4) & -q_1^2 - q_2^2 + q_3^2 + q_4^2 \end{bmatrix} \quad (\text{A.8a})$$

$$= (q_4^2 - \mathbf{q}^2) \mathbf{I} + 2\mathbf{q}\mathbf{q}^T - 2q_4 \mathbf{Q} \quad (\text{A.8b})$$

where  $\mathbf{Q}$  is the skew-symmetric matrix:

$$\mathbf{Q} = \begin{bmatrix} 0 & -q_3 & q_2 \\ q_3 & 0 & -q_1 \\ -q_2 & q_1 & 0 \end{bmatrix} \quad (\text{A.9})$$

The Euler symmetric parameters of a given direction cosine matrix can be found from [2]:

$$q_4 = \pm \frac{1}{2}(1 + A_{11} + A_{22} + A_{33}) \quad (\text{A.10a})$$

$$q_1 = \frac{1}{4q_4}(A_{23} - A_{32}) \quad (\text{A.10b})$$

$$q_2 = \frac{1}{4q_4}(A_{31} - A_{13}) \quad (\text{A.10c})$$

$$q_3 = \frac{1}{4q_4}(A_{12} - A_{21}) \quad (\text{A.10d})$$

How quaternions are used and implemented can be read in section 4.1 covering how rotations are done.

# B | Controller test using the ACS testbed and suspension

## B.1 Controller test using the testbed

### Purpose

The purpose of this test is to verify that the controller designed in chapter 5 works as intended in practice. This is done by testing it on the ACS testbed designed by Thomsen and Nielsen [7].

### List of equipment

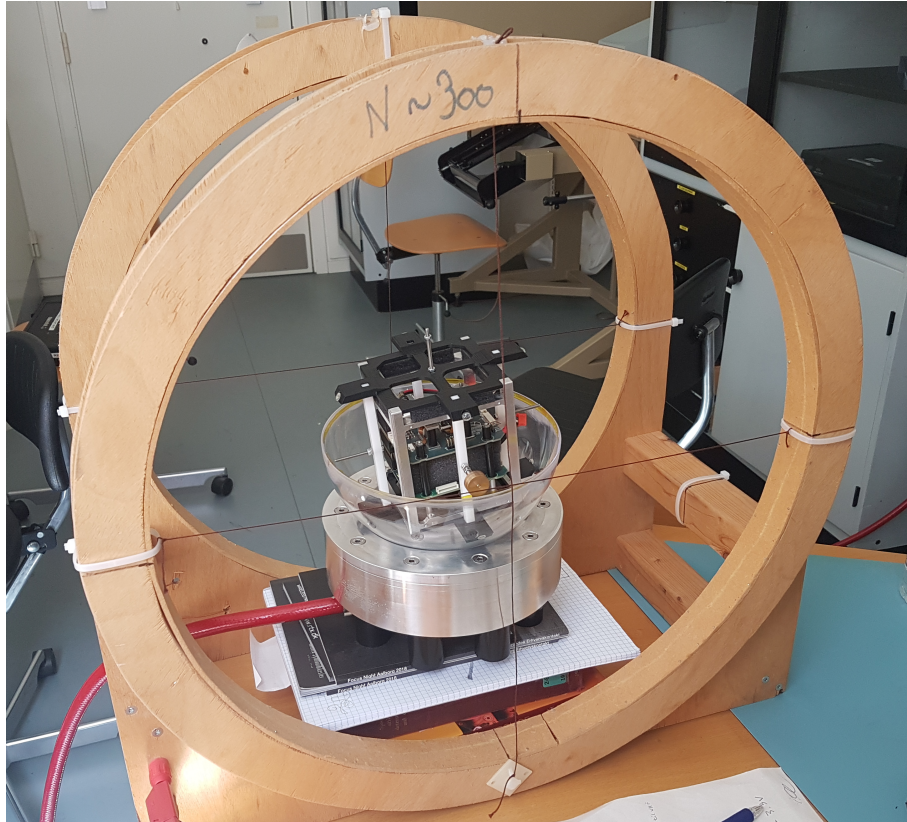
Instrument	AAU No.	Type
ACS testbed	-	-
XBee Pro S2B	-	-
Linux computer with relevant software	-	-
Power supply (0 - 32 V) (0 - 2 A)	61596	Triple Power Supply HM7042-5
Helmholtz coil	-	Ø0.4m, 300 windings

Table B.1: List of equipment for the test.

### Test setup

The Linux computer is set up with relevant software beforehand, and the XBee module is connected to the computer.

The ACS testbed is placed in the middle of the Helmholtz coil as shown in figure B.1. Only the lower half of the acrylic ball is used to keep the satellite stabilized in the  $z$ -axis.



**Figure B.1:** Picture of the test setup.

During the first 20 seconds of every test, after pressing run in Simulink the controller is disabled and the reaction wheels are running at their bias point. During these 20 seconds it is possible to stabilize the satellite by hand to make the initial satellite angular velocity zero and the initial error zero. This is to ensure that every test has the same starting conditions, that is  $\omega_{s0} = \mathbf{0}$ ,  $\omega_{rw0} = \omega_{bias}$  and  $\mathbf{q}_{err0} = [0\ 0\ 0\ 1]^T$ .

### Controller adjustment

As described in section 7.1.2, the moment of inertia is different for the testbed compared to AAUSAT3. Adjusting the controller to the testbed moment of inertia leads to reducing the  $K_p$  gain from 13 to 5, yielding:

$$D_{y-tb}(s) = 5 \cdot \frac{s + 0.13}{s} \quad D_{y-tb}(z) = \frac{5z - 4.935}{z - 1} \quad (\text{B.1})$$

Values of essential parameters for the step response of the new controller is summarized in table B.2

Parameter	Old controller	New controller	Unit
<i>W.r.t reference</i>			
Rise time	0.89	1.87	seconds
Settling time	8.08	17.99	seconds
Overshoot	16.12	15.80	%

**Table B.2:** Values of the new y-axis controller

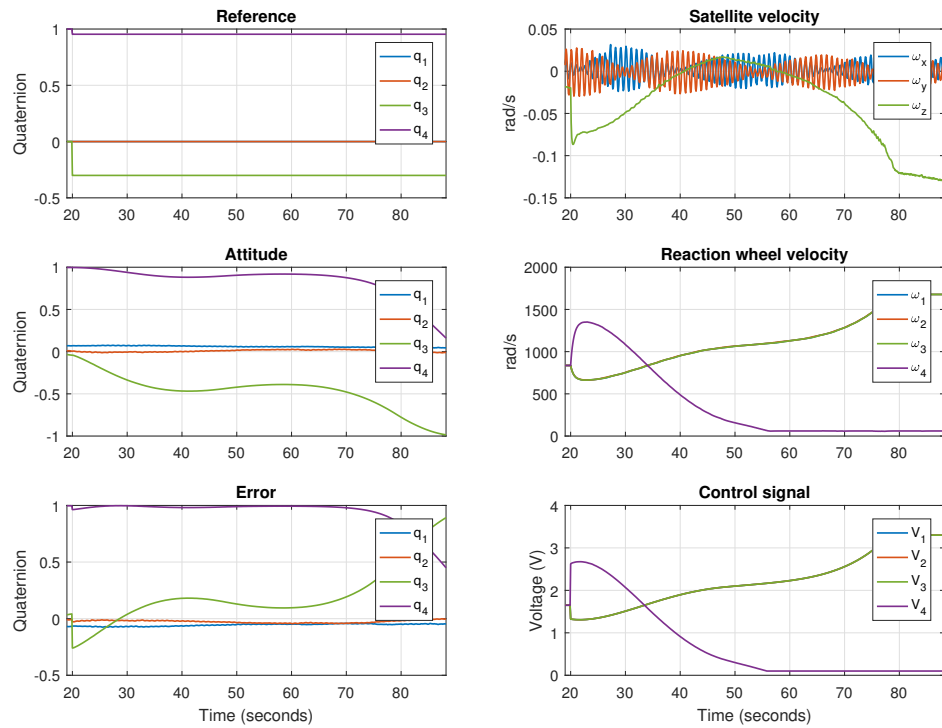
Only the change of inertia is addressed, other subjects such as change of center of mass is presumed to have minimal effects on the model and design of controller.

Both the new and the old controller has been tested on the testbed, to see if the adjustment had any effect, and if so how much of an effect.

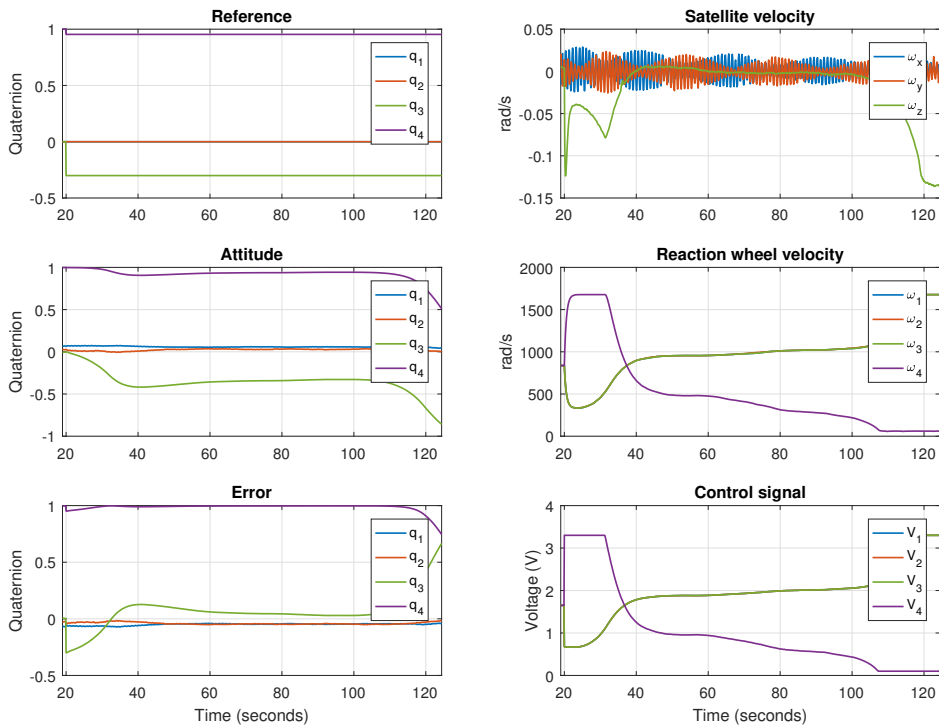
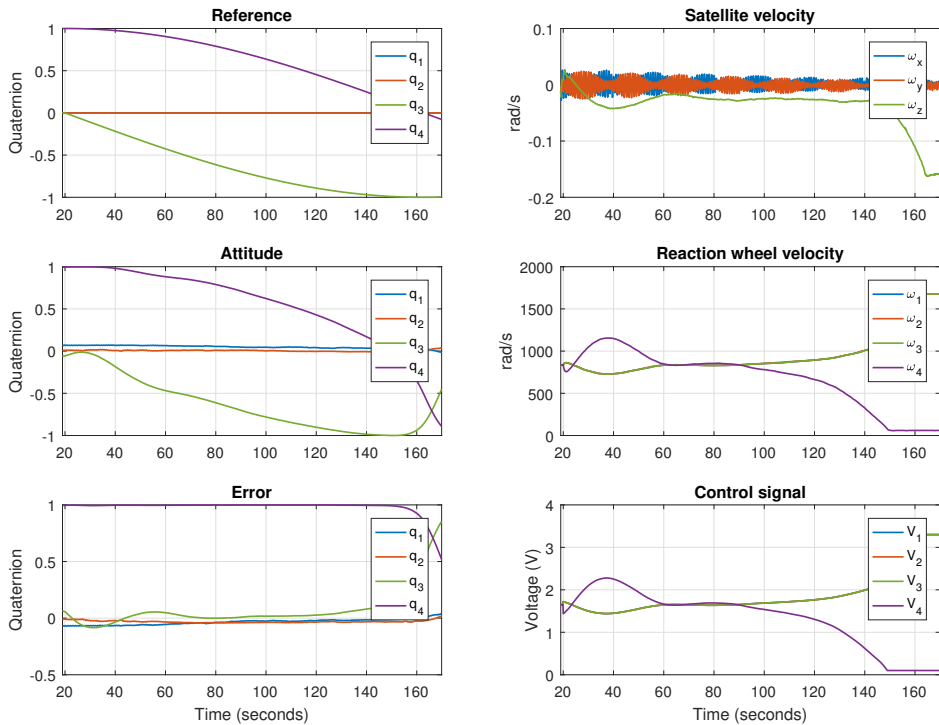
## Method

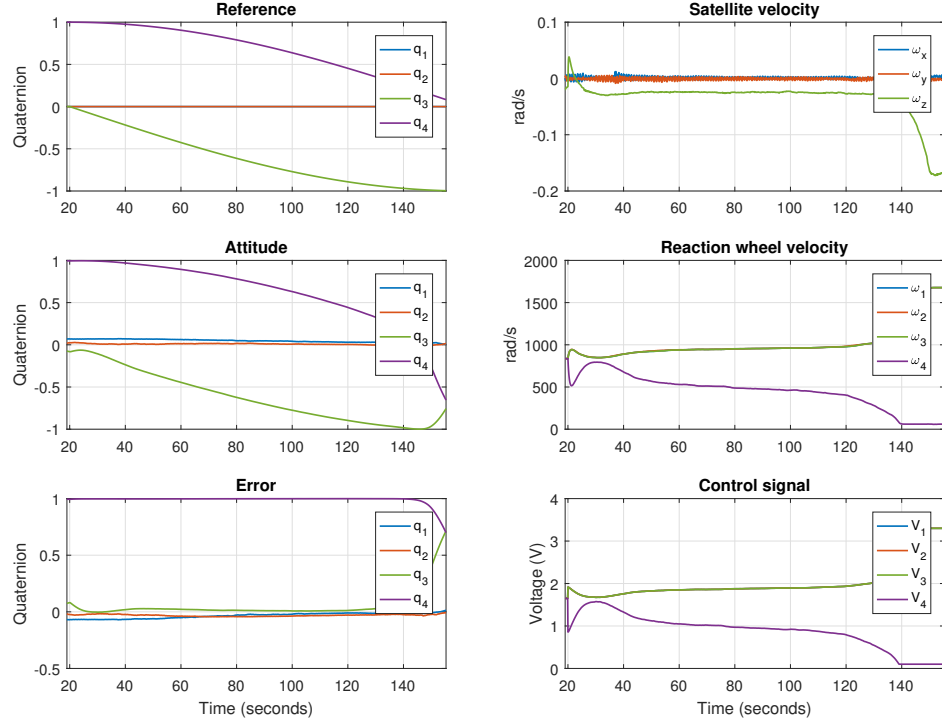
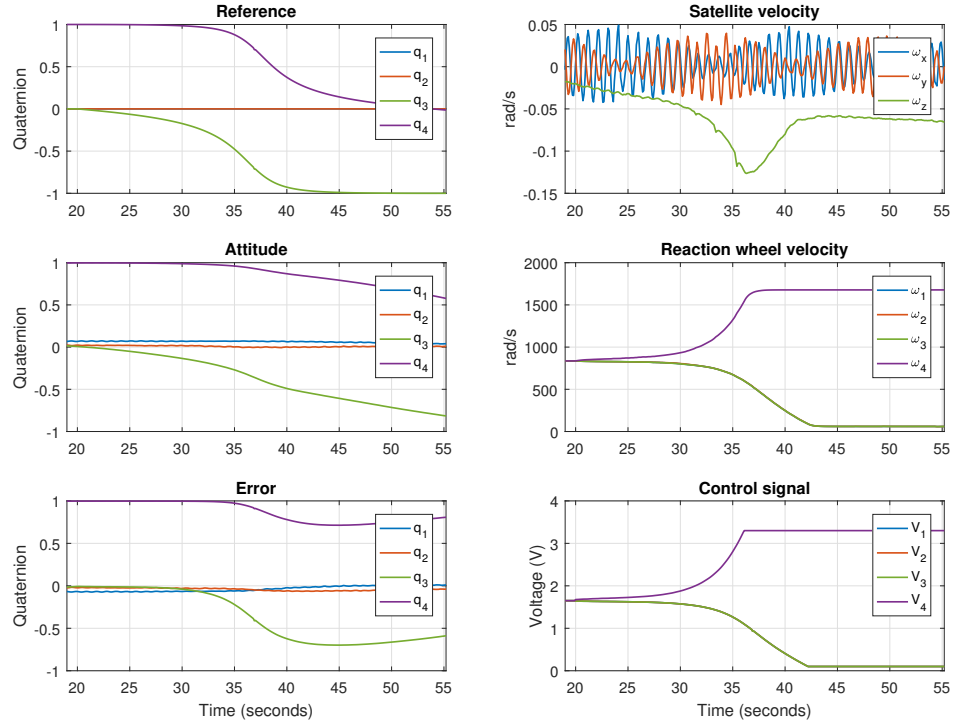
1. Turn on the power supply to the Helmholtz coil on 8.73 V and 1.95 A
2. Turn on the pressured air on 0.5 bar
3. Adjust the adjustable mass on the satellite to make the satellite as mass symmetric as possible in the  $x$ - and  $y$ -axis
4. Press "Run" in Simulink
5. During the next 20 seconds, adjust the satellite so the initial satellite speed and error are zero
6. Let go of the satellite
7. Log the data until all wheels reach saturation
8. Repeat item 4 to 8 with all relevant controllers and references

## Results



**Figure B.2:** Step input,  $K_p = 5$ , control in  $z$ -axis.

**Figure B.3:** Step input,  $K_p = 13$ , control in  $z$ -axis.**Figure B.4:** Ramp input,  $K_p = 5$ , control in  $z$ -axis.

**Figure B.5:** Ramp input,  $K_p = 13$ , control in  $z$ -axis.**Figure B.6:** Target trajectory input,  $K_p = 5$ , control in  $z$ -axis.

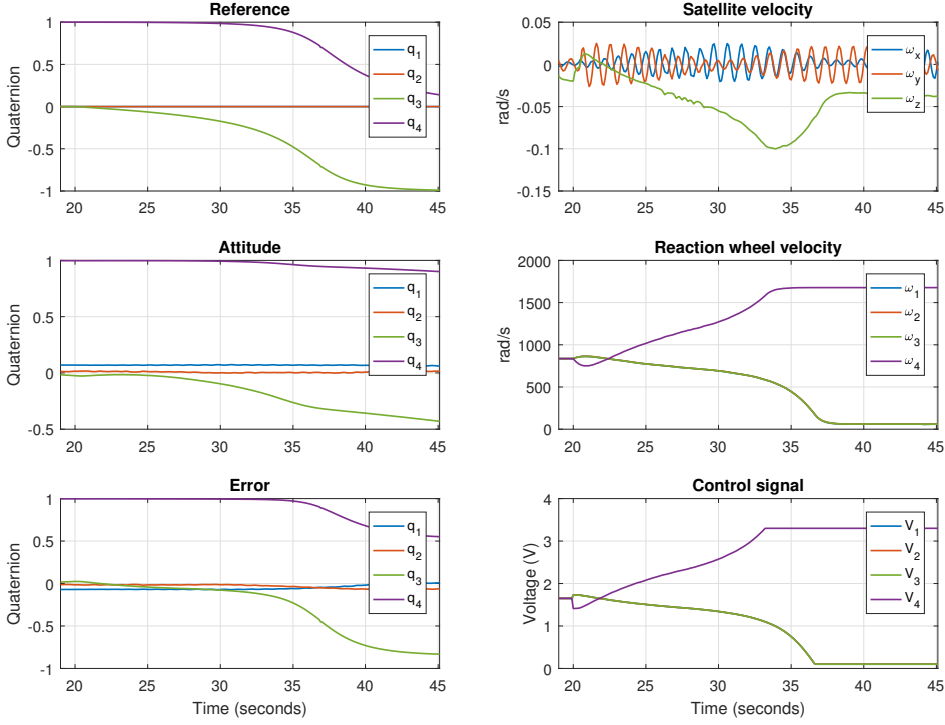


**Figure B.7:** Target trajectory,  $K_p = 13$ , control in  $z$ -axis.

## Sources of errors

- The disturbance torque from the testbed itself is too large compared to the possible actuation torque,
- The initial satellite attitude and initial satellite velocity is set by hand, which makes small errors likely
- The satellite's mass distribution is adjusted by hand and is difficult to make perfect. This results in the satellite always being tilted a bit about either the  $x$ - or the  $y$ -axis.
- The battery voltage may have varied during the tests, which may have influenced the actual input voltage to the motors.
- Packet losses between the ACS testbed and the Simulink computer can occur, which will influence the control.

## B.2 Controller test using suspension

### Purpose

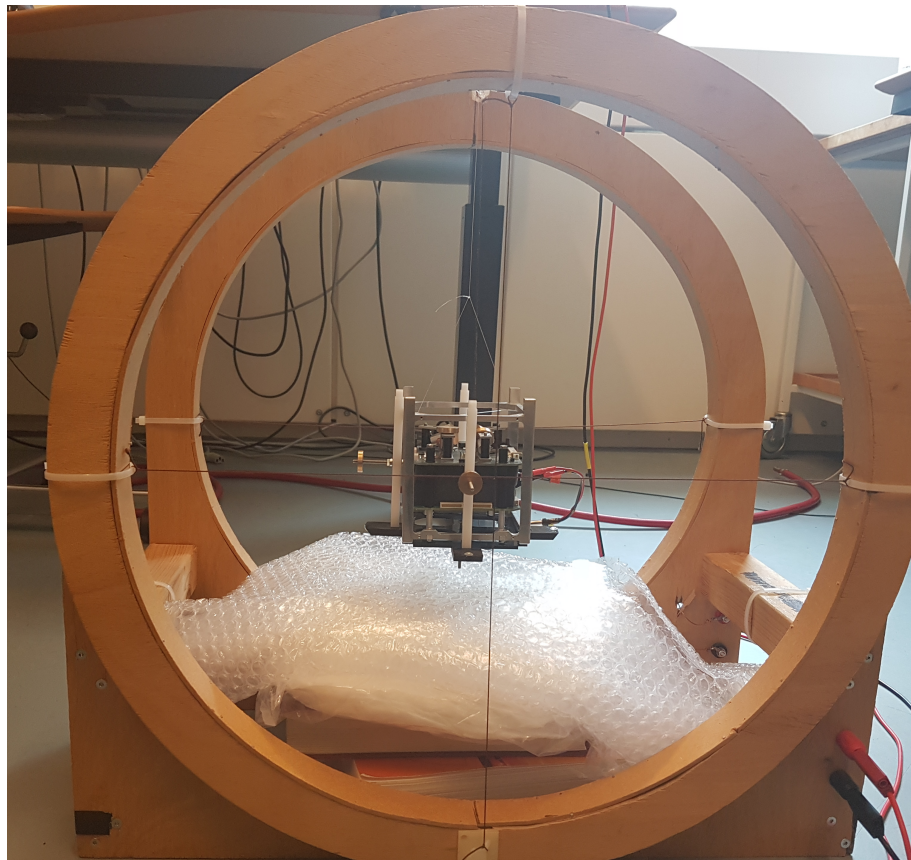
The purpose remains the same as in the test before.

### Test setup

The suspended satellite model is fastened to the fishing line. The other end of the fishing line is fastened to a beam 3.5 m above. The satellite model is placed in the middle of the

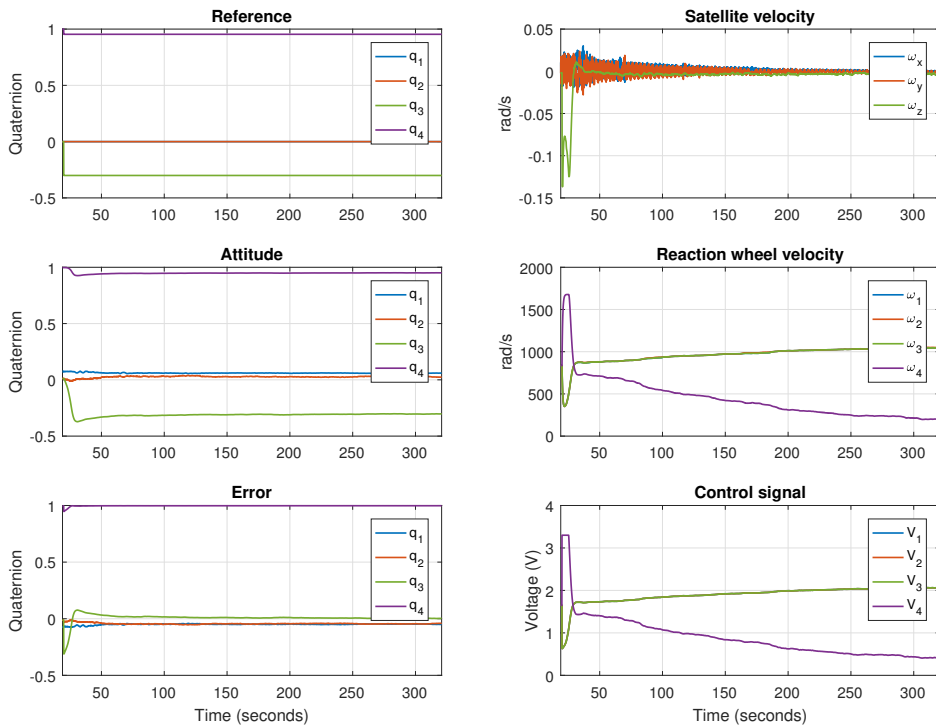
Helmholtz coil as shown in figure B.8. Beneath the satellite model is placed soft material to catch it if the line holding the satellite should break.

The equipment, test setup, method and sources of errors is almost the same. The testbed and effect related to the testbed is of course different. Which most significantly means that the system is affected by the disturbance torque from the line suspending the system. It applies a disturbance torque originating from the torsion happening when the line is twisting.

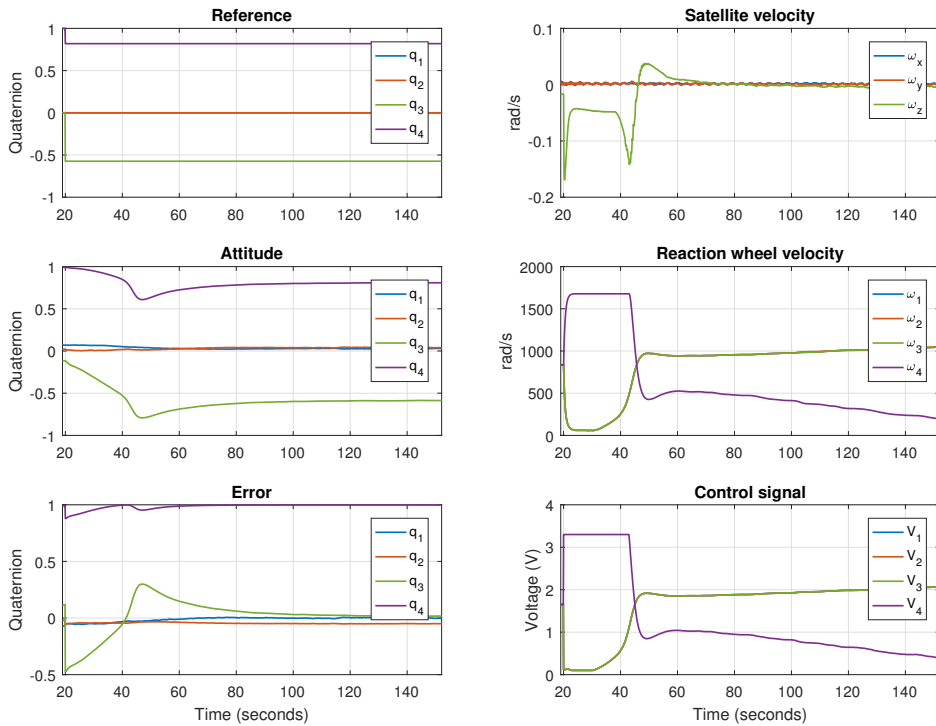


**Figure B.8:** Picture of the test setup.

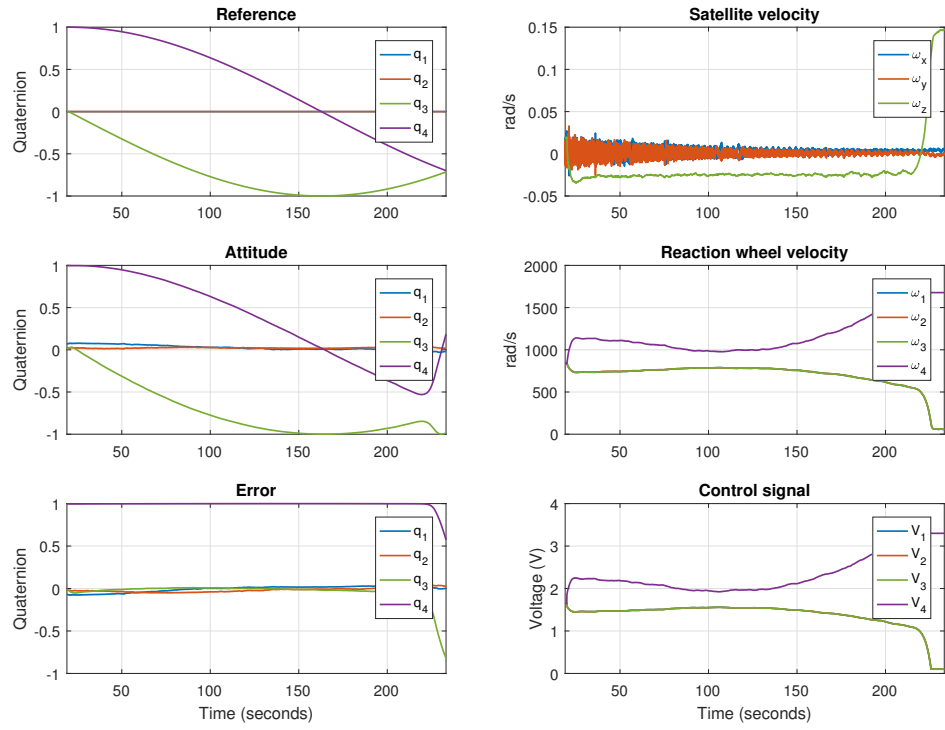
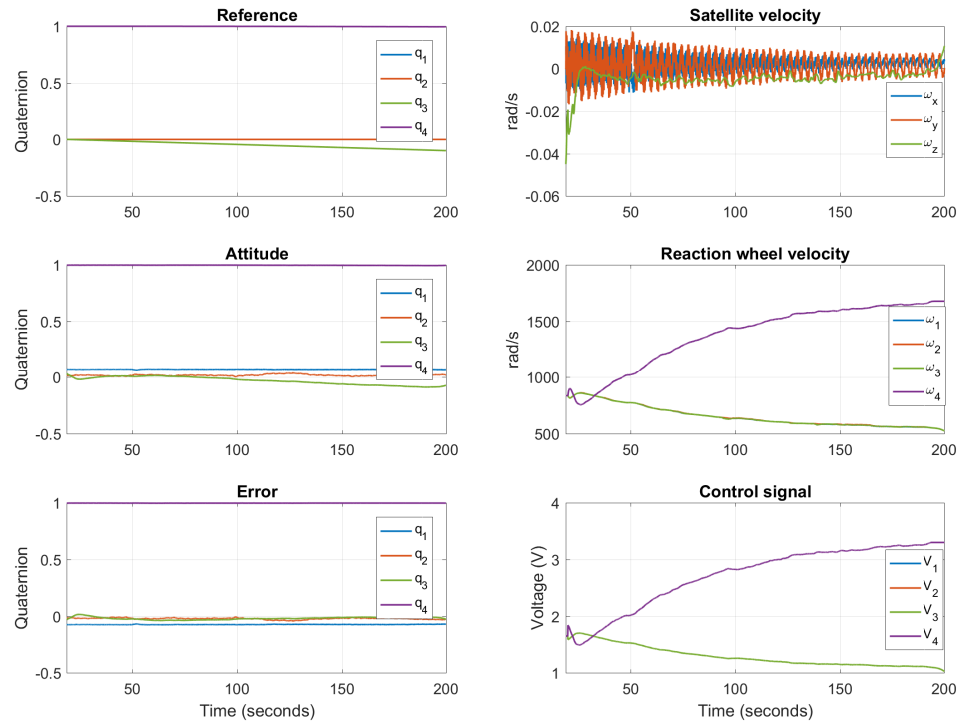
## Results



**Figure B.9:** 35 degree step,  $K_p = 13$ .



**Figure B.10:** 70 degree step,  $K_p = 13$ .

**Figure B.11:** Ramp with slope 0.022 rad/s,  $K_p = 13$ .**Figure B.12:** True nadir (-0.0011 rad/s),  $K_p = 13$ .

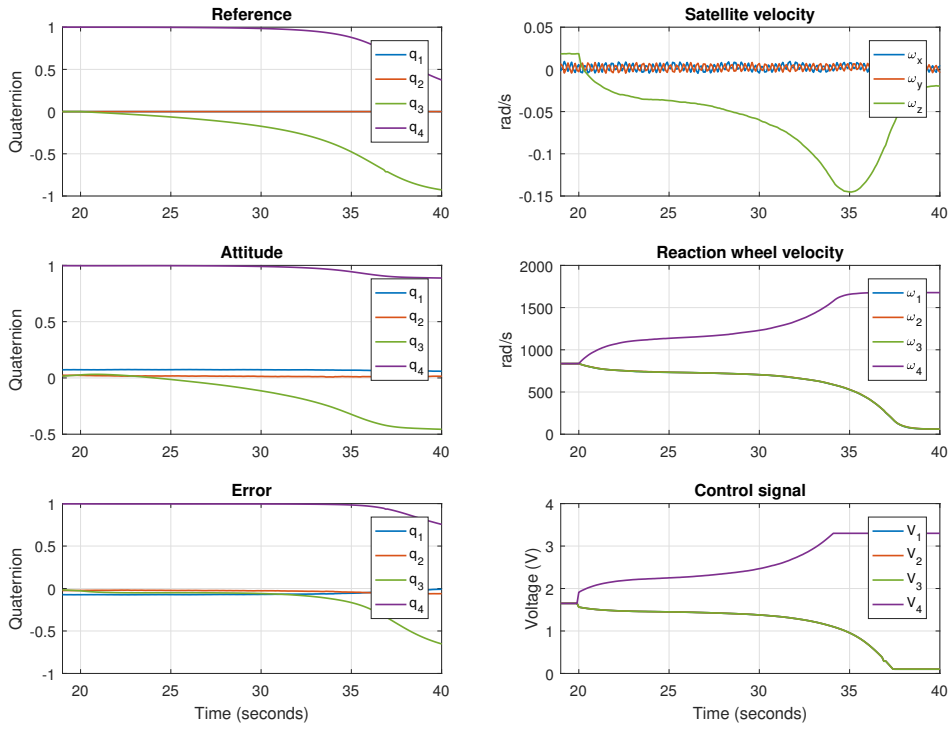


**Figure B.13:** Scaled target trajectory (x20),  $K_p = 13$ .